

LEVEL ~~II~~

✓ ARO 15124.9-MS

6

AD A103558

MOLECULAR DESIGN AND SYNTHESIS
OF
NEW NONCRYSTALLINE SOLIDS

FINAL REPORT

by

Rustum Roy
Russell Messier

JUNE 1981

U.S. Army Research Office

Contract Nos. DAAG29-78-G-0033
and
DAAG29-80-C-0089

DTIC FILE COPY

DTIC
ELECTE
SEP 1 1981
D

DISTRIBUTION STATEMENT A

Approved for public release;
Distribution Unlimited



THE MATERIALS RESEARCH LABORATORY

THE PENNSYLVANIA STATE UNIVERSITY

UNIVERSITY PARK, PENNSYLVANIA

81 9 01 145

Accession For	
NTIS GRA&I	<input checked="" type="checkbox"/>
DTIC TAB	<input type="checkbox"/>
Unannounced	<input type="checkbox"/>
Justification	
By	
Distribution/	
Availability Codes	
Dist	Avail and/or Special
A	

MOLECULAR DESIGN AND SYNTHESIS
OF
NEW NONCRYSTALLINE SOLIDS

FINAL REPORT

by

Rustum Roy
Russell Messier

JUNE 1981

U.S. Army Research Office

Contract Nos. DAAG29-78-G-0033
and
DAAG29-80-C-0089

The Pennsylvania State University
Materials Research Laboratory
University Park, PA 16802

Approved for public release; distribution unlimited.

DTIC
ELECTE
S SEP 1 1981 D

The findings in this report are not to be construed as an official Department of the Army position, unless so designated by other authorized documents.

REPORT DOCUMENTATION PAGE		READ INSTRUCTIONS BEFORE COMPLETING FORM
1. REPORT NUMBER (6)	2. GOVT ACCESSION NO. AD-A303558	3. RECIPIENT'S CATALOG NUMBER (9) 28
4. TITLE (and Subtitle) MOLECULAR DESIGN AND SYNTHESIS OF NEW NON-CRYSTALLINE SOLIDS.		5. TYPE OF REPORT & PERIOD COVERED Final Report, 1 March 1978 - February 28, 1981
7. AUTHOR(s) (10) Rustum/Roy, Russell/Messier		6. PERFORMING ORG. REPORT NUMBER
9. PERFORMING ORGANIZATION NAME AND ADDRESS Materials Research Laboratory The Pennsylvania State University University Park, PA 16802		8. CONTRACT OR GRANT NUMBER(s) (15) DAAG29-78-G-0033 DAAG29-80-C-0089
11. CONTROLLING OFFICE NAME AND ADDRESS U.S. Army Research Office Post Office Box 12211 Research Triangle Park, NC 27709		10. PROGRAM ELEMENT, PROJECT, TASK AREA & WORK UNIT NUMBERS P-51124-MS
14. MONITORING AGENCY NAME & ADDRESS (if different from Controlling Office) (12) 154		12. REPORT DATE (11) Jun 81
		13. NUMBER OF PAGES 150
		15. SECURITY CLASS. (of this report) Unclassified
		15a. DECLASSIFICATION/DOWNGRADING SCHEDULE N/A
16. DISTRIBUTION STATEMENT (of this Report) Approved for public release; distribution unlimited. (18) ARO / (14) 15124.9-MS		
17. DISTRIBUTION STATEMENT (of the abstract entered in Block 20; if different from Report) N/A		
18. SUPPLEMENTARY NOTES The findings in this report are not to be construed as an official Department of the Army position, unless so designated by other authorized documents.		
19. KEY WORDS (Continue on reverse side if necessary and identify by block number) Noncrystalline Solids Amorphous Films Noncrystalline Solid Formation Thin Films Vapor Deposition Rapid Solidification rf-Sputtering		
20. ABSTRACT (Continue on reverse side if necessary and identify by block number) The general objective is to prepare and characterize novel noncrystalline thin film materials over a broad range of material's classes in order to gain a better understanding of noncrystalline solid formation behavior and to provide a scientific basis for future studies. We have prepared noncrystalline thin films covering a wide range of materials: insulators (nickel, iron and tungsten oxides; various polymers), metals (Mg-Zn alloys), and semiconductors (a number of metal-borides; cermet films like alumina-metal and polymer metal;		

CdTe; Si; Ge). In addition to this exploratory preparation work, we have investigated in detail the structure and bonding in a number of these materials. For understanding the short range order bonding characteristics we have used both Mössbauer and magnetic studies and Raman spectroscopy. Also using conventional TEM, high resolution STEM, and atom probe field ion microscopy we have studied the structure of noncrystalline films at the atomic level. Such nanostructural studies along with microstructural studies, primarily using scanning electron microscopy, are now allowing us to develop a general structural model for vapor-deposited noncrystalline thin film materials, which is distinctly different from the structure of conventional glasses (liquid-to-solid transformation). Due to the high energy quenching rate of vapor-to-solid transformation processes, such as rf-sputtering used extensively in this study, noncrystalline thin films can be prepared over a much wider composition range than conventional glasses. This leads to low surface and bulk mobility of the depositing atoms which, in turn, leads to a highly anisotropic, columnar structure with the columns aligned in the direction of the depositing vapor species. This low mobility in vapor-to-solid processes also leads to the formation of very fine (1-5nm) crystallites in films which appear noncrystalline by x-ray diffraction but are, in fact, microcrystalline, albeit highly metastable, thin films. This fine dispersion of microcrystalline metals in a noncrystalline matrix phase have been prepared and investigated in three different materials: alumina-Au, polymer (PTFE and Ekonol)-metal (Pt, Au, Cu), and Mg-Zn alloys.

TABLE OF CONTENTS

Foreword

Introduction

Summary of Research

References

Appendix A: Mössbauer and Magnetic Study of rf-Sputtered Fe_2O_3 Films

Appendix B: Low Frequency Modes in Amorphous Boron-Rich Alloys

Appendix C: Cluster Formation in Amorphous and Polycrystalline Thin Films

Appendix D: Fine Structure of Gold Particles in Thin Films Prepared by Metal-Insulator Co-Sputtering

Appendix E: Microdiffraction from Gold Microcrystals

Appendix F: Rapid Solidification by rf-Sputtering in the Mg-Zn-O System

Appendix G: Polymer and Polymer-Metal Films by rf-Sputtering

Appendix H: Preparation and Properties of Amorphous WO_3 Films

Appendix I: Voids in Thin Films: A TEM and FIM Comparison

FOREWORD

The research reported here and in six preceding semi-annual reports is the result of a three-year effort at a modest level of funding (\$138,217 total for 3 years) on the "Molecular Design and Synthesis of New Noncrystalline Solids". The principal investigators were Rustum Roy, Evan Pugh Professor of the Solid State and Russell Messier, Senior Research Associate. They were assisted by three graduate students, Pamela Kistler, Ronnen Roy, and Ajay Bholagir. The latter student (Ajay Bholagir) received only research support with his financial support coming from a Government of India Fellowship. Other scientific personnel who contributed to this research effort included Visiting Professor G. P. Srivastava (on sabbatical for 6 months), Dr. L. A. Marusak, Dr. S. V. Krishnaswamy, Professor T. T. Tsong, Mr. S. B. McLane, Professor J. M. Cowley (Arizona State University), and Professor D. J. Barber (University of Essex).

INTRODUCTION

While in actual fact a large proportion of the solid matter on the surface of the earth is noncrystalline (by the conventional definitions of not coherently diffracting x-rays to Bragg maxima), yet the typical materials' scientist is trained to think that "glasses", the prototype noncrystalline solid (NCS), represent an esoteric small class of specialized materials. This is of course untrue. A very high proportion of biologically generated solids are NCS. Much of the mineral weathering product on the surface of the earth is also NC, despite the misleading impression gained by running a powder pattern (of the mixture of noncrystalline and crystalline matter). Among man-made products, the tonnages of set concrete, low grade ceramic ware, most polymers and glass loom very large in the total of manufactured solids, and a good fraction of these solids is NC. Yet the scientific attention received so far, by the noncrystalline branch of the solid state, is very small.

There are two major reasons for this excessive concentration on the crystalline state. First, an era of modern solid state technology was based on the tractable theories of periodic arrangements of atoms. Diffraction theory, Kramers-Kronig, and semiconductor physics and dislocation mechanics, were all fine fruits of this model for (at least part of) nature. Second, it was true till 1960 that, of all the usual combinations of elements that one could assemble, only a very few could be made to yield noncrystalline phases with the experimental tools then available. Thus was born the false dichotomy between the supposedly important majority: interesting, simple (most metals and monatomic solids) and crystalline and the tiny minority of solids: "the glassformers" (silicates, phosphates, borates, germanates and a few oddities like chalcogenides of metalloids).

Since 1960 when this picture held, both the reasons enumerated have become invalid. Solid state physics has mined out the periodic lattice and armed with contemporary computer power is looking for new worlds to conquer. Moreover, as solid state chemists started to catch up to their physicist colleagues, the range of noncrystalline solids has begun to expand tremendously. First, of course, as polymers became a more visible reality in materials science, it was clear that a very high percentage of useful man-made solid matter was noncrystalline. Next the technological success of the pyroceram process showed the intimate connection between the two states. Then, in the early sixties in a masterstroke of serendipitous scientific sociology, Mr. Sanford Ovshinsky engaged as his consultants a remarkable array of theoretical solid physicists. Ovshinsky's company (Energy Conversion Devices) was trying to exploit the electronic switching effects in glassy and truly noncrystalline chalcogenide semiconductors. Largely because of the interest of theorists, who could hardly have been expected to make this marginal technology of NC-solid state electronics succeed, the science of NC solids gained an enormous boost. At the same time, in a little noticed series of papers, Prof. Pol Duwez⁽¹⁾ at Cal Tech had devised a technique for rapid quenching of metal samples some thousand times faster than anything theretofore attained. With it he was able to make true noncrystalline glasses out of some rather special alloy compositions. If even metals could thus be made noncrystalline, and theoreticians were interested, it is clear that the world of materials science was at the beginning of a major new opening towards the noncrystalline state.

Simultaneously with the emerging interest in glass formation in novel compositions, and the discovery of splat-cooling, the new technology of forming solids via the vapor phase by sputtering was being re-developed. Again, most of

the work was done on metals and semiconductors. However, due to the importance of SiO_2 (and Si_3N_4) in integrated circuitry considerable work was done in these systems. This work obviously highly restricted with respect to composition, is also typically not very detailed on chemical and structural characterization.

Noncrystalline solids are metastable phases. Sputtering gives us a simple method to increase the probability of metastable phase formation (eg., because of the high quenching rate) and retention (because of the low substrate temperature). Moreover, control of the sputtering process allows extremely fine tuning of the degree of structural order in the sputtered films. The rationale for a systematic study of metastable (especially noncrystalline thin films synthesis by rf-sputtering therefore becomes obvious.

Materials prepared by the vapor-to-solid route are generally metastable, non-equilibrium, solids. The main reasons for this metastability are: the high rate of quenching ($\sim 10^{10}$ °C/sec); the relatively low T/T_m 's (where T = temperature of film during preparation and T_m = melting point of the final film composition, °K) during thin film vapor deposition; and the high solid solubility of normally insoluble elements and compounds which results from both the atom-by-atom nature of the condensation process and the high quench rate of these metastable assemblages. The fundamental difference between vapor deposited solids and those prepared from either the liquid or solid phase rests in the ability to modify the growing film by altering its surface reactions and kinetics through vapor species, gaseous impurities, surface temperature, and bombardment (ions, neutrals, electrons) processes.

The exact nature of the metastability in thin films can be related to both their crystal structure and physical structure. The physical structural features common to both crystalline and noncrystalline thin films prepared at

$T/T_m \approx 0.7$ are anisotropic, columnar structures with low-density regions (commonly called voids) surrounding them. The crystal structure is primarily that of the columns and must consider intermediate-range ordering (clustering of atoms and smaller clusters) as well as short- and long-range ordering for a complete understanding of its contribution to metastability. The physical structure component of a (single-phase) thin film's metastability is primarily that of the intercolumnar, void network regions in which both the chemistry and structure are radically different from the columnar regions. For multi-phase films (eg., fine crystals in a noncrystalline matrix phase) the energy stored at the phase boundaries may also be an important contribution to the overall film metastability.

Until recently the void contribution to thin film material metastability has not been considered. For that matter even intermediate-range ordering effects (such as the energy stored in the structure and at the boundaries of a 20-100Å metastable crystallite) have hardly been studied. As we and others are now beginning to show, the amount of energy stored at these void surfaces can be the predominant contribution to film metastability and is reflected in unusual properties of thin films such as explosive crystallization⁽²⁻⁴⁾, anisotropic etching behavior⁽⁵⁻⁷⁾, interdiffusion⁽⁸⁾, fast ion conduction⁽⁹⁾, perpendicular magnetic anisotropy⁽¹⁰⁾, high-voltage photovoltaic effect⁽¹¹⁾, and variable optical properties⁽¹²⁾.

SUMMARY OF RESEARCH

The general objective of our research on "Molecular Design and Synthesis of New Noncrystalline Solids" is to prepare and characterize novel noncrystalline thin film materials over a broad range of materials' classes in order to gain a better understanding of noncrystalline solid (NCS) formation and to provide a scientific basis for follow-up work on such new materials that indicate a potential technological application. The primary preparation method that has been used is rf-sputtering since we have shown that it affords us the widest latitude in terms of compositions and kinetics for retention of noncrystalline solid films. Although considerable effort was put into preparing CdTe by fused-salt solutions, only crystalline films would be prepared. Our limited experience with this technique indicated that such a technique is both complex and limited in the extent to which film metastability could be varied. Thus, no positive results with respect to the contract objectives were achieved. This work is being written up as a Masters Thesis.

The research effort over the last three years has resulted in four papers published (Appendices A, B, C, D), two papers submitted for publication (Appendices E and F), and at least three more possible papers in which the research is nearly complete (Appendices G, H, I).

As seen in these appendices and as described in some detail in the semi-annual reports, we have prepared NCS films covering a wide range of materials: insulators (nickel, iron and tungsten oxides; various polymers), metals (Mg-Zn alloys), and semiconductors (a number of metal-borides; cermet films like alumina-metal and polymer metal; CdTe; Si; Ge). In addition to this exploratory preparation work, we have investigated in detail the structure and bonding in a number of these materials. For understanding the short range order bonding characteristics we have used both Mössbauer and magnetic studies

(Appendix A) and Raman spectroscopy (Appendix B). Also using conventional TEM (Appendices D and I), high resolution STEM (Appendices D and E), and atom probe field ion microscopy (Appendices C and I) we have studied the structure of noncrystalline films at the atomic level. Such nanostructural studies along with microstructural studies (Appendix H), primarily using scanning electron microscopy are now allowing us to develop a general structural model for vapor-deposited noncrystalline thin film materials, which is distinctly different from the structure of conventional glasses (liquid-to-solid transformation).

Due to the high energy quenching rate of vapor-to-solid transformation processes, such as rf-sputtering used extensively in this study, noncrystalline thin films can be prepared over a much wider composition range than conventional glasses. This leads to low surface and bulk mobility of the depositing atoms which, in turn, leads to a highly anisotropic, columnar structure with the columns aligned in the direction of the depositing vapor species. Such columns are ~ 10 - 20 nm in diameter and are as long as the film thickness. Depending upon preparation conditions these nano-columns cluster such that ~ 100 - 200 nm diameter micro-columns, consisting of a bundle of nano-columns, are created. Again, depending upon preparation condition, these microcolumns can cluster into macro-columns (~ 1000 - $10,000$ nm diameter). For all three types of columns, low-density regions (usually called by the misnomer "voids") surround the columns. It is in these low density (highly defective, high free energy state) regions where it is found that many of the anomalous properties of noncrystalline thin films originate and are controlled.

The model of the physical structure of a noncrystalline thin film is the composite result of all the various studies described above. In particular, our work on noncrystalline WO_3 thin films (Appendices H and I) is central to

this model. In this work we have studied the nano-structure by FIM and TEM (using phase-contrast focusing techniques), and micro- and macro-structure by SEM, and its structure related properties (superionic conductivity-electrochromic behavior) as a function of preparation conditions. This work is sufficiently far along that we can conclusively say that the ionic (hydrogen) conduction path is not a uniform structural effect but occurs along the low-density, anisotropic void networks which are present in these materials. This mechanism has not yet been suggested for this important class of materials, which find applications in batteries, electrochromic displays, etc. The significance of this mechanism should be great. It should be mentioned that Green⁽⁹⁾ has suggested an analogous mechanism which, however, is based on polycrystalline grain boundaries which are distinctly different from voids.

This low mobility in vapor-to-solid processes also leads to the formation of very fine (1-5nm) crystallites in films which appear noncrystalline by x-ray diffraction but are, in fact, microcrystalline, albeit highly metastable, thin films. This fine dispersion of microcrystalline metals in a noncrystalline matrix phase have been prepared and investigated in three different materials: alumina-Au and polymer-Au composite film experiments (Appendices D and E) and Mg-Zn work (Appendix F) have been completed while the remaining polymer and polymer-metal work (Appendix G) is in the final stages. Extensive characterization tests (compositions analysis, ac- and dc-conductivity versus temperature and frequency, TEM) on the polymer-metal films are nearly complete. The Mg-Zn results show that completely noncrystalline films can be prepared over a much wider composition range than rapidly quenched liquids. Furthermore, an even wider composition range of fine crystals dispersed in a NC matrix is obtained. However, work on the stability and structure of these types of materials is still incomplete though very much needed for defining the exact nature of the metastability in these disordered composite materials.

REFERENCES

1. P. Duwez, R. H. Willens, and W. Klement, J. Appl. Phys. 3, 1136 (1960).
2. T. Takamori, R. Messier, and R. Roy, Appl. Phys. Lett. 20, 201 (1972).
3. R. Messier, T. Takamori, and R. Roy, Solid State Commun. 16, 311 (1975).
4. S. V. Krishnaswamy, R. Messier, P. Swab, L. L. Tongson, and K. Vedam,
J. Elect. Mat. 10, 433 (1981).
5. R. Messier, S. V. Krishnaswamy, L. R. Gilbert, and P. Swab, J. Appl.
Phys. 51, 1611 (1980).
6. P. Swab, S. V. Krishnaswamy, and R. Messier, J. Vac. Sci. Technol.
17, 362 (1980).
7. L. R. Gilbert, R. Messier, and R. Roy, Thin Solid Films 54, 151 (1978).
8. S. V. Krishnaswamy, L. L. Tongson, N. Said, and R. Messier, J. Vac. Sci.
Technol. 18, 313 (1981).
9. M. Green, Thin Solid Films 50, 145 (1978).
10. A. G. Dirks and H. J. Leamy, Thin Solid Films 47, 219 (1977).
11. K. L. Chopra, Thin Film Phenomena, McGraw-Hill, New York (1969) p. 455.
12. G.A.N. Connell, in Amorphous Semiconductors, M. H. Brodsky, Ed., Springer-
Verlag, New York (1979) p. 73.

Mössbauer and magnetic study of rf-sputtered Fe_2O_3 films

L. A. Marusak^a and R. Messier

Materials Research Laboratory, The Pennsylvania State University, University Park, Pennsylvania 16802

We report Mössbauer and magnetic susceptibility data as a function of temperature for a thin film prepared by rf-sputtering from an Fe_2O_3 target in an O_2 -Ar atmosphere. Powder X-ray diffraction data shows very broad bands at $d = 2.7, 2.0$ and 1.5 \AA . The magnetic susceptibility data as a function of temperature may be divided into three regions. The low temperature region ($T < 170 \text{ K}$) shows a near constant susceptibility of $1.5 \times 10^{-4} \text{ emu/g}$. Between 170 and 225 K there is a dip in the susceptibility. For $T > 225 \text{ K}$ the susceptibility decreases with temperature in accord with the Curie Weiss law. We have estimated the Neel temperature to be 220 K from the peak in the magnetic susceptibility and the collapse of the magnetic hyperfine splitting in the Mössbauer data. While the film discussed in the present paper is amorphous, we have found that films sputtered at slightly higher power levels consist of microcrystals of $\gamma\text{Fe}_2\text{O}_3$.

PACS numbers: 75.50.Kj, 75.30.Kz, 76.80.+y

I. INTRODUCTION

There have been several magnetic studies [1-3] of iron oxide thin films prepared by chemical vapor deposition (CVD) or rf sputtering. These films have consisted of crystalline, microcrystalline and amorphous Fe_2O_3 . van Diepen and Popma [4] have prepared amorphous Fe_2O_3 by CVD techniques and found that the hyperfine field follows a temperature dependence similar to the Brillouin function for $S = 1/2$, although the hyperfine field (470KG) at $T = 5 \text{ K}$ is indicative of $S = 5/2$. In the above mentioned studies most films could be transformed to crystalline α or $\beta\text{-Fe}_2\text{O}_3$ through high temperature annealing.

In the present study we examine Mössbauer and magnetic susceptibility data as a function of temperature for a thin film prepared by rf-sputtering using conditions described previously by Messier and Roy [5]. The unique feature of our film is that it was prepared from an Fe_3O_4 target in an O_2 -Ar atmosphere. We have found that the collapse of magnetic hyperfine splitting in the Mössbauer spectra at $\sim 215 \text{ K}$ is a consequence of exchange fluctuations caused by structural disorder. The large reduction in the Neel temperature is consistent with the results reported in reference 4 for an amorphous Fe_2O_3 film.

II. EXPERIMENTAL

A thin film ($\sim 10 \mu\text{m}$ thickness) was prepared by rf-sputtering from a 99.9% purity Fe_2O_3 diameter target at a power level of 40 watts in $22\mu\text{Ar}$ and $8\mu\text{O}_2$ atmosphere at a deposition rate of $50 \text{ \AA}/\text{min}$. Mössbauer, magnetic measurements and X-ray diffraction were performed on a film which had been sputtered onto a 99.999% thin film aluminum foil. The substrate temperature during the sputtering process was 360 K [5]. Transmission electron microscopy (TEM) results on films sputtered at 50 watts and higher power levels show that these films consist of connected microcrystals of $\gamma\text{Fe}_2\text{O}_3$ on the order of 100 \AA . From these results we have concluded that the crystallinity of the films is a sensitive function of rf-power and substrate temperature (see figure 5 in ref. 5). Magnetic

susceptibility data was obtained using a Faraday balance and an electromagnet which produced a maximum field of 8 KOe. Mössbauer spectra were collected in the constant acceleration mode, using a $18\text{mCi } ^{57}\text{Co}$ in rhodium source and a 512 multichannel analyzer. Low temperature Mössbauer spectra were obtained using a Heli-Tran coldfinger manufactured by Air Products Co. The hyperfine parameters were obtained from spectra using hand calculations. In a later publication we will consider a distribution of hyperfine fields in fitting the Mössbauer spectra.

III. RESULTS AND DISCUSSION

Figure 1 shows an X-ray diffraction pattern of the film used in Mössbauer and magnetic susceptibility measurements. The diffraction bands at $d \sim 2.7$ and 2.0 \AA are consistent with oxygen-oxygen and iron-oxygen structural correlations, respectively. The diffraction band at $d \sim 1.5 \text{ \AA}$ may be caused by iron-iron structure correlations.

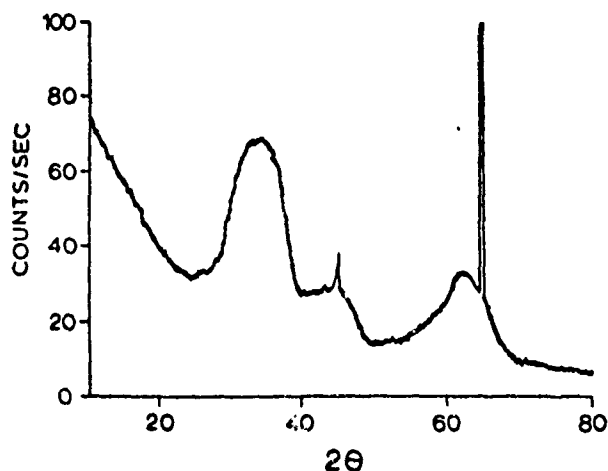


Figure 1. Powder X-ray diffraction pattern obtained using $\text{CuK}\alpha$ radiation. Sharp lines in the pattern are due to Al foil substrate.

One cannot rule out the possibility that the film discussed in the present study also consists of voids based on the TEM results of films sputtered at slightly higher power levels.

The temperature dependence of the magnetic susceptibility of the Fe_2O_3 film is shown in Figure 2. The low temperature magnetic susceptibility ($T < 170\text{K}$) shows a slight increase in susceptibility similar to the temperature dependence of an antiferromagnet.

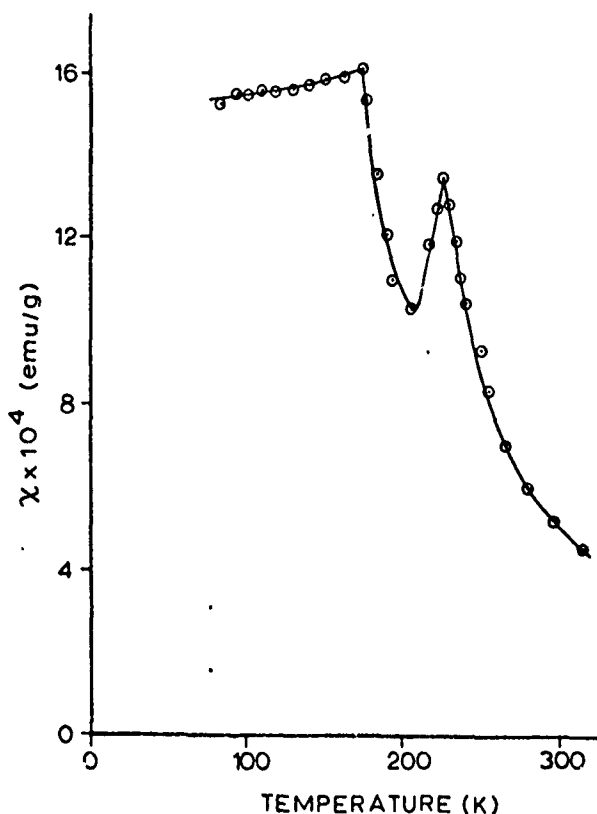


Figure 2. Magnetic susceptibility as a function of temperature for the Fe_2O_3 thin film.

Mössbauer data given in figure 3 show magnetic order below 215K. The broad line widths (~ 1.0 mm/sec) is indicative of structural disorder which causes a distribution in hyperfine fields. Figure 4 shows the temperature dependence of the hyperfine field as a function of reduced temperature along with a theoretical curve for $S = 5/2$. At lower temperatures the hyperfine field falls more rapidly than the $S = 5/2$ curve which is predicted by theoretical calculations which consider a distribution in exchange interactions. Conversely, the field is greater than what is expected for $S = 5/2$ at higher temperatures. Of considerable interest is the fact that the dip in the susceptibility coincides with the deviation in the hyperfine field from $S = 5/2$ for $170 \leq T \leq 215\text{K}$. At present the cause of these anomalies in the magnetic susceptibility and Mössbauer data are not clear.

Above 225K the susceptibility asymptotically approaches the Curie-Weiss law temperature dependence for $\mu_{\text{eff}} = 5.5\mu_B$ and $\theta = 100\text{K}$. This value of μ_{eff} is smaller than what is expected for $S = 5/2$. The reduction in magnetic moment is also consistent with the smaller value of the hyperfine field (492 KG) at $T = 14\text{K}$ compared to the crystalline

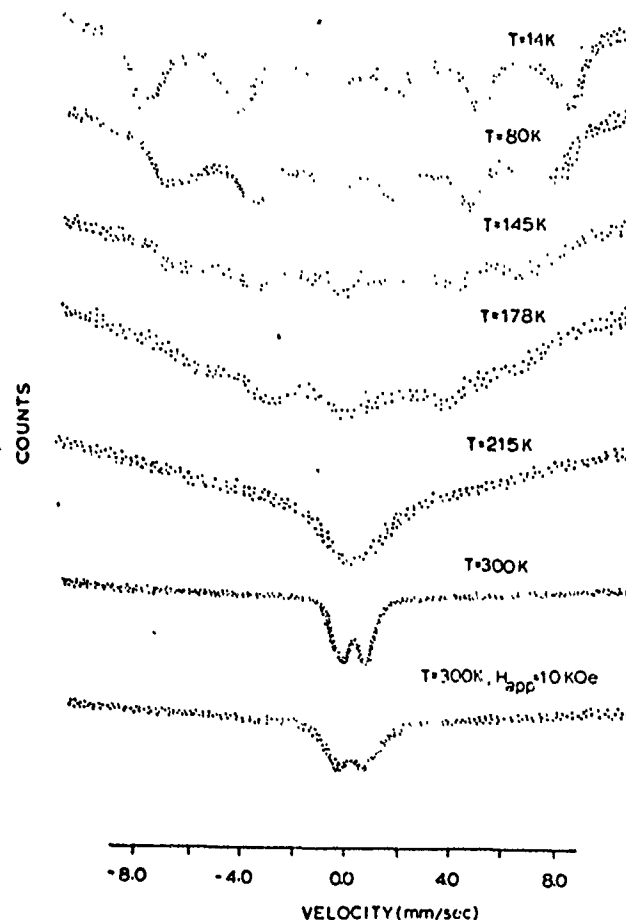


Figure 3. Mössbauer spectra of Fe_2O_3 thin film at various temperatures along with a spectrum at room temperature in an externally applied magnetic field perpendicular to the γ -ray beam.

oxides which show hyperfine field of 540KG at $T = 0\text{K}$. These same effects were observed for the amorphous Fe_2O_3 film discussed by van Diepen and Popma who observed a hyperfine field at $T = 5\text{K}$ of 469KG and a $\mu_{\text{eff}} = 3.0\mu_B$. They suggest that reduction in the hyperfine field from the crystalline oxides may be due to covalency. A more suitable explanation would be the mixing of various spin states. Fe^{3+} can exhibit $S = 1/2, 3/2$ and $5/2$ depending on the strength of the crystal field. It is therefore conceivable that the structure fluctuations within the material cause fluctuations in the strength of crystal field.

We may rule out superparamagnetism since the peak in the magnetic susceptibility at 225K is within 10K of the loss of magnetic order shown by the Mössbauer data. In addition, a Mössbauer spectrum of the film in an applied field at 300K shows no signs of hyperfine splitting which confirms that the Neel temperature is below 300K.

We also find no quadrupole interaction in our spectra indicating that θ (the angle between the hyperfine field and the electric field gradient) is averaged over the entire solid angle. This result is consistent with structure fluctuations in the film.

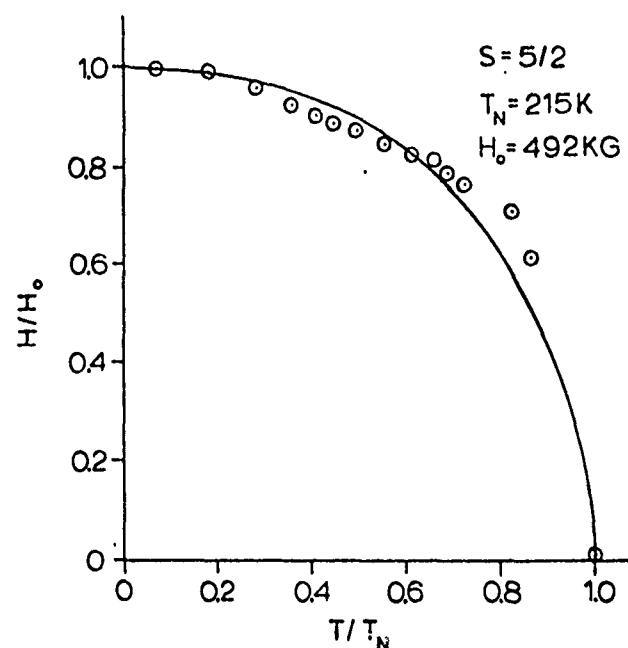


Figure 4. Reduced hyperfine field as a function of reduced temperature for Fe_2O_3 thin film. Solid curve is the Brillouin function for $S = 5/2$.

ACKNOWLEDGEMENTS

We wish to thank D. Barber for the transmission electron microscopy analysis of the films and A.M. deGraff for helpful discussions on the magnetic susceptibility and Mössbauer data. We also wish to acknowledge support for this work from the U.S. Army Research Office under Grant No. DAAG29-78-G-0033, Project No. P-15124-MS.

REFERENCES

- a. Address after 9/1/79, Wayne State University, Department of Physics and Astronomy, Detroit, Michigan.
1. W. Keune and V. Conser, *Thin Solid Films*, **7**, R7 (1971).
2. P. K. Gallagher, W. Robert Sinclair, R.A. Rastnacht and J. P. Luongo, *Thermochimica Acta*, **8**, 141 (1974).
3. Lina Ben-Dor, Eli Fischbein, Israel Feliner and Zvi Kalman, *J. Electrochem. Soc.: Solid State Science and Tech.*, **124**, 451 (1977).
4. A.M. van Diepen and Th. J. A. Popma, *Solid State Comm.*, **27**, 121 (1978).
5. R. Messier and R. Roy, *J. of Non-Cryst. Solids*, **28**, 107 (1978).

Low-Frequency Modes in Amorphous Boron-Rich Alloys

Jeffrey S. Lannin

Department of Physics, Pennsylvania State University, University Park, Pennsylvania 16802

and

Russell Messier

Materials Research Laboratory, Pennsylvania State University, University Park, Pennsylvania 16802

(Received 3 June 1980)

Raman scattering measurements are reported in amorphous boron-rich alloys of Y and La which indicate cagelike or in-band resonant modes not previously observed in non-crystalline solids. Low-frequency, intense Raman peaks indicate weak metal-boron bonding that is significantly reduced in the Y system. This is similar to the recent results in superconducting crystalline hexaborides and suggests that the anomalous transition temperature of YB_6 is a consequence of general bonding trends that persist in the amorphous state.

PACS numbers: 63.50.+x, 61.40.Df, 78.30.-j

While studies of amorphous solids have been concerned with the influence of light atoms in a host system, such as H in α -Si, the role of rather heavy atoms has not been pursued. In crystalline solids the addition of heavy atoms to a host matrix has been shown to result in the formation, under appropriate conditions, of in-band resonant modes. Such modes have been shown to correspond to a large amplitude of the heavy metal atom along with motions of the surrounding atoms.^{1,2} These modes, which are less localized than corresponding high-frequency light-atom local modes, have been shown to depend on weak coupling between host and defect atoms. An additional low-frequency defect mode that has been observed in relative "open" solids, such as clathrates, is that associated with a weakly coupled heavy atom. In this situation the motion has been considered as a "cagelike" translation of the impurity,³ though an alternative resonant mode picture may possibly be appropriate.² In this study we report on the formation and Raman scattering from amorphous B-rich alloys in which quite heavy atoms have been added. The resulting spectra indicate the formation of low-frequency modes that suggest either cagelike or resonant modes not previously observed in other amorphous solids studied to date. It is shown that the low-frequency modes are a consequence of weak metal-B bonding and not solely a function of metal-atom mass.

The systems chosen for the present study have compositions in the range of the corresponding crystalline metal hexaboride systems, MB_6 . These systems are quite interesting in that they are composed of a B network of octahedra which are strongly coupled and which together provide a

cagelike environment for the metal atoms. Group-IIIa hexaborides such as YB_6 and LaB_6 are particularly interesting in that they are superconductors with appreciable differences in their superconducting transition temperatures [$T_c(LaB_6) = 0.45$ K, $T_c(YB_6) = 7.1$ K]. Studies of the electronic energy band⁴ have indicated that the densities of states at the Fermi energy are rather similar and thus suggested that difference in the T_c values may primarily be due to low-frequency metal-atom motions. Recent neutron-scattering measurements⁵ have indicated differences in the low-frequency photon spectra of YB_6 and LaB_6 which are consistent with the substantial changes in T_c .⁶ The Raman scattering results in the amorphous counterparts discussed here also indicate similar differences in the low-frequency vibrational spectra that result from weak Y-B bonding. The results thus suggest that the anomalies in the crystalline superconducting transition temperatures are a general consequence of bonding trends that persist in the amorphous phase and do not require special lattice modes or long-range order.

Of additional interest in amorphous B-rich alloys is the extent to which the structure maintains B clusters, such as icosahedra or octahedra, which are present in the crystalline compounds.⁷ In a previous Raman scattering study⁸ in α -B it was shown that the spectra were consistent with short-range order similar to that of crystalline B implying half or full icosahedral-like bonding. While it is in general quite difficult to obtain information about structural order over an intermediate range in amorphous solids, the Raman results in the amorphous alloys are shown to be

consistent with the presence of B octahedral clusters.

Thin films of $\sim 0.5 \mu\text{m}$ thickness were prepared by rf sputtering from 2-in. polycrystalline targets of LaB_6 and SiB_6 and noncompacted YB_6 powder. A Materials Research Corporation system of base pressure $\sim 10^{-6}$ Torr was operated at 50 W power at an Ar pressure of 20×10^{-3} Torr and a substrate separation of ~ 5 cm. Based on the sputtering conditions the substrate temperature was estimated to be $< 75^\circ\text{C}$. Crystalline Si and glass substrates were employed for infrared measurements above 180 cm^{-1} and Raman measurements, respectively. A Spex third monochromator system was used for the Raman spectral determinations with 5145 and 4880-Å laser excitation. The relatively weak signal intensities prohibited a detailed analysis of the polarization of the scattered light. The composition of the films was estimated by Auger analysis which yielded ratios of $\text{B}/\text{La} \approx 6.0$ and $\text{B}/\text{Y} \approx 8.5$. The somewhat lower estimated concentration of Y than the stoichiometric value of 6 in the crystal is not expected to appreciably modify the Raman spectrum and its interpretation in any substantial fashion. Crystalline MB_6 materials are similarly found to be commonly metal-atom deficient, though in the present case this may be a consequence of the sputtering process. Infrared transmission spectra of B alloy films indicate a broad peak centered at 1350 cm^{-1} that is not observed in the Raman spectra. This is attributed to the presence of oxygen incorporated in the B network. Auger analysis indicates $\sim (3-6)\%$ oxygen. The absence of a distinct impurity associated Raman band is similar to the results in other amorphous solids and indicates an enhanced infrared absorption associated with B-O bonds. For higher oxygen concentrations the major influence in the Raman spectra appears to be a substantial background luminescence. The infrared and visible transmission spectra demonstrate the semiconducting nature of the amorphous materials in contrast to metallic $c\text{-LaB}_6$ and $c\text{-YB}_6$.

In Fig. 1 the Raman spectrum of $a\text{-B}$ is shown along with nonmetal alloy additions of Si and C. In pure $a\text{-B}$ the Raman spectrum indicates four distinct peaks at 335, 585, 750, and 1000 cm^{-1} . Recent neutron-scattering measurements⁹ in $a\text{-B}$ confirm that the peak positions occur near to the corresponding peaks in the phonon density of states. With the addition of C or Si the $a\text{-B}$ spectrum primarily broadens, though some changes occur in the low-frequency peak in $a\text{-SiB}_6$ as a

consequence of the heavier Si-atom mass. For these "covalent" alloys it is reasonable to assume that they are directly incorporated substitutionally in the $a\text{-B}$ network. In contrast, Fig. 2 indicates the effect of the introduction of the heavy metal atoms La and Y into $a\text{-B}$. The predominant effect seen here is the occurrence of an additional intense low-frequency phonon peak.

Before discussing this new low-frequency feature it is useful to note that the spectra of Fig. 2 may be approximately divided into four intervals,^{9,10} I-IV, with divisions at 175, 500, and 950 cm^{-1} . Interval I from $0\text{--}175 \text{ cm}^{-1}$ corresponds to acoustic modes in $c\text{-LaB}_6$ and $c\text{-YB}_6$ as well as in $c\text{-B}$. Interval II from $175\text{--}500 \text{ cm}^{-1}$ corresponds in the crystalline systems to rotational motions of B units, which in $c\text{-B}$ are icosahedra and in $c\text{-MB}_6$ are octahedra. For the $c\text{-MB}_6$ systems $M\text{-B}$ optic-mode contributions also occur in this range.^{9,11} Spectral ranges III and IV correspond to intraunit and interunit B motions, which in $c\text{-MB}_6$ systems and $c\text{-B}$ partially overlap. The higher frequency for the interunit vibrational bands are a consequence in the crystalline systems of shorter interunit bonds relative to those within the icosahedral

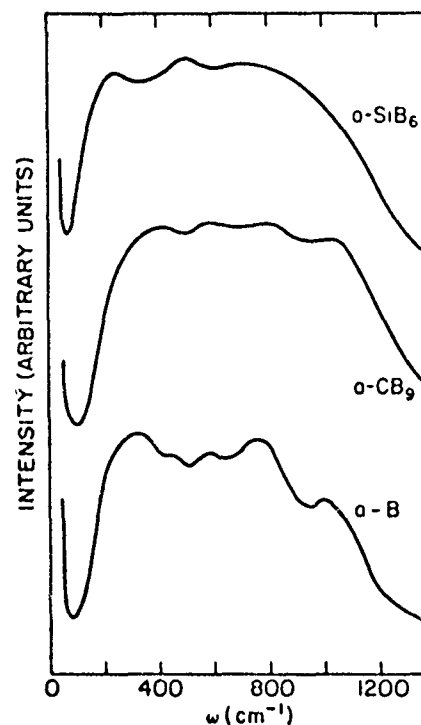


FIG. 1. Comparison of the Raman spectra of pure $a\text{-B}$ with $a\text{-SiB}_6$ and $a\text{-CB}_9$ at 300 K. A constant background has been subtracted to eliminate a high-frequency background contribution (Ref. 8).

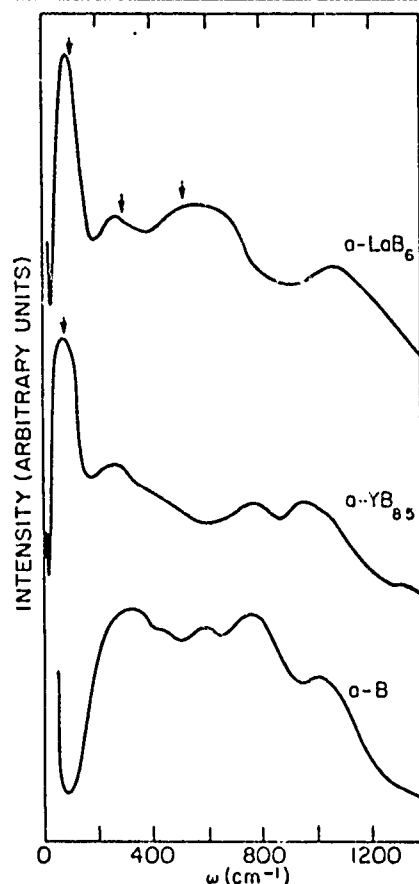


FIG. 2. Raman spectra for pure a -B and a - LaB_6 and a - YB_6 alloys at 300 K. As in Fig. 1 a high-frequency background has been subtracted. The vertical arrows indicate approximate peaks in the density of states for c - LaB_6 and c - YB_6 obtained by neutron scattering (Ref. 6).

or octahedral units.^{9,10} The spectra of Fig. 2 indicate that this approximate separation is still reasonable in the amorphous counterparts of the crystalline materials. In Fig. 2 the vertical arrows indicate peaks in the phonon density of states of the polycrystalline hexaborides as obtained to date from inelastic-neutron-scattering measurements.⁵ The correspondence between the amorphous and crystalline peaks suggests that coupled B octahedral units are also present in the amorphous systems. In particular, the peaks at $\sim 260 \text{ cm}^{-1}$ in the La and Y alloys correspond to a similar peak in c - LaB_6 which is interpreted as arising from rigid B octahedral rotations with essentially stationary metal atoms.⁵

For the low-frequency regime I it is observed that the Raman peak for the La system occurs above that for the lighter-, Y-atom case. Given the similar valence of La and Y this behavior is

surprising and indicates a weakening of the force constant by approximately a factor of two for the Y-B bond as compared to the La-B bond. This anomalous behavior of the Y-B force constant is analogous to that recently observed by Gompf in the crystalline MB_6 systems.⁵ The relative intensity and precise position of the peaks in the phonon density of states, $\rho(\omega)$, for the low-frequency modes in amorphous solids requires consideration of the effective frequency-dependent coupling parameter, $\bar{C}(\omega)$, in the phenomenological Raman relation¹² $I(\omega) \sim \omega^{-1}(\eta + 1)\bar{C}(\omega)\rho(\omega)$. The relatively rapid rise and fall of the low-frequency peak for a - LaB_6 and a - $\text{YB}_{6.5}$ implies that the peaks in $I(\omega)$ will occur near to that of $\rho(\omega)$ as $\bar{C}(\omega)$ will vary less rapidly than ω^2 .¹³ In a number of amorphous solids $\bar{C}(\omega)$ is found to vary roughly linearly with ω at low frequencies.¹⁴ For this choice of $\bar{C}(\omega)$ the relative intensities of the two lowest peaks in $\rho(\omega)$ are found to be similar to that shown in Fig. 2. Recent neutron-scattering measurements⁹ in a -B suggest⁸ for that system an alternative weak frequency variation of $\bar{C}(\omega)$ between ~ 200 – 600 cm^{-1} . For a similar choice of $\bar{C}(\omega)$ in a - LaB_6 , the intensity ratio of the two lowest peaks in $I(\omega)\omega/(\eta + 1)$ is found to be similar to that estimated for $\rho(\omega)$ in c - LaB_6 . For either of the above choices for $\bar{C}(\omega)$ the Raman spectra clearly demonstrate a substantial low-frequency contribution to the density of states.

The low-frequency modes observed in the La and Y alloys correspond to translational modes that primarily involve heavy-metal-atom motion. As peaks in the density of states of the crystalline and amorphous systems are similar this implies that the low-frequency modes are primarily determined by short-range order and metal-boron bonding. This indicates that differences in the superconducting transition temperature between c - LaB_6 and c - YB_6 , if primarily attributed to the phonon spectral variations, arise from general bonding interactions that do not require translational symmetry. It is interesting to note that preliminary measurements of amorphous group-IIIa metal alloys of Ca and Sr with B do not indicate the appreciable low-frequency scattering observed for the La and Y systems. As the mass of Sr is similar to that of Y this implies that the low-frequency peak in the density of states is not a consequence of the heavy metal-atom mass alone, but also requires weak metal-boron bonding. The results thus suggest the role of d electron bonding on the low-frequency phonons in the group-IIIa hexaborides. Increased participation

of d electrons in the Y alloy⁶ may in turn be responsible for the substantially lower force constant than in LaB_6 . Neutron scattering measurements clearly would be of interest to determine if the low-frequency phonon spectrum is also substantially modified in $c\text{-SrB}_6$.

The low-frequency modes in the Y and La alloys are thus somewhat analogous to defect-induced modes in crystalline systems which also require weak defect-host bonding.^{1,2} An alternative picture for these modes based on the crystalline analogues would correspond to cagelike modes in which a heavy, weakly coupled metal atom moves in a distorted cage of octahedrallike units of B. While the latter cagelike point of view appears most reasonable qualitatively, it is possible that the low-frequency modes also have some resonantlike character. The increased localization expected for amorphous solids may blur somewhat the distinction between these points of view. To date such resonant or cagelike modes have not been observed in amorphous solids, nor discussed theoretically.

In summary, the Raman spectra in boron-rich alloys of Y and La prepared by sputtering indicate vibrational spectra and bonding that are qualitatively different from other amorphous solids studied to date. The spectra suggest that coupled B clusters are present and that these define a network in which weakly coupled metal atoms are relatively free to vibrate. The results suggest a distorted local cagelike motion for the heavy metal atoms based on the correspondence to the low-frequency modes in the crystalline hexaborides. The presence of an increased density of low-frequency modes in the amorphous Y-B alloy relative to that of the La-B parallels similar changes in the crystalline counterparts. As these low-frequency modes have been suggested to play an important role in variation of T_c in general,¹⁵ as well as account for the large variation between $c\text{-LaB}_6$ and $c\text{-YB}_6$,⁶ the Raman spectra of the amorphous materials manifest these analogous states. This further implies that the

T_c anomaly is primarily a result of general bonding trends that persist in the noncrystalline, semiconducting systems.

We wish to thank Dr. L. Tongson for the Auger analysis, and Dr. F. Gompf for communicating his results prior to publication. This research was supported by the National Science Foundation under Grant No. DMR-79-08390 and by the U. S. Army Research Office under Contract No. DAAG-29-80-C-0089.

¹A. A. Maradudin, in *Localized Excitations in Solids*, edited by R. F. Wallis (Plenum, New York, 1968), p. 1.

²A. S. Barker, Jr., and A. J. Sievers, *Rev. Mod. Phys.* **47**, Suppl. 2, 1 (1975), and references therein.

³J. C. Burgiel, H. Meyer, and P. L. Richards, *J. Chem. Phys.* **43**, 4291 (1965).

⁴A. J. Arko, G. Crabtree, J. B. Ketterson, F. M. Mueller, P. F. Wall, L. R. Windmiller, and Z. Fisk, *Phys. Rev. B* **13**, 5240 (1976).

⁵F. Gompf, Teilinstitut Nukleare Festkörperphysik, Kernforschungszentrum Karlsruhe, Report No. 2670, 1978 (unpublished), p. 17.

⁶G. Schell, H. Winter, and R. Rietschel, Teilinstitut Nukleare Festkörperphysik, Kernforschungszentrum Karlsruhe, Report No. 2881, 1979 (unpublished), p. 59.

⁷J. L. Hoard and R. E. Hughes, in *The Chemistry of Boron and Its Compounds*, edited by E. L. Muetterties (Wiley, New York, 1967), p. 25.

⁸J. S. Lannin, *Solid State Commun.* **25**, 363 (1978).

⁹F. Gompf, Ref. 6, p. 41.

¹⁰W. Weber and M. F. Thorpe, *J. Phys. Chem. Solids* **36**, 967 (1975).

¹¹A large absorption cross section for ^{10}B has limited higher-frequency measurements in $c\text{-MB}_6$ systems to date.

¹²R. Shuker and R. W. Gammon, *Phys. Rev. Lett.* **25**, 222 (1970).

¹³A. Martin and W. Brenig, *Phys. Status Solidi (b)* **64**, 163 (1974).

¹⁴J. S. Lannin, *Phys. Rev. B* **15**, 3863 (1977).

¹⁵J. C. Phillips, in *Superconductivity in d- and f-Band Metals-1972*, edited by D. H. Douglas, AIP Conference Proceedings No. 4 (American Institute of Physics, New York, 1972), p. 339.

CLUSTER FORMATION IN AMORPHOUS AND POLYCRYSTALLINE THIN FILMS

S. V. KRISHNASWAMY AND R. MESSIER

Materials Research Laboratory, Pennsylvania State University, University Park, PA 16802 (U.S.A.)

S. B. McLANE, YEE S. NG AND T. T. TSONG

Department of Physics, Pennsylvania State University, University Park, PA 16802 (U.S.A.)

(Received October 6, 1980; accepted December 1, 1980)

Ions field evaporating from thin films r.f. sputter deposited onto molybdenum and tungsten tips in the presence of hydrogen are identified by employing an energy-focused atom probe field ion microscope. The existence of multiatomic clusters is unequivocally established. While the abundance of clusters for a well-developed tungsten tip is about 0.01%, polycrystalline sputtered metal films (nickel, gold and platinum) yield 2-5% cluster ions. For polycrystalline NiO films and amorphous germanium and silicon films, the yield of clusters increases up to about 20% and the cluster size also increases. The abundance of cluster ions is thus directly related to the degree of disorder of the materials. Study of cluster ion formation may shed light on the bonding mechanisms of thin film materials.

It is known that metals and alloys field evaporate as multiply charged monatomic ions¹⁻⁴. When they are field evaporated in the presence of an imaging gas like helium or neon, or a reactive gas such as O_2 or N_2 , in addition to the multiply charged metal ions, metal-gas molecular complex ions are obtained. Bulk materials in general have not been reported to contain clusters. Although multiatomic cluster ions have been reported in the field evaporation literature, the numbers observed have been rather too few for their presence to be established unequivocally.

One of the earliest reports was of CuBe_2^+ obtained by evaporating a CuBe alloy tip⁵; others were of As_2^+ from a GaAs tip⁶ and of CuH_2^+ , CuH_3^+ from a Be-Cu alloy tip⁷. Block⁸ found field desorption of ion species of S_2^+ , S_3^+ from a multilayer-covered sulfurized tungsten emitter using a quadrupole mass filter in the temperature range 150-500 K. When field evaporating a rhodium tip in H_2S gas, we could detect neither singly charged sulfur nor sulfur molecular ions at the high fields at which the substrate was evaporated⁹. Large fractions of cluster ions, however, have been observed when liquid metals such as gallium, indium, gold, cesium etc. are field desorbed¹⁰⁻¹¹. Ng *et al.*¹² have successfully obtained depth profiles of p-type semiconducting NiO formed by *in situ* oxidation of nickel and obtained NiO^+ and NiO_2^+ as predominant species as well as some multiply charged (threefold and fourfold) Ni_2O_3 ions.

Cluster formation has been reported for very thin films ($< 100 \text{ \AA}$) of gold obtained by thermal evaporation with the coalescence of such small clusters apparently playing an important role in the early growth stages of the film¹³. However, films greater than 1000 \AA are generally considered as extensions of bulk materials, albeit with one small dimension, and as such, cluster formation in thin films is not considered a general phenomenon. Feldman and Satkiewicz¹⁴ have observed clusters in amorphous and crystalline silicon films using a sputtering ion source. They find the percentage abundance to range from about 8% to about 0.1% for clusters with two atoms to clusters containing six atoms. In a similar secondary ion mass spectrometry (SIMS) experiment Herzog *et al.*¹⁵ obtained cluster ions containing up to 18 aluminum atoms by bombarding polycrystalline aluminum with 12 keV Xe^+ ions. While the ion cluster distribution was suspected to reflect the short range order, this was not established unambiguously.

In this paper we report that thin films, in general, contain a higher percentage of clusters than corresponding bulk materials and that the percentage depends on the history of preparation of the films. We established the existence of multiatomic clusters as field evaporation species obtained by evaporation of bulk tungsten tips as well as thin films of polycrystalline nickel, gold and platinum and amorphous germanium and silicon sputter deposited onto molybdenum and tungsten tips. Furthermore, this study provides a connection between crystalline, amorphous and liquid materials in their cluster formation behavior, thus shedding light on the bonding mechanism of these materials.

Recently, we employed the atom probe field ion microscope to characterize structurally thin films r.f. sputter deposited onto molybdenum tips^{16,17}. The field ion micrographs of metal and semiconductor films reveal void network structures, local ordering and atomic clusterings in the non-crystalline materials. Atomic layer depth profiling of these films indicates that the large ($\approx 100\text{--}500 \text{ \AA}$) voids, or low density regions, in amorphous germanium originate at the film-substrate interface and extend through the film, whereas interconnected voids, such as in nickel films, are in general smaller ($\approx 10\text{--}50 \text{ \AA}$).

The details of the field ion microscopy (FIM) and the energy-compensated time-of-flight atom probe can be found elsewhere¹⁸. A mass resolution of better than 1,200 can be routinely achieved for m/e up to 200. Moreover, the double-channel plate detector can eliminate after-pulses to fewer than one in 1000 primary events; thus an excellent rejection of artifacts is possible. Earlier atom probe studies employed either photographic techniques to record flight time, or in cases where electronic timers were used, the mass resolution was rather marginal to assign the masses to the cluster ions confidently. However, with our newly built electronic timers, a mass resolution of 1000 is achieved for ions up to an m/e ratio of 800; identification of heavy ions thus becomes much easier.

All the films except for a-Si (tungsten tip) were sputter deposited onto molybdenum FIM tips. Details of the sputtering system and the deposition procedure have been described elsewhere¹⁹. The preparation parameters during sputter deposition for all the films were 2.6 Pa argon gas pressure, 50 W r.f. power and 50–55 mm substrate-to-target distance. The deposition time was controlled to obtain film thickness estimated to be in the range 2000–4000 Å. The films after being transferred to the atom probe were imaged and field evaporated at 85 K in H_2 or an $\text{H}_2 + \text{Ne}$

mixture at an operating gas pressure of 5×10^{-4} to 6×10^{-3} Pa for H_2 and 1×10^{-4} Pa for neon.

On field evaporating a well-developed tungsten tip in vacuum at about 85 K, we found that about 0.3% of the ions detected from (223) crystallographic regions are cluster ions such as W_5^{2+} , W_3^+ and W_2^+ . However, out of 10^4 ions detected from (011) regions of tungsten, not a single cluster ion was detected. This indicates that cluster formation has a higher probability in a high index plane than in a low index plane for a well-developed tip.

A larger fraction of multiatomic cluster ions is found for polycrystalline metallic films and amorphous semiconductor films. Table I summarizes various species obtained on field evaporating thin nickel, platinum and gold films. Platinum films evaporated mostly as doubly charged. This behavior is similar to that reported for bulk platinum tips. Clusters containing up to three platinum atoms are observed as field evaporation species. Also three cluster ions were observed when a total of 100 field-evaporated ions were counted. Thus the abundance of cluster ions is $3 \pm 1.7\%$.

Gold films on molybdenum tips often field evaporate in bursts, similar to our earlier observations of bulk gold tips. Gold films evaporated as both singly and doubly charged ions in equal abundance. As can be seen from Table I, clusters containing up to nine gold atoms are observed for the sputtered gold film. From a total of 270 particle counts we observe the abundance of cluster formation to be $5.2 \pm 1.4\%$. Takeuchi *et al.*^{1,3} from transmission electron microscopy studies observed as much as 1% of all atoms captured by the substrate to form clusters with the cluster size varying from five to ten atoms.

TABLE I

ION SPECIES OBTAINED ON THE FIELD EVAPORATION OF NICKEL, GOLD AND PLATINUM FILMS DEPOSITED ON MOLYBDENUM TIPS

Nickel	Gold	Platinum
H^+ , H_2^+ , OH^+	H^+ , C^+ , CH^+	H^+ , N^+ , O^+
H_2O^+ , Ni^{2+} , NiH^{2+}	O^+ , H_3O^+ , Ar^{2+}	O_2^+ , Ar^+ , Pt^{2+}
NiH_2^{2+} , $(NiO)^{2+}$, $(NiOH)^{2+}$	O_2^+ , Ar^+ , $(Au_2)^{3+}$	Pt^+ , Pt_2^+ , $(PtO_3)_2^+$
O_2^+ , $Ni_2O_3^{4+}$, $NiCO^{2+}$	AuO^{1+} , Au^{2+} , $(AuH)^{2+}$	Pt_3^+ , $(Pt_3N)^+$
$(Ni_2O_3)^{1+}$, Ni^+ , NiH^+	$(Au_3O_3)^{4+}$, $(Au_3O_4)^{2+}$, Au^+	
NiH_2^+ , NiO^+ , $Ni(OH_2)^+$	$AuAr^+$, $(Au_3)^{2+}$, $(Au_3O_9)^{2+}$	
$(NiH_2)_3^+$, Ni_3^+ , Ni_6^+	$(Au_2O_4)^+$, Au_3^+ , $(Au_8O_{10})^+$	
	$(Au_9O)^{2+}$	

For the nickel film, singly and doubly charged ions are the predominant species. Out of a total of 150 signals, there were four corresponding to nickel clusters, resulting in an abundance of about $2.7 \pm 1.3\%$. Cluster species containing up to six nickel atoms were detected. However, when the nickel films were prepared in an $Ar-O_2$ mixture the cluster abundance increased. For instance, when sputtered in a gas mixture of 2.6 Pa $Ar + 2.6 \times 10^{-3}$ Pa O_2 the abundance increased to $7.5 \pm 2\%$ (12 out of 160 particle counts). When films prepared with 2.6 Pa $Ar + 0.6$ Pa O_2 were field evaporated we obtained eight cluster ions out of a total of 95 particles, representing $8.5 \pm 2.9\%$ abundance for clusters. Also, we could detect larger clusters containing up to 37 nickel atoms at the latter gas mixture condition. Recently, Upton and

Goddard¹⁹ have made first-principle calculations of nickel clusters containing up to 87 atoms. In their study, they point out the relevance of such clusters in chemisorption. The fact that we have observed clusters containing up to about 37 nickel atoms is consistent with these calculations and may have some significance in catalysis. Figure 1 is a field ion micrograph of a polycrystalline NiO_x film imaged in 10^{-3} Pa H_2 at 85 K in which interconnected void structures and atomic clusters can be clearly seen. Such void structures have also been observed for nickel, gold, and platinum, germanium and silicon films^{16, 17, 20}.

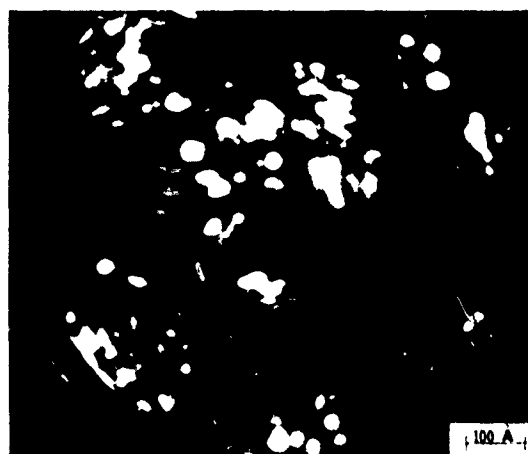


Fig. 1. Field ion micrograph of a polycrystalline NiO_x film deposited onto a molybdenum tip and imaged in 10^{-3} Pa H_2 .

We have been successful also in pulse evaporating sputtered thin films of a-Ge and a-Ge:H. Atom probe analysis of these films in H_2 gives signals corresponding to both singly and doubly charged germanium. Upon field evaporation of a-Ge a large fraction of the signals appeared as various oxides of germanium, such as GeO^+ , GeO_2^{3+} , GeO_3^+ etc. Further, for a-Ge:H films a significant number of clusters of germanium hydrides and hydroxides were obtained as evaporation species, in addition to the oxides. For example, mass signals up to 400 amu representing Ge_2H_2^+ , Ge_3H_6^+ , Ge_3H_9^+ , $\text{Ge}(\text{OH})^+$, $\text{Ge}(\text{OH})_2^+$, $\text{Ge}(\text{OH})_3^+$ and Ge_2O_2^+ were observed. These oxides and hydroxides may be due, in part, to post-deposition interaction of the film with oxygen and water vapor through void, or low density, regions^{21, 22}. The abundance of these clusters is $24 \pm 8\%$. This clearly establishes the presence of clusters which have been identified by us previously in the field ion images of a-Ge and a-Ge:H¹⁷. It is noted in a mass spectrometric analysis of evaporated germanium vapor species that, in addition to single germanium atoms, a great number of clusters consisting of two, three, four and five germanium atoms exist²³. Although the results are preliminary, clustering effects can also be seen on field evaporating a-Si as well as a-Si:H sputtered films.

A well-developed tip with a field-evaporated end form yields only up to 0.3° clusters with cluster formation having a higher probability in a high index plane than in a low index plane. However, when an as-etched tungsten tip (that exposes a

rather disordered surface) is field evaporated, the cluster yield is about $1-2\%$. Field-evaporated polycrystalline metallic films have cluster yields of $2-5\%$ while amorphous (disordered) semiconducting films give cluster yields as high as 20% . In liquid metals, the yield has been reported by Evans and Hendricks¹⁰ to be as high as 50% for gallium and indium, with cluster sizes of up to five gallium atoms. Clappitt and Jefferies¹¹ have also observed signals of Cs_3^+ in the field evaporation of liquid cesium. From the above results and discussion there appears to be a close relation between the degree of disorder of a material and the cluster ion formation upon field evaporation of the material; the larger the disorder, the larger the fraction of the atoms forming ion clusters and the number of atoms in the clusters. Also, the fact that the cluster yield for field evaporation of the bulk tips is less than 0.3% indicates directly the atomic cluster formation within these thin films and bulk-disordered materials.

We believe that our results may shed some light towards understanding the atomic bonding scheme in disordered and amorphous thin films and its relationship to the field evaporation behavior in such films. We have established the existence of multiautomic clusters in thin amorphous semiconducting films and polycrystalline metallic films. It is shown that such clusters mark a clear distinction between thin films and bulk materials and may account in part for differences in properties between these two classes of materials. Some recent results by other researchers support this conclusion^{24,25}. For instance Hebard and Vandenberg²⁴ have demonstrated the presence of clusters even in thin ($\sim 300 \text{ \AA}$) granular lead films and point out that these clusters play an important role in maintaining Josephson coupling across regions of the films containing a relatively large number of grains.

ACKNOWLEDGMENTS

We wish to acknowledge support for this work from the U.S. Army Research Office under Grant DAAG29-80-C-0089 and from the U.S. National Science Foundation under Grant DMR-7904862.

REFERENCES

1. F. W. Muller, J. A. Pautz and S. B. McLane, *Rev. Sci. Instrum.*, **39** (1968) 53.
2. F. W. Muller and I. F. Tsong, *Prog. Surf. Sci.*, **4** (1973) 1.
3. F. W. Muller, S. V. Krishnaswamy and S. B. McLane, *Surf. Sci.*, **23** (1970) 110.
4. S. S. Brenner and J. T. McCloskey, *Surf. Sci.*, **23** (1970) 88.
5. E. W. Muller and S. V. Krishnaswamy, *Phys. Status Solidi A*, **3** (1970) 27.
6. T. T. Tsong, Yee S. Ng and A. J. Melmed, *Surf. Sci.*, **77** (1978) L187.
7. S. R. Goodman, S. S. Brenner and J. R. Low, *Metall. Trans.*, **4** (1973) 2371.
8. J. H. Block, in A. W. Czanderna (ed.), *Methods of Surface Analysis*, Elsevier, New York, 1975, Chap. 9.
9. E. W. Muller and S. V. Krishnaswamy, in L. H. Lee (ed.), *Characterization of Metal and Polymer Surfaces*, Academic Press, New York, 1977, p. 42.
10. C. A. Evans and C. D. Hendricks, *Rev. Sci. Instrum.*, **43** (1972) 1527.
11. R. Clappitt and D. K. Jefferies, *Nucl. Instrum. Methods*, **149** (1978) 739.
12. Yee S. Ng, S. B. McLane and I. F. Tsong, *J. Appl. Phys.*, **49** (1978) 2517.
13. H. Takeuchi, H. Fujimoto, K. Ishii and K. Knaosita, *Thin Solid Films*, **57** (1979) 29.
14. C. Feldman and F. G. Satkiewicz, *J. Electrochem. Soc.*, **120** (1973) 1111.

- 15 R. F. K. Herzog, W. P. Poschenreider and F. G. Satkiewicz, *Radiat. Eff.*, **18** (1973) 199.
- 16 S. V. Krishnaswamy, R. Messier, Yee S. Ng and T. T. Tsong, *Appl. Phys. Lett.*, **35** (1979) 870.
- 17 S. V. Krishnaswamy, R. Messier, Yee S. Ng, T. T. Tsong and S. B. McLane, *J. Non-Cryst. Solids*, **35-36** (1980) 531.
- 18 E. W. Müller and S. V. Krishnaswamy, *Rev. Sci. Instrum.*, **45** (1974) 1053.
Yee S. Ng and T. T. Tsong, *Surf. Sci.*, **78** (1978) 419.
- 19 T. H. Upton and W. A. Goddard, *J. Vac. Sci. Technol.*, **16** (1979) 531.
- 20 S. V. Krishnaswamy, D. J. Barber, R. Messier and T. T. Tsong, unpublished work.
- 21 L. R. Gilbert, R. Messier and R. Roy, *Thin Solid Films*, **54** (1978) 149.
R. Messier, S. V. Krishnaswamy, L. R. Gilbert and P. Swab, *J. Appl. Phys.*, **51** (1980) 1611.
- 22 D. A. Anderson, G. Moddel, M. A. Paesler and W. Paul, *J. Vac. Sci. Technol.*, **16** (1979) 906.
- 23 A. Barna, P. B. Barna, Z. Bodo, J. F. Pocza, I. Pozsgai and G. Radnóczy, in J. Stuke and W. Brenig (eds.), *Proc. 5th Int. Conf. on Amorphous and Liquid Semiconductors*, Garmisch-Partenkirchen, F.R.G., Taylor-Francis, London, 1973, p. 109.
- 24 A. F. Hebard and J. M. Vandenberg, *Phys. Rev. Lett.*, **44** (1980) 50.
- 25 E. Smanek, *Phys. Rev. Lett.*, **38** (1977) 1161.

FINE STRUCTURE OF GOLD PARTICLES IN THIN FILMS PREPARED BY METAL-INSULATOR CO-SPUTTERING

R. A. ROY AND R. MISSIER

Materials Research Laboratory, The Pennsylvania State University, University Park, PA 16802 (U.S.A.)

J. M. COWLEY

Department of Physics, Arizona State University, Tempe, AZ 85281 (U.S.A.)

(Received December 1, 1980; accepted January 5, 1981)

Thin films containing a homogeneous dispersion of small gold particles were formed by co-sputtering composite targets of gold with Al_2O_3 and polyester in separate experiments. The nanostructure of these films was studied using transmission electron microscopy (TEM) and high resolution scanning-transmission electron microscopy (STEM). Diffraction data obtained from STEM show the gold islands to be simple and multiply twinned crystallites even in particles as small as 15 Å across. The existence of such fine structure in sputtered gold particles is consistent with the earlier TEM work reported by other workers for gold particles grown from colloidal solutions and by evaporation onto single-crystal substrates.

1. INTRODUCTION

The structure of small metal crystallites has been examined by several workers over the last 15 years. Uyeda *et al.*¹ reported observation of twinned crystallites in gold sol particles prepared from several different colloidal solutions. The particle sizes ranged from 50 to 150 Å and high resolution transmission electron microscopy (TEM) revealed that each particle consisted of smaller crystallites. Diffraction contrast analysis revealed the crystallites to be parallel or radial twins. They proposed that the formation of such twinned structures in f.c.c. metal particles results from the interaction of small nuclei before crystal growth occurs. Further, they suggested that the type of twinned structure formed depends on the geometry of the elementary nucleus. Ino² developed the model of a metastable icosahedral nucleus forming in small metal particles which show twin formation. Uyeda *et al.* noted that if such nuclei exist they will probably lead to the formation of multiple twins whereas if the stable cube-octahedral nucleus is formed the growth of simple twins is more likely. If the particle growth is rapid, the metastable nucleus will remain intact and the growth of multiple twins will occur. If the particle growth is slow, a transition from icosahedral to cube-octahedral form will take place favoring simple twin growth or none at all. Uyeda *et al.* also reported that particles which formed rapidly in sodium citrate sols showed an abundance of multiple twins, whereas those formed from slowly reacting Faraday sols showed mostly simple twins.

A number of authors³⁻⁸ have found the same type of multiply twinned particles of gold and other f.c.c. metals in thin layers grown epitaxially on single-crystal supports, including alkali halides, mica and magnesium oxide. The advantage of a single-crystal substrate is that diffraction patterns can be obtained from assemblies of well-oriented crystallites and that high resolution electron micrographs may be obtained from crystallites having well-defined orientations. Analysis of the forms of the particles has been made using lattice fringe imaging, selected zone dark field imaging, weak beam thickness fringe imaging, imaging of moiré patterns and selected area electron diffraction. It has been concluded^{6,7} that the misfit inherent in the formation of regular decahedral and icosahedral particles is taken up by uniform strain of the component crystallites resulting in deformations of the f.c.c. gold lattice to give rhombohedral or orthorhombic lattices. However, dislocations which may accommodate much of the strain have been observed in some cases⁸. In addition, Gillet⁹ has observed a gap in larger gold crystallites which he attributes to the transition from icosahedral structure to f.c.c. structure during particle growth. Moreover, several authors¹⁰⁻¹² have done model calculations to estimate the stability of different structures in particles containing a small number of atoms. They all concluded that the icosahedral structure is more stable than the f.c.c. structure for very small metallic particles such as gold.

One difficulty associated with the use of small particles grown epitaxially on a single-crystal support is the uncertainty about the influence of the substrate on the initial form and growth of the particles. A limitation of all the quoted work is that the particles investigated are mostly greater than 50 Å in diameter and are often as large as 200 Å so that the information on the initial forms of the particles is limited.

The preparation of novel "hybrid" solid materials involves the fine mixing of two or more components consisting of metals, ceramics or polymers. In the past it has been shown that r.f. sputtering offers a uniquely versatile tool to achieve such fine mixing. Sputtered materials often exist in a metastable state and frequently appear amorphous by X-ray diffraction. In this study we report the preparation of composite metal-containing films by co-sputtering, the structure of these films and the fine structure of the metallic component. The gold particles were dispersed in composite films whose matrix component was either sputtered Al_2O_3 or sputtered polyester (EKONOL). The microstructure of the films was probed initially using X-ray diffraction and TEM. The presence of small gold islands (approximately 30 Å in diameter) throughout the films prompted a detailed look at the fine structure of the particles using high resolution scanning-transmission electron microscopy (STEM) and the microdiffraction methods which allow diffraction patterns to be obtained from regions 20 Å or less in diameter. The results of our investigation are compared with earlier work on f.c.c. metal particles by other authors.

2. EXPERIMENTAL DETAILS

Ceramic-metal films were prepared by r.f. sputtering of a composite Al_2O_3 -Au target. The target was a hot-pressed Al_2O_3 disk 12.5 cm in diameter on an aluminum backing plate with an area of gold foil 0.5 cm square placed near the edge. The target was sputtered in an r.f. diode unit in which the power was 50 W and the partial pressure of oxygen and argon was 20 mTorr each. The distance between the target

and the substrates was 4 cm. The substrates were a series of eight 3-mm copper microgrids with carbon film supports arranged in a line running underneath the line connecting the gold piece to the Al_2O_3 target center. The geometry is shown in Fig. 1. The films obtained varied in gold composition according to the proximity of the substrate to the gold part of the target.

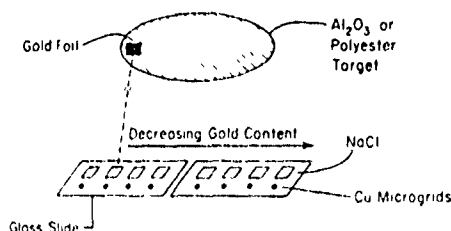


Fig. 1 Geometrical arrangement of the composite sputtering target and the substrates

Sputtered polyester-Au films were made using a polyester (EKONOL) target 9 cm in diameter on which a square of gold foil 0.25 cm^2 in area was placed at one edge. (EKONOL is a trade name of Carborundum.) Two different sets of substrates were used. In the first test a series of eight copper microgrids with carbon film supports was used. The substrates in the second test were a series of eight flat pieces of NaCl arranged in a geometry similar to the Al_2O_3 -Au sputtering test. After the films had been deposited at a power of 50 W and a pressure of 25 mTorr of argon, the NaCl substrates were dissolved and the films floated onto copper microgrids. In addition, glass substrates were used to collect film for X-ray diffraction analysis.

Both sets of films were examined in an HB-5 scanning transmission electron microscope equipped with an optical analyzer system¹³. The polyester Au films were also examined in a conventional transmission electron microscope (Philips model EM200).

3. RESULTS

X-ray diffraction patterns produced no sharp peaks in any of the samples. Figure 2 shows TEM micrographs of sputtered polyester Au films prepared under the conditions noted above. The images show that the size and number of gold particles decrease as the concentration of gold in the film decreases. The samples are referenced to a substrate position directly underneath the gold target. The particle size ranges from about 80 Å down to 15-20 Å. Of interest in our study is the fine structure of the individual gold particles in the films. The small size of the gold particles required a high resolution technique to study the fine structure of the islands. The STEM system developed at Arizona State University was particularly suited to the study of the sputtered gold films.

In an STEM instrument, a microdiffraction pattern is formed in the detector plane for each position of the incident beam on the specimen. The diameter of the region giving the diffraction pattern is comparable with the image resolution obtainable with the instrument and so approaches 5 Å for modern dedicated STEM instruments. In most STEM instruments the diffraction pattern from a particular

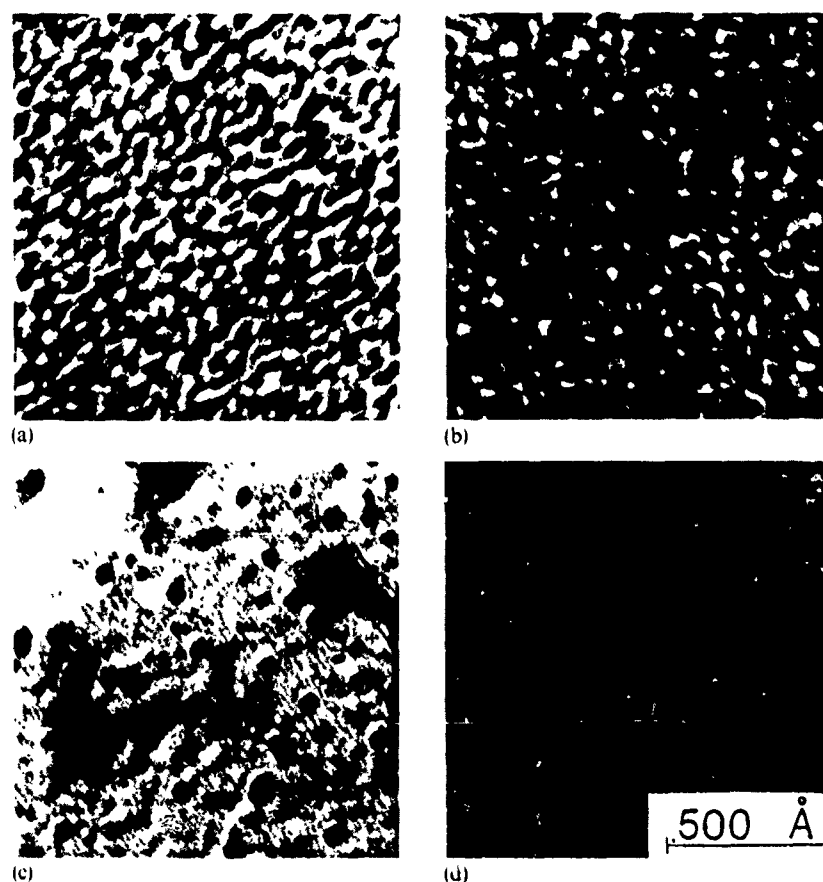


Fig. 2. Conventional TEM micrographs of sputtered polyester-Au films showing variation of the microstructure with the gold content, taken from substrate positions as follows: (a) $R = 0$ (directly underneath the gold target); (b) $R = 14$ mm; (c) $R = 42$ mm; (d) $R = 56$ mm.

specimen area, obtained when the beam is held stationary on the specimen, is recorded by using post-specimen deflection coils to scan the diffraction pattern over the entrance aperture to the energy analyzer or over an aperture placed immediately in front of a scintillator-photomultiplier detector. This recording method is so inefficient that although patterns from regions about 20 \AA in diameter have been recorded the recording time is of the order of 1 min and the signal-to-noise ratio is poor.

In the instrument at Arizona State University an optical system has been added in which the diffraction pattern formed on a fluorescent screen is amplified by an image intensifier and then viewed with a low light level television (TV) camera so that diffraction patterns from regions less than 20 \AA in diameter can be recorded as single frames of a video tape recording, *i.e.* at the rate of $30 \text{ patterns s}^{-1}$, or photographed from a TV display screen in a fraction of a second. Thus it has been possible to record diffraction patterns from very small (15 \AA) individual gold particles or from individual small areas within larger gold particles.

If an objective aperture of 10 or $20 \text{ }\mu\text{m}$ diameter is used in the STEM instrument

in order to obtain reasonably small diffraction spots such as those shown in Figs. 3–5, the resolution of the image formed when the electron probe is scanned over the specimen is necessarily limited to about 15 or 10 Å respectively. This gives fuzzy low contrast images of the small gold particles. The procedure adopted was, therefore, to obtain a high resolution image with a large (60 μm) objective aperture (Fig. 3(a)), to stop the beam at a point on a small crystal (indicated by a marker on the display screen), to insert a small objective aperture to obtain the convergent beam microdiffraction pattern (Fig. 3(b)) and then to record the image using the same small objective aperture in order to ensure that within the resolution of the low resolution image formed no relative movement of the beam and the specimen had resulted from the change of apertures or from the drift of the specimen. Alternatively the sequence of operations could be reversed.

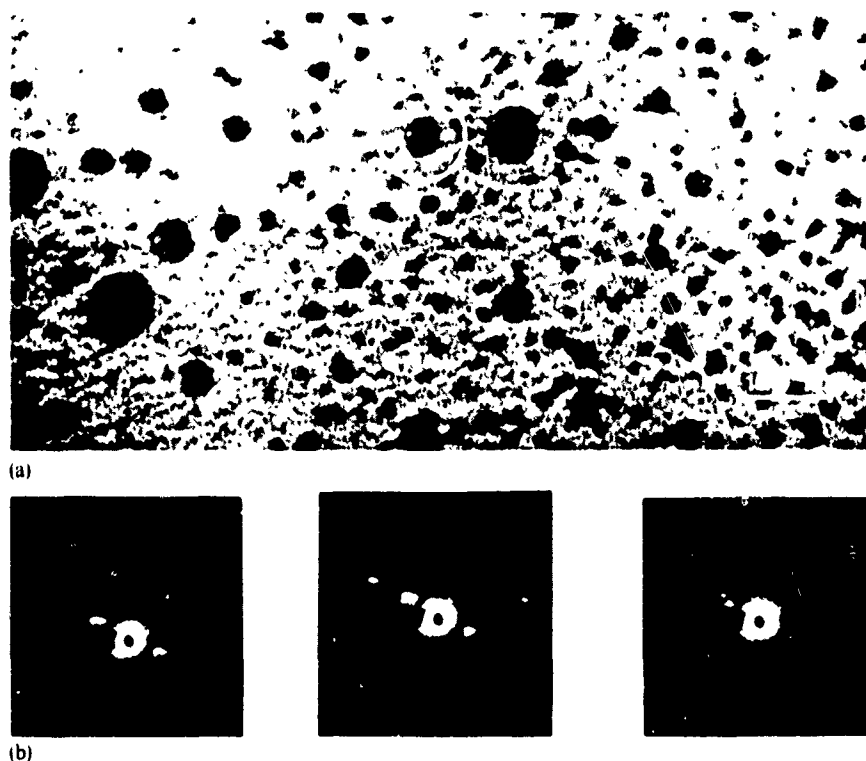
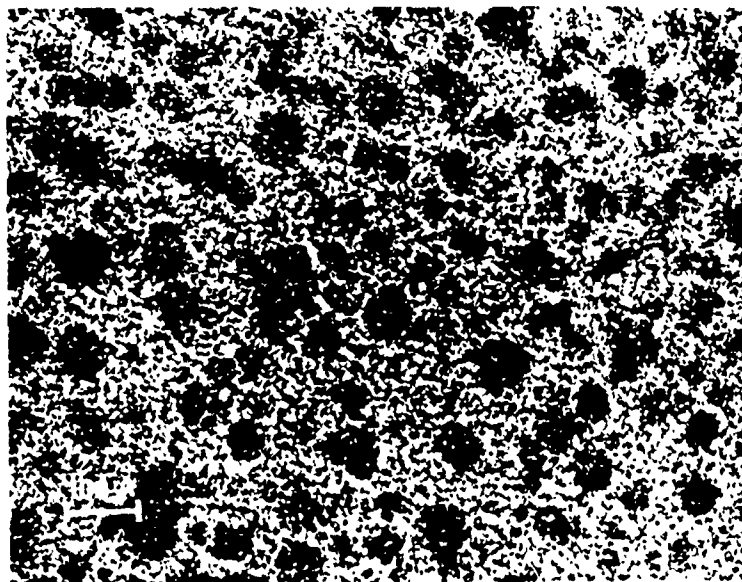


Fig 3 (a) Bright field STEM image of a thin polyester-Au film; (b) three microdiffraction patterns obtained as the beam is traversed across the 30 Å diameter particle circled in the image.

For relatively thick (200–300 Å) Au-Al₂O₃ and Au-polyester films, the STEM images show evidence of a high concentration of gold particles but the very strong phase-contrast “noise” from the amorphous embedding material prevented any clear high resolution imaging of the shapes or details of the gold particles (see Fig. 4(a)). Even so, microdiffraction patterns from the gold particles were readily obtained, showing clear evidence of their crystallinity and in many cases of their multiple-twin structure (Figs. 4(b) and 4(c)).



(a)



(b)

Fig. 4. (a) Bright field STEM image of a thick polyester-Au film with a strong background of phase-contrast noise due to the amorphous polyester film. (b) microdiffraction patterns from individual gold particles 50 Å or less in diameter showing clear evidence of multiple twinning

For thin Au-polyester films much clearer images of the gold particles could be obtained (Fig. 3(a)) and a less ambiguous correlation of diffraction patterns with particle images was possible.

The observations of diffraction patterns from individual gold particles may be summarized as follows.

- (1) For relatively large particles, 50–100 Å in diameter, the diffraction patterns usually showed clear evidence of multiple twinning, giving complicated patterns of spots such as those shown in Fig. 5(a), which resemble one of the patterns predicted by Yang *et al.*¹⁴ for a decahedral particle.
- (2) Some particles gave patterns explainable in terms of simple f.c.c. untwinned crystals such as those shown in Fig. 5(b).
- (3) Many small particles gave patterns containing spots from crystallites in at

least two twinned orientations plus continuous streaks of considerable intensity (see Fig. 5(c)) such as could be attributed to planar faults (or twin planes) which occupy a relatively large fraction of the particle volume.

(4) Pairs or triplets of spots were frequently observed (Figs. 3(b) and 5(d)). As the beam is moved from one side of a crystal to the other, each pair or triplet coalesces into a strong central spot and then separates again into a pair or triplet, usually with a rotation of the group. These splittings of the spots are a consequence of interference effects occurring within a coherent convergent incident beam which will be described in a subsequent publication. They should not be interpreted as primarily due to structural features of the gold particles.

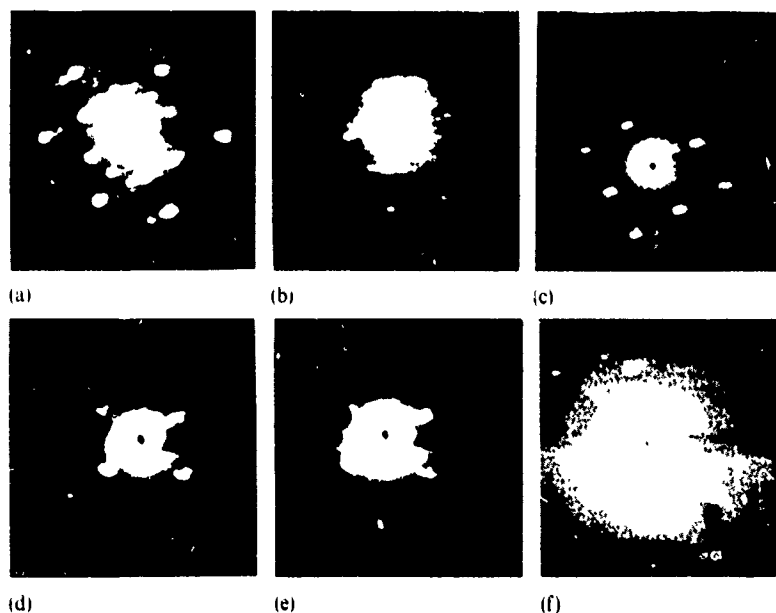


Fig. 5. Microdiffraction patterns from small gold particles showing the multiple orientations expected from the multiply twinned models of their structure (in (a) and (b)) and the doublets (f) and triplets ((d) and (e)) of spots. Patterns (d) and (e) were obtained from opposite sides of the same particle. The pattern (c) comes from an apparently untwinned crystal.

The detailed interpretation of the diffraction patterns in terms of particle structure and the comparison with the predictions from the proposed multiple-twin models is a matter for detailed study and future publication. However, the conclusion which can be drawn immediately is that a higher proportion of the crystallites, including the very small ones (less than 30 Å in diameter), have a multiply twinned structure in both the Au-Al₂O₃ and Au-polyester preparations.

4. DISCUSSION

The r.f. sputtering of gold combined with Al₂O₃ or with EKONOL polyester has produced films with small gold particles finely dispersed in two completely different non-conducting matrices. These dispersions contain a high proportion of

particles smaller than those found in discontinuous epitaxial deposits on single-crystal substrates³⁻⁸ or sol particles formed in colloidal solutions¹. It is of interest that despite the difference in growth method and environment the particles prepared in the present study are similar to those made by other methods. The growth of the gold particles during sputtering is subject to several factors. In the r.f. plasma positive argon ions strike the target and eject atoms, ions or clusters of the target material into the vapor phase. When those vapor species deposit at the substrate they experience a fast quenching rate of the order of 10^9 K s^{-1} . Additionally, electron and ion bombardment of the growing film surface, both of which are highly dependent on preparation conditions, can alter the adatom surface mobility and in turn the nucleation and growth processes. These properties can be manipulated to produce amorphous films from material generally crystalline such as Al_2O_3 , CdTe, Fe-B alloys and others.

The fact that the gold particles formed from co-sputtering experiments exhibit multiply twinned structures even in such a highly non-equilibrium process may be interpreted in different ways. It has been noted earlier that model calculations predict that such arrangements of atoms are stable for particles containing several thousand atoms or fewer¹⁰⁻¹². By simple calculation it can be shown that a 40 Å gold sphere contains about 1800 atoms. Thus, the smaller particles (less than or equal to 40 Å) in the composite films which are multiply twinned are well within the size range for which such a structure has been calculated to be stable. Hence the fact that even particles formed in a highly metastable process such as sputter deposition have this structure can be interpreted as evidence of the stability of the multiply twinned arrangement with respect to the f.c.c. arrangement. However, as previously noted, the detailed interpretation of the STEM diffraction patterns of the sputtered gold particles requires further study because several novel features of these patterns can be understood only in terms of unfamiliar concepts. However, conclusions (1)-(4) of Section 3 are not subject to uncertainty for this reason. The complexity and diversity among the diffraction patterns obtained for the different particles indicates directly that no single structure type is present. Nor does the type of pattern appear to be related to the size of the particle over the 15-100 Å size range studied. The fact that different structures appear to be present in particles of the same size may well be the result of the complexity of parameters in the sputtering process. In addition, the insulating matrix surrounding the gold particles should have an influence on their growth and resulting structure.

5. SUMMARIZING REMARKS

Very small gold particles were prepared by co-sputtering gold with insulating materials which served to disperse it into islands during film growth. By variation of the amount of insulator codepositing with the gold on the substrate the average size of the gold particles was varied. Particles 15-100 Å in diameter were studied using a STEM instrument equipped with an optical analyzer¹³. The fine structure of these particles was probed using diffraction modes which revealed a complex and varied structure in the different particles. Our preliminary analysis showed that a large proportion of the particles have a multiply twinned structure similar to that of small gold particles grown by other methods.

ACKNOWLEDGMENTS

This work was supported by the U.S. Army Research Office under Contract Nos. DAAG29-78-0033 and DAAG29-80-0089. The use of the Facility for High Resolution Electron Microscopy, supported by the National Science Foundation Regional Instrumentation Program under Grant No. CHE7916098, is also gratefully acknowledged.

REFERENCES

- 1 N. Uyeda, M. Nishino and E. Suito, *J. Colloid Interface Sci.*, **43** (1973) 276.
- 2 S. Ino, *J. Phys. Soc. Jpn.*, **21** (1966) 346.
- 3 S. Ino and S. Ogawa, *J. Phys. Soc. Jpn.*, **22** (1967) 1356.
- 4 J. G. Allpress and J. V. Sanders, *Surf. Sci.*, **7** (1967) 1.
- 5 K. Yagi, K. Takayanagi, K. Kobayashi and G. Honjo, *J. Cryst. Growth*, **28** (1975) 117.
- 6 K. Heinemann, M. J. Yacaman, C. Y. Yang and H. Poppa, *J. Cryst. Growth*, **47** (1979) 177.
- 7 M. J. Yacaman, K. Heinemann, C. Y. Yang and H. Poppa, *J. Cryst. Growth*, **47** (1979) 187.
- 8 L. D. Marks, A. Howe and D. J. Smith, in T. Mulvey (ed.), *Electron Microscopy and Analysis 1979*, The Institute of Physics, Bristol, 1980, p. 397.
- 9 M. Gillet, *Surf. Sci.*, **67** (1977) 139.
- 10 J. G. Allpress and J. V. Sanders, *Aust. J. Phys.*, **23** (1970) 23.
- 11 Y. Fukano and C. M. Wayman, *J. Appl. Phys.*, **40** (1969) 1656.
- 12 S. Ino, *J. Phys. Soc. Jpn.*, **27** (1969) 941.
- 13 J. M. Cowley, in O. Johari (ed.), *Scanning Electron Microscopy 1980*, Vol. 1, Scanning Electron Microscopy Inc., AMF O'Hare, IL, 1980, p. 61.
- 14 C. H. Yang, M. J. Yacaman and K. Heinemann, *J. Cryst. Growth*, **47** (1979) 283.

Appendix E

Microdiffraction from Gold Microcrystals[†]

J. M. Cowley* and Ronnen Roy**

*Department of Physics, Arizona State University

Tempe, Arizona 85281

**Materials Research Laboratory,

Pennsylvania State University,

University Park, Pennsylvania 16802

Running head: Gold Microcrystals

Person to contact regarding paper:

J. M. Cowley

Department of Physics

Arizona State University

Tempe, AZ 85281

Telephone: work (602) 965-6459

home (602) 966-0071

Key words:

Microdiffraction; STEM; Optical analyser system; gold; microcrystals;
multiple twinning; diffraction at twin planes; coherent diffraction
effects.

[†]Submitted to Scanning Electron Microscopy/1981.

Abstract

By use of an optical analyser system attached to a scanning transmission electron microscopy (STEM) instrument it is possible to obtain microdiffraction patterns from specimen regions 1nm or less in diameter. Patterns have been obtained from gold particles 2 to 5nm in diameter formed in thin near-amorphous supporting films by co-sputtering with polyester or alumina. The diffraction patterns show evidence of the multiple twinning on (111) planes which has previously been observed in larger gold particles formed by other methods. Diffraction patterns calculated for small regions of crystal including a twin plane show agreement with the observed patterns. A splitting of the diffraction spots which occurs frequently is the result of using a coherent convergent incident beam for diffraction from a finite crystal.

Introduction

The high brightness of the cold field emission gun used in dedicated STEM instruments allows relatively high beam currents to be concentrated in the small focussed probe incident on the specimen. On any detector plane following the specimen a convergent beam electron diffraction (CBED) pattern is formed of the specimen area irradiated by the incident beam. The number of electrons per second in the beam is sufficient to give a clear diffraction pattern with high signal-to-noise ratio for electron beam diameters of less than 1nm. Given an efficient and convenient means for viewing and recording these electron microdiffraction patterns an important new component is added to the armory of electron optical techniques used for attacking the problems of understanding the solid state of matter on a scale approaching that of interatomic distances. Direct photographic

recording of microdiffraction patterns is normally not feasible because the presence of photographic materials in the system degrades the excellent vacuum (better than 10^{-9} torr) normally attainable. Hence other forms of two-dimensional detector system have been investigated.

To our HB5 STEM instrument we have added an optical analyser system (Cowley, 1980) which, among other things, allows the microdiffraction patterns to be seen clearly and recorded in a small fraction of one second. If desired the TV images of these patterns may be recorded on video-tape and played back so that individual patterns may be recorded at the rate of 30 per second.

Recently the manufacturer (VG Microscopes Ltd.) has provided a system of two post-specimen lenses as an addition to our instrument. These allow the diffraction pattern to be expanded or contracted by any desired factor before entering the optical system. It is therefore possible to achieve the most favorable compromise between resolution in the diffraction pattern (normally limited by the fibre optic plates and the TV raster) and the pattern intensity.

For many purposes it is convenient to work with an electron beam of diameter 1-2nm. The intensity available is then adequate to allow relatively weak diffraction spots to be observed without difficulty. The size of the diffraction spots (inversely proportional to the beam diameter) is such that for the crystal unit cell dimensions commonly encountered (0.3-1nm) the individual spots are well separated and clearly defined. Also the complications due to the coherence of the incident beam, which comes from what is effectively a point source, are not as severe as in the case of very small beam diameters although, as we shall see, these complications are present to some extent.

Using beams of this size we have carried out a number of systematic investigations which demonstrate the value of the microdiffraction technique. Extended studies have been made of the structure and epitaxial relationship of thin, near-amorphous layers of oxide formed on chromium and chromium-iron alloys (Watari and Cowley, 1981). Also a detailed investigation has revealed interesting detail of the structures of small gold particles 1 to 5nm in diameter which are of interest in relation to the catalytic properties of finely dispersed metals.

In the present paper we use the results of this latter investigation to illustrate some of the practical considerations which arise when diffraction methods are extended to the study of such extremely small specimen volumes, often containing fewer than 1000 atoms.

Experimental

Thin films containing small gold particles were made by co-sputtering gold with either alumina or polyester (Roy and Cowley, 1981). Sputtering with alumina took place in an atmosphere of oxygen and argon (20 mTorr partial pressure of each) and the gold content of the films was varied by varying the relative areas of gold foil and the alumina film exposed to the discharge. The sputtered films were collected either on carbon supporting films. For the sputtering with polyester an atmosphere of argon was used and, in some cases, the films were formed on sodium chloride crystals which were then dissolved so that the films could be collected on copper microgrids. The films formed on carbon supports were estimated to have a thickness of 20-30nm. Those on the sodium chloride were probably around 5nm thick.

The films were examined by X-ray diffraction and using conventional

transmission electron microscopy (TEM) and selected area electron diffraction. These methods gave no clear evidence as to the state of crystallinity of the gold since the diffraction patterns showed only diffuse haloes.

In the HB5 STEM instrument with its attached optical system the gold particles were seen in bright field images to be 1 to 10nm in diameter. Dark field images suggested a crystal size of the same order of magnitude. The supporting films of alumina and polyester appeared to be amorphous.

Microdiffraction patterns were obtained with an objective aperture size of $10\mu\text{m}$ giving an incident beam convergence angle of 3×10^{-3} radians so that for 100kV electrons the beam size at the specimen was about 1.5nm. The diffraction pattern was formed on a fluorescent screen, amplified by an image intensifier, imaged in the optical system and viewed with a low-light-level TV camera. The diffraction patterns were recorded by photographing the TV display directly using exposure times of $\frac{1}{4}$ or $\frac{1}{8}$ sec. Alternatively the patterns were recorded on video-tape, played back one frame at a time and recorded on the analog memory of a Vistascan image converter and then read from this memory on to the photographic cathode ray tube incorporated in the HB5 console.

A direct correlation could be made between the microdiffraction pattern and the bright-field STEM image if the central spot in the diffraction pattern was placed over a small mirror in the optical system which reflected the light to a photomultiplier. When a raster scan was applied to the beam an image of the specimen was formed. The beam could be stopped at any point of the image, indicated by a marker, and the diffraction pattern from that point could be recorded.

If the same objective aperture was used for the image as for the

diffraction pattern, the image resolution could not be better than the beam diameter used for diffraction. Hence a sequence of operations commonly used was to obtain a high resolution (0.5nm) image of an area of the specimen (fig. 1) using a large objective aperture (60 μ m), then insert the 10 μ m aperture and record the same field of view. Then the beam was stopped on any chosen crystal to record its diffraction pattern. Alternatively the sequence could be reversed when the first step was to find a diffraction pattern from a crystal in a desired orientation or displaying interesting diffraction effects.

Observations

The microdiffraction patterns from gold particles showed a variety of effects illustrated in figures 2, 3 and 4. Figures 2 and 4 were obtained by photographing the TV screen directly. Figure 3 contains patterns recorded on video-tape and replayed.

In many cases the spot patterns could be attributed to single crystals of gold. With comparable frequency, the patterns showed spots from several crystallites in twinned orientations. Especially for the smaller particles (2-4nm diameter) there were often continuous streaks along some of the lines between diffraction spots (see figs. 2 (b-d) and 3(c)).

By using the variable d.c. offset controls on the beam scan it was possible to move the beam about on the specimen by well-defined amounts. In this way it was possible to investigate the variation of the diffraction pattern as the beam was moved over a gold particle. For large gold particles (5-10nm diameter) clear single crystal patterns could be obtained from several different areas of the particle. From between these areas two or more of these single crystal patterns appeared simultaneously, often

with the streaking between the spots, as the beam straddled the twin boundary. For the smaller particles, about half showed only one single crystal pattern. The rest showed evidence of the same twinning effects, with the twin boundaries occupying a correspondingly large proportion of the projected area of the particle.

The background of the gold spot diffraction patterns had a mottled appearance, which was especially strong for the alumina supporting films (figs. 2 (c) and (d)) and for the thicker polyester films with carbon film supports. This mottled appearance is characteristic of the scattering from amorphous materials and arises because, when the volume of sample illuminated by the incident beam contains only a few hundred atoms, the averaging over many atom configurations, which smears out the scattering into diffuse haloes in normal diffraction patterns, does not take place.

In many cases the gold diffraction spots showed a fine structure, being split into two or three components. For example, fig. 4 shows two patterns taken from opposite sides of the same small crystal (about 4nm in diameter). As the beam was moved across the crystal the spots first appeared as split, then became brighter and unsplit and then split again in different directions as the beam left the crystal. As will be discussed below, this effect has been shown to be due to an edge diffraction effect, common to all finite crystals and arising from interference in a coherent convergent incident beam. It is not related to the internal crystal structure and so may be omitted from our initial discussions.

Multiple twinning in small metal particles

It has been known for a number of years that small particles of face-centered cubic metals often have a multiply-twinned structure. Most of the

observations have referred to particles 5nm or more in diameter, prepared from colloidal solutions (Uyeda et al. 1973) or by evaporation on single crystal supports which induce a certain amount of well-defined preferred orientation through epitaxial growth (Ino and Ogawa, 1967; Allpress and Sanders, 1967; Yagi et al. 1975; Heinemann et al. 1979). These studies have made use of the techniques of high resolution TEM, dark-field TEM, selected zone dark field imaging, weak beam thickness fringe imaging, imaging of moire patterns and selected area electron diffraction.

The picture which emerges is that particles of two different sorts tend to form as a result of multiple twinning on the close-packed (111) planes. The (111) planes form the boundaries of tetrahedrally shaped crystallites. Five such tetrahedra may be joined together with a twin relationship between them to form a decahedral particle. If the angle between the tetrahedron faces were 72° , the five tetrahedra would fit in a pentagonal arrangement around a common edge (in a [110] direction) with no strain or gaps at the interfaces. Since, however, the angle between the tetrahedral faces is 70.5° it is necessary to postulate some means for accommodating this misfit so that the unlikely alternative of one or more thin wedge shaped gaps between the tetrahedra is avoided.

Similarly twenty tetrahedra can be fitted together with multiple twinning relationship to form icosahedral particles with only a small degree of misfit to be accounted for. The observations suggest that most of the multiply twinned particles are either decahedral or icosahedral in form, although some imperfectly formed particles of either type, with a few tetrahedra missing, have been observed on occasion.

It has been proposed (Heinemann et al 1979; Yacaman et al. 1979) that the metal lattice is uniformly distorted from the face-centered cubic form

to either body-centered orthorhombic or rhombohedral to accommodate the misfit between the tetrahedral crystallites. This proposal appears to account very well for the available observations by diffraction and imaging methods. On the other hand it has been observed that in some relatively large particles, dislocations are present which could alleviate the overall strain of the lattice by localizing the misfit distortion (Marks, et al 1979).

Several authors have made model calculations which suggest that for very small particles containing only a few hundred atoms the multiply twinned form may be more stable than the untwinned form. (Allpress and Sanders 1967; Fukano and Wayman, 1969; Ino, 1969). It is therefore of considerable interest to determine whether the multiply twinned form is present for crystals smaller than the 50 Å size which has been the lower size limit in most investigations. Also, since the influence of a crystal substrate used for epitaxial growth of the crystallites has usually been a major factor in both the experimental work and the theoretical analysis, it is of interest to study the particles formed by sputtering for which no influence of a substrate is relevant. A further question to be born in mind is the possibility that the faults or strain in the crystallites associated with the twinning may have some relevance for the catalytic activity of small metal particles.

The geometry of multiple twinning

The geometric relationship of crystallites twinned on (111) planes is reflected in the diffraction patterns as illustrated in figure 5. Figure 5(a) represents the spot pattern produced with an incident beam in the [022] direction. If there is twinning on a ($\bar{1}11$) plane, parallel to the

line drawn in fig. 5(b), the line of $n(\bar{1}11)$ spots will be common to both lattices and so will be every third row of spots parallel to this one. On the intermediate lines of spots there will be the characteristic appearance of pairs of spots separated by one third of the $\bar{1}11$ spot spacing. This configuration is clearly visible in figs. 2(a), 2(b) and 3(a). If there is a second twinning on another of the (111) -type planes the pattern will become more complicated, as in fig. 5(c) where the twinning is on the (111) plane of the original lattice, or in fig. 5(d) where there is twinning on the $(\bar{1}11)$ plane of the new lattice of fig. 5(b). Several features of these predicted spot configurations are visible in the patterns reproduced. There are now two intersecting sets of the lines of doubled spots, shown in fig. 5(b), forming characteristic large diamond shapes. These are visible in the patterns of figs. 2(c), 2(d), 3(a) and 3(b). There are characteristic close groups of three spots, one 200 -type and two 111 -type, which appear strongly in fig. 3(a).

Another clear indication of a doubly twinned configuration is the near alignment of a 111 -type spot and a 220 -type spot. This is indicated by the dotted line in fig. 5(c) and is clearly visible in the horizontal direction, particularly to the right of the central spot, in figs. 3(a) and 3(b).

Hence it may be concluded that for the particles giving figs. 2(c), 2(d) and 3(a-c) there are at least two twin planes within the area illuminated by the incident beam. This is consistent with either a decahedral or an icosahedral model for the particles.

Further evidence for the decahedral model is provided by the pentagonal outlines for some of the particles seen in the bright field STEM images such as figure 1.

Streaking in microdiffraction patterns.

It is generally true that planar discontinuities in crystals will give rise to continuous streaks in diffraction patterns, perpendicular to the plane of the discontinuity. The streaking observed in the microdiffraction patterns of gold may be attributed to this cause since the streaks are usually perpendicular to identifiable twin planes. However it is not immediately obvious that twin planes can be said to represent discontinuities in the lattice when we are considering diffraction from such a small region that the total number of planes of atoms parallel to the twin plane may be between 5 and 10.

All of our preconceived ideas on streaking in diffraction patterns due to twinning come from theory and experiment referring to very large numbers of twin planes distributed at random or according to some probability law through a large volume of crystal (see, for example, Cowley 1981). For such cases the streaking occurs on the double-spot lines of fig. 5(b) but not on the line of spots through the origin or every third line parallel to this. The streak intensity is high around the positions of the sharp spots and falls off rapidly away from them. The streak is strong in between the sharp spots only if there is a very high probability for twinning i.e. if twinning occurs, on the average, at distances of only a few planar spacings.

The streaking observed in the microdiffraction patterns of gold is not consistent with this picture. While the streaks lie along the double-spot lines, as expected, their intensity distributions are irregular, with maxima which are not always at the sharp-spot positions and which do not show symmetry in form or intensity about the twin planes.

These irregularities of the streaking may be attributed to the fact

that only a small number of planes of atoms contribute to the diffraction pattern and that the twin plane may not be at the center of the beam so that more planes are illuminated on one side of it than of the other.

In order to confirm that the observations are consistent with this picture we have calculated the intensity distributions along the lines of the streaks to be expected for a few representative cases.

We take as our model the arrangement of atoms about a (111) twin plane, viewed along the [110] direction, illustrated in the insert of figure 6. The atom positions may be represented by the function

$$\left[\sum_{s=0}^n \delta \left(\underline{r} + s \left(\frac{a}{3} + \underline{c} \right) \right) + \sum_{t=0}^m \delta \left(\underline{r} + t \left(\frac{a}{3} - \underline{c} \right) \right) \right] * \sum_p \delta (\underline{r} - p\underline{a})$$

where the horizontal and vertical periodicities have been assumed to be a and c and we have taken n planes of atoms on one side and m planes on the other side of the twin plane.

Fourier transforming this to give the diffraction amplitude leads to

$$\Psi(uv) = \left[\sum_{s=0}^n \exp\{2\pi i s(ua/3 + vc)\} + \sum_{t=0}^m \exp\{2\pi i t(ua/3 - vc)\} - 1 \right] \times \sum_h \delta(u - h/a)$$

where u, v are the reciprocal space coordinates. The diffraction intensity along the continuous streaks is then found by calculating $|\Psi(v)|^2$ for $u = h = 3N \pm 1$ for integral N . We have done this for cases with $n = m$ and with $n \neq m$. To take account of the fact that the incident beam is not sharply defined we have done some averaging of the results. This eliminates some of the more violent oscillations of the curves.

In figure 6 we have plotted the average of the $n = 2, m = 4$ and the

$n = 3$, $m = 5$ cases (full line) and also the average of the $n = m = 2$ and $n = m = 3$ cases (dashed line). These results illustrate the general behaviour of the intensity distributions which follow what might be expected intuitively.

For the symmetrical cases the curve is symmetrical about the mid position. When the number of planes is so small that the distinction between the f.c.c. and the hexagonal close packing is not well defined (and it takes three planes to define the f.c.c. sequence) there is an additional maximum at the $v = \frac{1}{2}$ position. This disappears for $n > 3$.

For the unsymmetrical case, the intensity maximum at one of the sharp spot positions ($v = \frac{1}{3}$ or $\frac{2}{3}$) is narrower and higher than for the other. For the case considered neither peak is very sharp and both have odd bumps on them.

These results are consistent with the observations. In patterns such as figs. 2(b) and 3(c) it is seen that the intensity maxima along the streaks differ in sharpness and width and are not accurately located at the sharp spot positions of fig. 5(b). The widths of the maxima are comparable with those of the calculated curves, suggesting that the numbers of planes involved are approximately equal to those assumed. The peak at $v = \frac{1}{2}$ has been observed in several cases.

Splitting of diffraction spots

As illustrated in figure 4, diffraction spots from small single crystal regions may be split into two or three relatively sharp components. This effect was first noticed in the diffraction patterns of the small gold crystallites but has been observed also for small crystals of MgO smoke and for a number of other specimens. It has been shown to occur when a

coherent incident convergent beam is close to the edge of a crystal. All spots in the diffraction pattern are split in the same way. The separation of the split components is approximately equal to the diameter of the incident beam spot in the absence of a specimen. The incident beam spot may show the same splitting as the other diffraction spots.

An analysis of this effect, to be reported elsewhere, shows that it results from the phase factors which enter into the diffraction amplitudes as a result of the relative displacements in real space of the center of the electron beam and the center or edge of the diffracting crystal.

The relevance of this effect for our present considerations is that it complicates, to some extent, the interpretation of the diffraction patterns from the gold microcrystals. The details of the intensity distribution, on the scale of this splitting, cannot be interpreted without complete calculations taking all these interference effects into account. However, since the main evidence regarding the multiply twinned structure of the gold particles relies on observations of intensity variations on a larger scale than this, the conclusions we have reached in the above sections remain unaffected.

Conclusions

The evidence from the microdiffraction patterns suggests that the multiply twinned structure found for larger particles persists for particles of diameter as small as 2-3nm. Approximately half of the particles in this size range appear to have this structure, the remainder being near-perfect single crystals.

The diffraction patterns are consistent with the picture of an incident beam of diameter about 1.5nm illuminating portions of these particles

and so including at times, especially for larger particles, only perfect crystal regions but at other times covering one or two twin boundaries and portions of two or three twin-related crystallites so that the patterns show superimposed spot patterns with streaking between the spots and perpendicular to the twin planes.

There is fine structure due to the sensitivity of the intensities to the relative positions of the beam and the scattering centers when a coherent convergent incident beam is used. This complicates the interpretation of the diffraction effects to some extent. In particular it makes it difficult to give immediate answers to the question of the validity of the model which proposes that the crystal lattice within the crystallites is uniformly distorted from the f.c.c. structure.

The geometry of the diffraction patterns to be expected from this model has been worked out in detail by Yang et al. (1979). They showed for example that the (111)-type and (220)-type spots, which are shown to be almost colinear in figure 5(c) based on a twinning of undistorted f.c.c. tetrahedra, are exactly colinear when the distortion is taken into account. In patterns such as figs. 3(a) and (b) these spots appear to deviate slightly from the straight-line arrangement but this deviation lies within the range of uncertainty due to the inherent spot size and the unknown effects on these spots of interference from adjacent crystal boundaries or twin boundaries.

In order to resolve such questions it may well be necessary to improve the accuracy of the observations and to include more parameters into both the specification of the experimental conditions and the theoretical analysis. One possibility which appears experimentally feasible is to vary the degree of coherence of the incident beam in a controlled way so that

References

- Allpress, J. G. and Sanders, J. V. "The structure and orientation of crystals in deposits of metals on mica" *Surface Science* 7 (1967) 1-25.
- Cowley, J. M. "Optical processing of diffraction information in STEM" *Scanning Electron Microscopy 1980; I*: 61-71.
- Cowley, J. M. "Diffraction Physics" 2nd Edit. North Holland Publ. Co., Amsterdam, The Netherlands (1981) Chapter 18.
- Fukano, Y. and Wayman, C. M. "Shapes of nuclei of evaporated fcc metals" *J. Appl. Phys.* 40 (1969) 1656-1664.
- Heinemann, K., Yacaman, M. J., Yang, C. Y. and Poppa, H. "The structure of small vapor-deposited particles. I Experimental study of single crystals and particles with pentagonal profile" *J. Crystal Growth* 47 (1979) 177-186.
- Ino, S. "Stability of multiply-twinned particles" *J. Phys. Soc. Japan* 27 (1969) 941-953.
- Ino, S. and Ogawa, S. "Multiply twinned particles at earlier stages of gold film formation on alkali halide crystals" *J. Phys. Soc. Japan* 22 (1967) 1365-1374.
- Marks, L. D., Howie, A. and Smith, D. J. "The internal and surface structure of multiply twinned particles" in *Electron Microscopy and Analysis 1979*, T. Mulvey (ed.), The Institute of Physics, Bristol, England (1980) 397-400.
- Roy, Ronnen and Cowley, J. M. "The structure of gold particles in co-sputtered films" *Thin Solid Films*. In press.
- Uyeda, N., Nishino, M. and Suito, E. "Nuclear interaction and fine structure of colloidal gold particles" *J. Colloid Interface Science* 43 (1973) 264-276.
- Watari, F. and Cowley, J. M. "The study of oxide formation on (001), (011), (111) and (113) surfaces of Cr thin films using STEM-microdiffraction methods" *Surface Science*. In press.
- Yacaman, M. J., Heinemann, K., Yang, C. Y. and Poppa, H. "The structure of small, vapor-deposited particles. II Experimental study of particles with hexagonal profile" *J. Crystal Growth* 47 (1979) 187-195.
- Yagi, K., Takayanagi, K., Kobayashi, K. and Honjo, G. "In-situ observations of growth processes of multiply twinned particles" *J. Crystal Growth* 28 (1975) 117-124.
- Yang, C. Y., Yacaman, M. J. and Heinemann, K. "Crystallography of decahedral and icosahedral particles, II High symmetry orientations" *J. Crystal Growth* 47 (1979) 283-290.

the importance of the position sensitive interference effects may be evaluated. An alternative, which would require more extensive data collection and theoretical analysis but would give a more complete analysis, would be to record diffraction patterns on video tape as the incident beam is scanned slowly in a two-dimensional raster over a small particle.

A further factor complicating the interpretation of the microdiffraction patterns is the scattering from the amorphous supporting film which can obviously be strong for films 10-20nm thick and appreciable even for very thin films, especially when it is considered that in a coherent diffraction situation it is the complex amplitude variations due to the amorphous support which are added to the amplitudes of diffraction from the particle being investigated.

It is clear that the possibility of obtaining microdiffraction patterns from nanometer-size areas on a routine basis can be very valuable for the study of very small crystals or crystal defects. It is also clear that there are complications to the interpretation of the data which, while potentially adding to the amount of information to be obtained, will require a considerable amount of study both theoretically and experimentally before they can be fully exploited.

Acknowledgement: This work was supported by the National Science Foundation, Grant DMR-79126460 and made use of the resources of the Facility for High Resolution Electron Microscopy supported by Grant CHE-7916098 under the NSF Regional Instrumentation Facilities Program. This work was also supported in part by the U.S. Army Research Office under Contract No. DAAG29-80-0089.

Gold Microcrystals

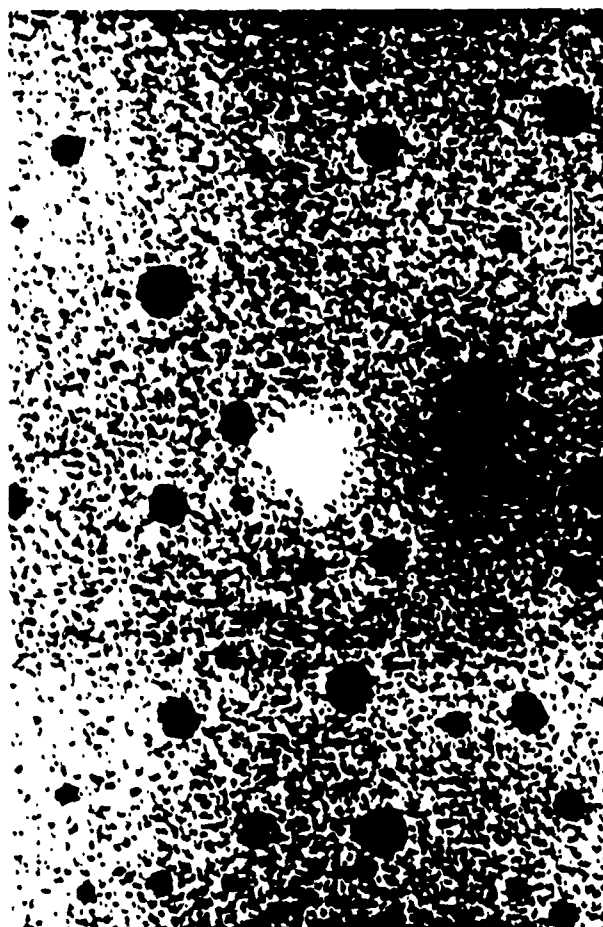


Fig. 1. Bright field STEM image of small gold particles in a thin film formed by cosputtering with polyester. The white spot is the overexposed marker used to indicate the point at which the beam is stopped to obtain a microdiffraction pattern. Magnification marker = 10nm.

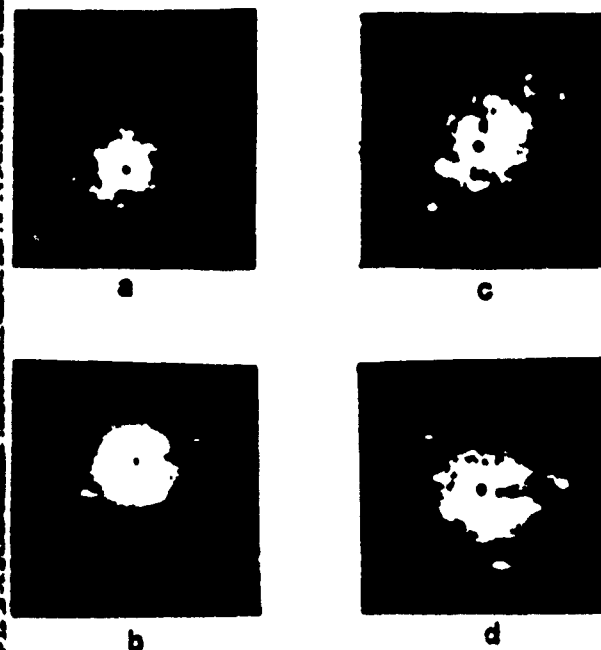


Fig. 2. Microdiffraction patterns of small gold particles of diameter 2 to 5nm such as those in fig. 1. Patterns (a) and (b) were obtained with a thin polyester supporting film and for (c) and (d) the film was thicker and composed of amorphous alumina.

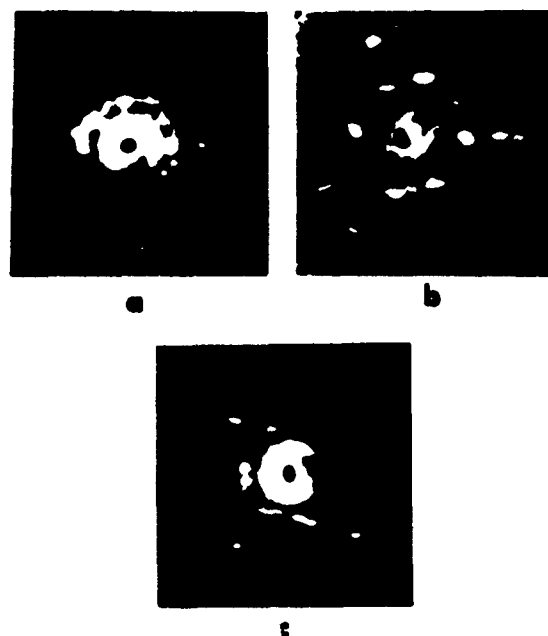


Fig. 3. Microdiffraction patterns from small gold crystallites, recorded on video-tape and played back one frame at a time.

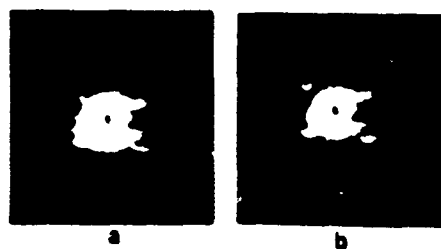


Fig. 4. Microdiffraction patterns obtained from the two opposite edges of a small gold crystallite (about 4nm in diameter) showing the splitting of the diffraction spots.

Gold Microcrystals

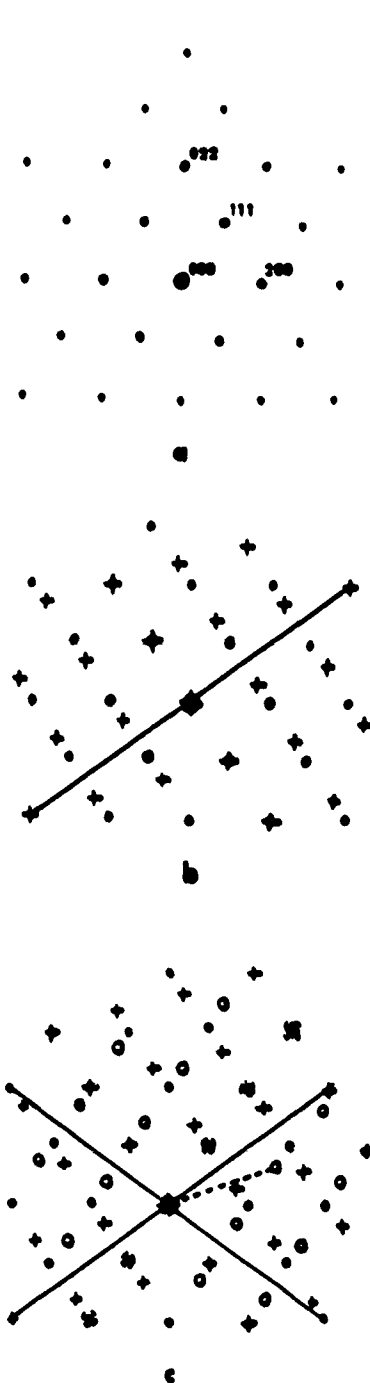


Fig. 5. The geometry of diffraction patterns formed from crystals of an f.c.c. metal, (a) for an untwinned crystal; (b) for crystals twinned on the (111) plane indicated by the line; (c) for crystals doubly twinned on planes indicated by the two lines; (d) for twinning on the two planes indicated, one referring to the pattern indicated by dots and the other referring to the pattern of crosses.

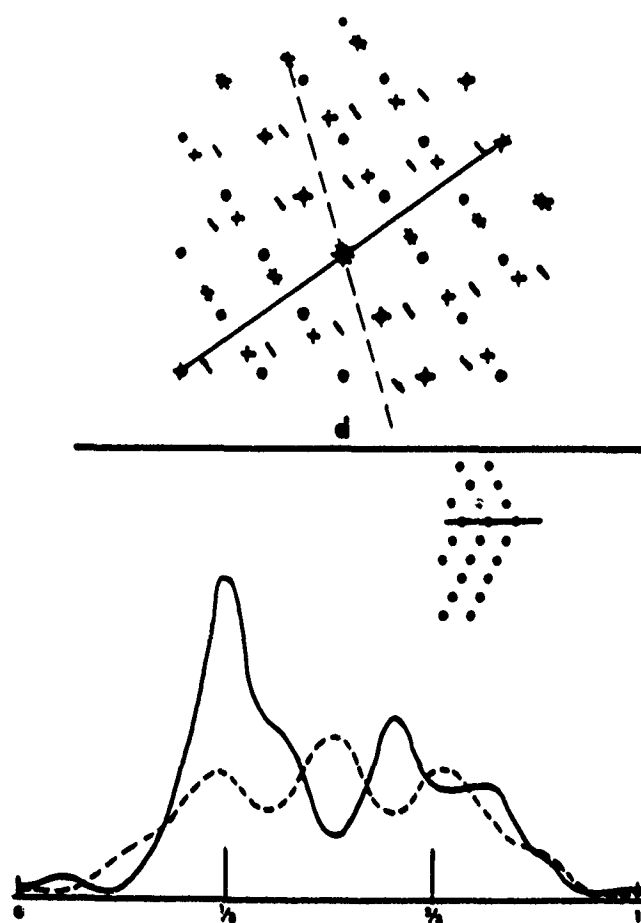


Fig. 6. Calculated intensity distribution along the double-spot lines of fig. 5(b) for a crystal region with n planes of atoms on one side of a twin plane and m planes of atoms on the other side. The full curve is the average for the cases $n = 2, m = 4$ and $n = 3, m = 5$. The dashed curve is the average for the cases $n = m = 2$ and $n = m = 3$.

Rapid Solidification by rf-sputtering in the Mg-Zn-O System

R. A. Roy, R. Messier, S. V. Krishnaswamy, and Rustum Roy

Materials Research Laboratory
The Pennsylvania State University
University Park, PA 16802

Abstract

Non-crystalline solid (NCS) films in the Mg-Zn-O system have been prepared over a wide composition range by sputtering. For pure Mg-Zn alloys this range is expanded and shifted away from the narrow eutectic range found in alloys quenched from the liquid. In the ternary Mg-Zn-O region the NCS formation range expands further as oxygen is incorporated in the films. The NCS formation behavior is dependent on unique aspects of vapor-to-solid preparation. Thermodynamic, kinetic and structural parameters are compared with liquid-quenched preparation techniques.

I. Introduction

The physical vapor deposition method of sputtering has been used to make non-crystalline solid (NCS) films from a variety of single- and multi-component systems¹. One advantage to forming NCS materials by sputtering is the fast temperature quench rate as sputtered material deposits at the film surface from the vapor. Moreover, in multi-component systems, the compositional range over which NCS's are obtained is greater for vapor-deposited materials than for those solidified from the liquid state. This results in large part because the various elements are brought together only at the growing film surface where the rapid quench rate prevents phase separation.

Materials in the Mg-Zn system have been prepared from the melt by rapid quenching techniques. Both Boswell² and Calka et al.³ found that NCS thin

layers could be obtained over the Mg_xZn_{1-x} composition range $0.68 < x < 0.75$ which is centered at the deep eutectic composition $x = 0.72$. In this report we have prepared Mg-Zn sputtered films over a wide composition range and compared their NCS formation behavior with these previous studies. In addition, we have examined the NCS formation in Mg-Zn-O ternary composition films in which oxygen is incorporated during sputtering of the binary alloy components.

II. Experimental

Mg-Zn-O films were prepared in an rf-diode sputtering unit (Materials Research Corporation) using a 12.5cm diameter metallic target consisting of a Mg disc of the same size upon which a 2mm thick, 2.5cm wide sector of Zn was bonded. Substrates were arranged underneath the target such that they lay in a line perpendicular to the Mg-Zn interface in the target (see Figure 1). In this manner, the composition is expected to vary continuously between each substrate. The sputtering chamber was evacuated to about $4-5 \times 10^{-7}$ Torr before each test and the film substrates were placed upon a liquid nitrogen cooled substrate holder directly beneath the target for most of the experiments. Tests ranged up to 6 hours and the films obtained were generally between 3 and $8\mu m$ thick. To form oxygen containing films, O_2 gas was leaked in at pressures ranging from 10^{-6} to 10^{-4} Torr for different tests, while the pressure of the predominant sputtering gas (Ar) was maintained at $\sim 5 \times 10^{-3}$ Torr. The films were deposited on 8 x 8mm glass slides as well as carbon discs and aluminum pans (for direct use in differential scanning calorimetry experiments).

III. Results and Discussion

Initial tests were performed without the liquid nitrogen cooled substrate holder with x-ray diffraction done on several series of films deposited at

different power levels (see Figure 2). At 100W rf-power crystalline Zn and Mg phases are observed, as well as several intermetallic compounds. At 50W similar crystalline peaks occur (see Figure 2a), although pure Mg appears only weakly crystalline. Films formed at 25W show some crystalline Zn and no other crystalline phases (Figure 2b). These results show that the formation of NCS films is enhanced at lower rf-power levels which is apparently related to the correspondingly lower substrate temperatures during film growth.

When the substrates were cooled using liquid nitrogen ($T_{\text{sub}} \leq -75^{\circ}\text{C}$), films were deposited onto carbon and glass substrates. Electron microprobe analysis was done for each set of films using the carbon discs, and x-ray analysis was performed for the corresponding glass substrate films. The results for Mg-Zn and Mg-Zn-O films are shown in Figure 3. The crystalline and non-crystalline phases formed are shown as a function of overall composition represented by the ternary diagram. It is noted that the NCS range for the pure metal system encompasses about 30 at.% as compared to about 7 at.% for splat-quenching methods and is shifted away from the NCS range observed in splat quenched Mg-Zn materials, centered at the deep eutectic at $x = .28$, and toward more Zn-rich compositions. The area of NCS formation expands rapidly from the pure metallic zone as small amounts of oxygen (~ 5 at.%) are incorporated in the films. This is consistent with the fact that gaseous impurities such as oxygen generally reduce the mobility of atoms at a growing film surface and thus stabilize the films from re-crystallization⁴. Similarly, Boswell² implied that minimization of oxygen in splat quenched samples using an inert atmosphere leads to a reduction in the NCS formation tendency.

Also of interest is the fact that the films that are stoichiometric oxides are apparently crystalline over the compositions that were measured. Although

many multi-component oxide systems do form NCS films easily, the present results are not unexpected. It is known that MgO can not be made non-crystalline as readily as ZnO by sputtering¹ and that ZnO, with a crystallization temperature of 75-100°C, must be prepared below room-temperature in order to obtain NCS films⁵. Further, the equilibrium binary phase diagram for MgO-ZnO shows that ZnO is soluble in the MgO structure up to nearly 60% ZnO which is greater than the most zinc-rich composition measured in the pure oxide films in the present study. The films containing about 40 at.% oxygen are shown to be non-crystalline at the zinc-rich compositions and it is likely that this occurs for the stoichiometric oxide system near the ZnO composition.

The above results illustrate that kinetic and thermodynamic barriers to NCS formation in liquid-to-solid techniques are often overcome by vapor-to-solid preparations such as sputtering. In previous studies^{2,3} of Mg-Zn glass formation, investigators took advantage of the low temperature at the deep eutectic at 72 at % Mg (see Figure 4). The formation of NCS alloys here rests largely on the ability to cool the liquid of near-eutectic compositions to below some critical temperature before crystalline rearrangement takes place. However, by sputtering, we have produced oxygen-free NCS alloys at compositions far removed from the eutectic region (65-35 at % Mg), suggesting that such films are more stable than those formed around the deep eutectic, where mixed crystalline and non-crystalline phases were obtained. This difference in NCS formation behavior between vapor-quenched and liquid quenched solids obviously results from the different quench routes to the final room-temperature solids and apparently reflects the much higher quench rate and solid solubility of vapor-solid transformations on the one hand and the final-state temperature of the solid during preparation (room-temperature for

liquid quenched alloys^{2,3} and possible elevated temperatures for sputter vapor-deposition¹) on the other hand. For instance, Calka et al.³ have shown that near-eutectic compositions are only marginally stable at room temperature. The relative importance of kinetic and structural factors on NCS formation is an important question which remains.

Calka et al.³ have pointed out that the atomic size difference of the elemental components and their large number of compounds formed indicate a high tendency toward NCS formation. Also, another important point is that phase separation and the resultant formation of polycrystalline films can be greatly reduced by the introduction of small amounts of oxygen. Because the film growth is essentially an atom-by-atom process, small amounts of "impurity" atoms can reduce the mobility of metallic atoms at the growing film surface, thus preventing both segregation and crystallization. These factors are all reflected in the wide NCS composition range obtained with the addition of 5-8 at % oxygen to the Mg-Zn alloys. More importantly, the incorporation of several percent oxygen should stabilize the as-formed NCS film to subsequent re-crystallization by lowering the mobility of the Mg and Zn atoms within the bulk of the film. Thus, the addition of oxygen is expected to enhance both the ability to form NCS films and the temperature stability of such films. A detailed study of the recrystallization of these Mg-Zn and Mg-Zn-O NCS films will be reported separately.

Acknowledgement: This work was supported by the U.S. Army Research Office under Contracts Nos. DAAG29-78-0033 and DAAG29-80-0089.

References

1. R. Messier, "New Experimental Approach to Understanding the Formation of Non-Crystalline Solids", Ph.D. Thesis, The Pennsylvania State University, University Microfilms, Ann Arbor, MI 48106, (1973).
2. P. G. Boswell, "Crystallization of an $\text{Mg}_{74}\text{Zn}_{26}$ Glass", Mater. Sci. Eng. 34, 1-5 (1978).
3. A. Calka, M. Madhava, D. E. Polk, B. C. Giessen, H. Matyja, and J. Vander Sande, "A Transition-Metal-Free Amorphous alloy: $\text{Mg}_{.70}\text{Zn}_{.30}$ ", Scripta Met. 11, 65-70 (1977).
4. H. L. Caswell, "Effect of Residual Gases on Superconducting Characteristics of Tin Films", J. Appl. Phys. 32, 105-114 (1961).
5. R. A. Mickelsen and W. D. Kingery, "Preparation and Properties of Non-crystalline Zinc Oxide Films", J. Appl. Phys. 37, 3541-3544 (1966).

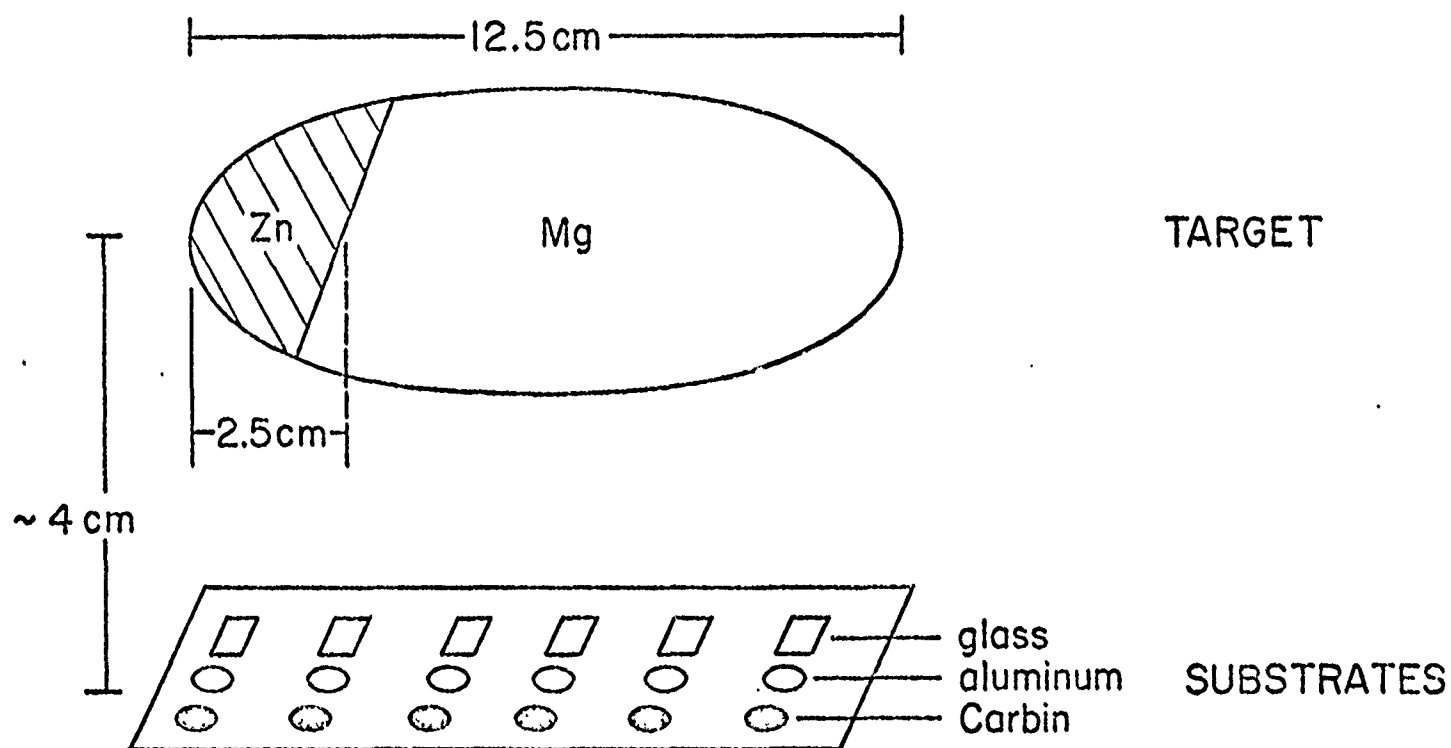


Figure 1: Geometrical relationship of target and film substrates used in Mg-Zn-O sputtering.

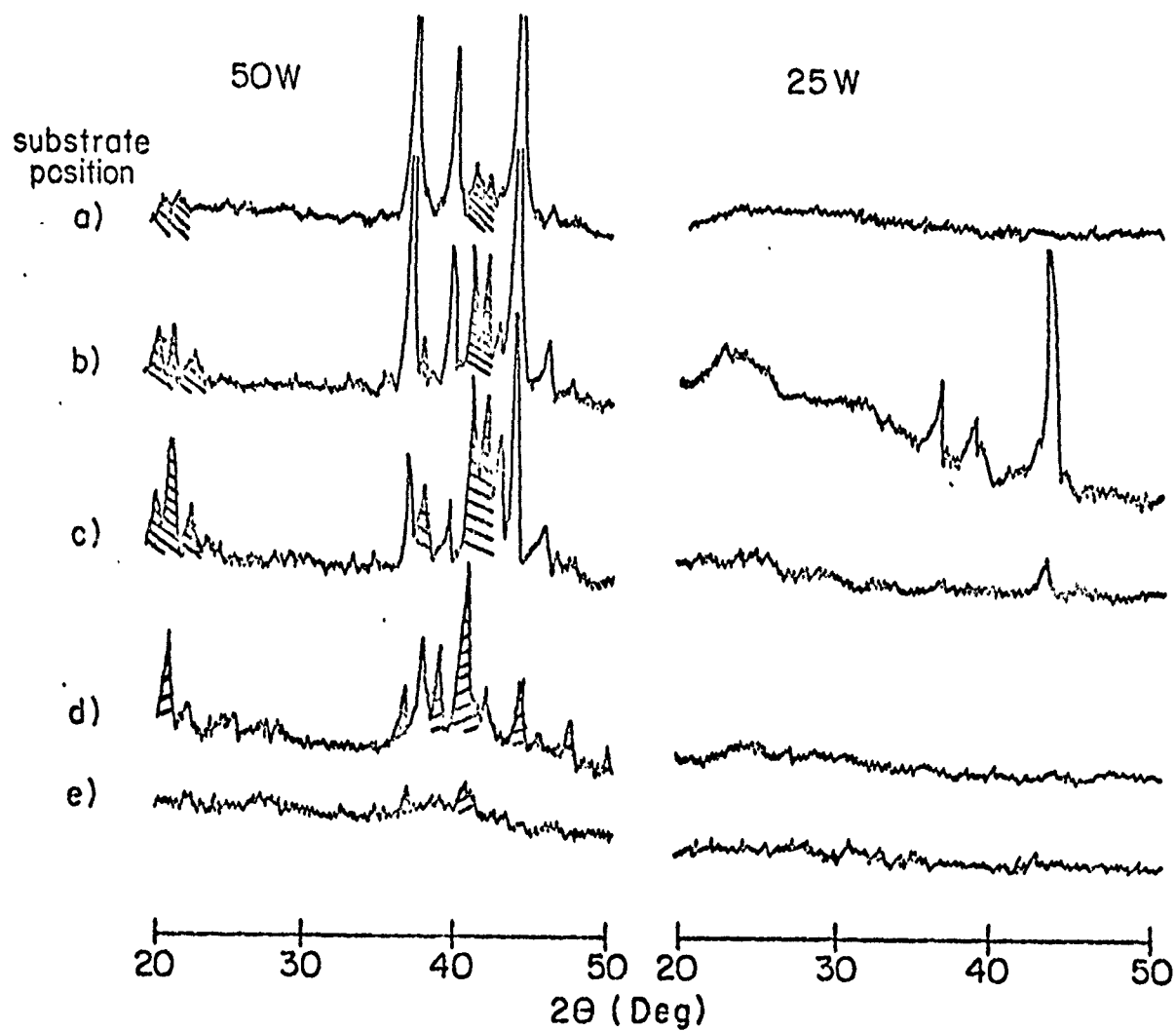


Figure 2. Formation of crystalline phases in films deposited at 50 and 25W respectively, without liquid nitrogen substrate cooling. Zn \square , MgZn_2 $////$, MgZn $\\$, as well as Mg \boxtimes form at different compositions for the 50W test; only a weak Zn peak is present in two films in the 25W test.

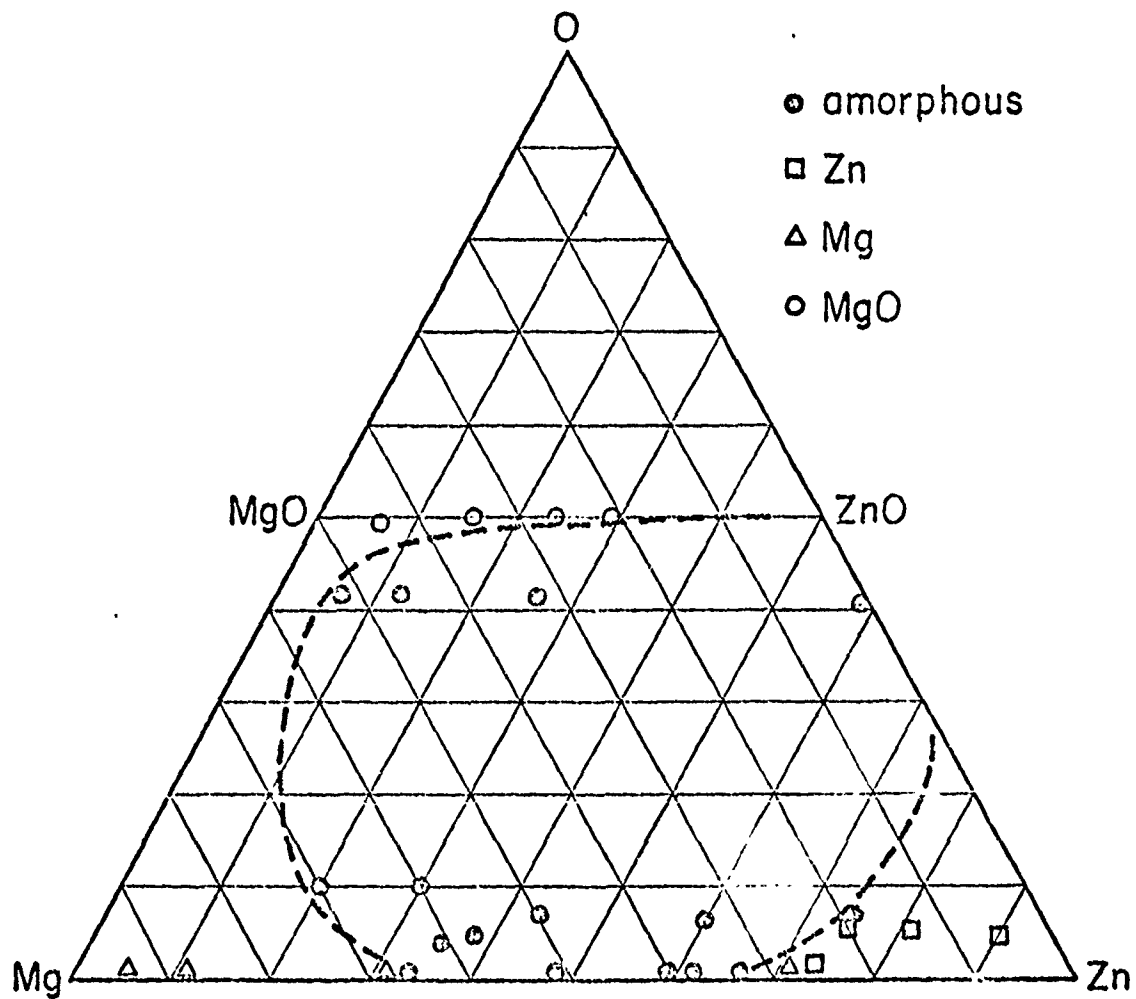


Figure 3. Formation of crystalline and non-crystalline phases as a function of overall composition for Mg-Zn-O films deposited on liquid nitrogen cooled substrates.

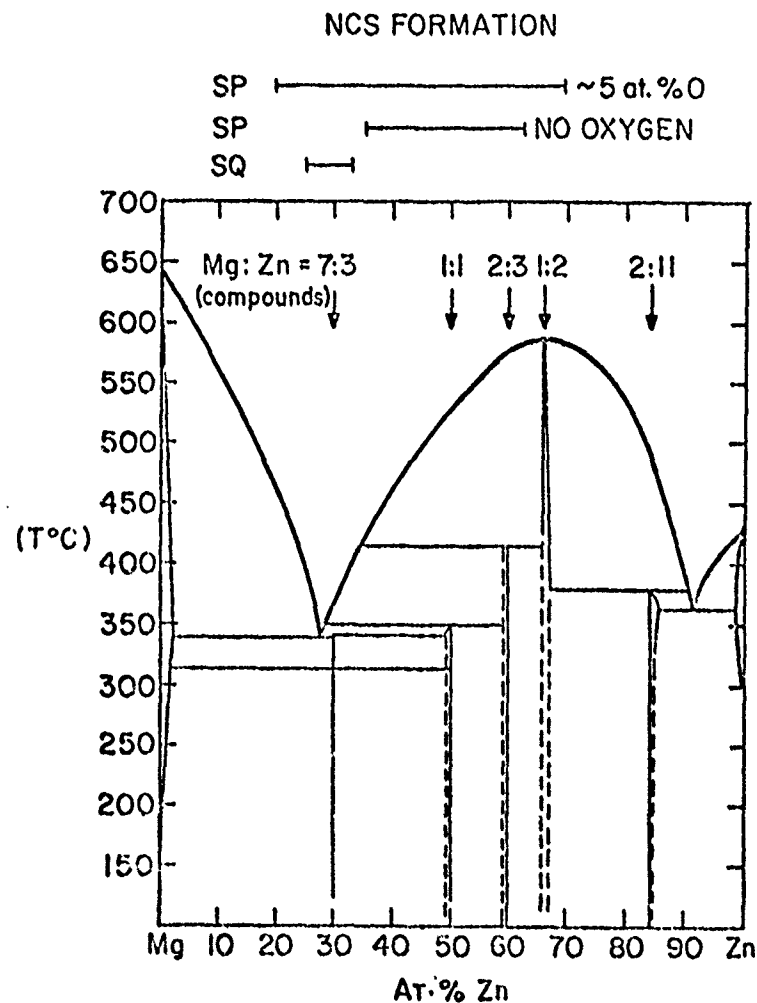


Figure 4. Mg-Zn equilibrium phase diagram showing NCS formation regions obtained by splat quenching (SQ) and sputtering onto cooled substrates (SP). The effect of incorporation of several percent oxygen is shown by indicating the range in terms of Mg/Zn ratio in those Mg-Zn-O films.

Appendix G

POLYMER AND POLYMER-METAL FILMS BY rf-SPUTTERING

INTRODUCTION

In recent years research into the preparation and characterization of polymer thin films has increased. Several relatively new techniques for polymer preparation have been employed in research as well as industrial production. These methods include:

- 1) solution deposition (1)
- 2) plasma polymerization (2-5)
- 3) vacuum evaporation (6-8)
- 4) sputter deposition (9-15)

all of which are suited to producing films several micrometers thick or less. Additionally, these processes have been modified to produce films containing both polymer and metal components^(16,17). Such films are of interest from several standpoints:

- 1) A polymer-metal composite film combining desirable mechanical and electrical properties is a possibility.
- 2) Polymer-metal films could be used as precursors for materials such as:
 - a) a microporous polymer film formed by selective etching of the metal component
 - b) a metal/metal-oxide sintered film formed by burning the polymer component⁽¹⁸⁾
- 3) Conduction mechanisms in polymers might be better understood by studying the behavior of composites⁽¹⁹⁾.

In the present study we have set out to produce polymer and polymer-metal films by rf-sputtering. We have attempted to prepare films using several representative polymers as sources, and have selected, from these, suitable polymers to co-sputter with metals. As a result of these studies, the applicability of rf-

diode sputtering for preparing polymer films has been more clearly defined.

EXPERIMENTAL

Three different rf-sputtering units were used in preparing films. The first was an MRC model SES-8632 (referred to as "MRC" system). In this system a central shaft ran through the deposition chamber and 62.5cm circular substrate holders/shutters could be attached to the shaft. The shaft could be rotated so that different substrates could be placed sequentially under the target without opening the chamber to air. The second system consisted of a Plasma-Therm model HFS-500C rf-generator, MRC rf-diode sputtering module, and a CVC diffusion pump (referred to as MRC/CVC system). This unit featured a liquid-cooled substrate stage which could be raised or lowered under the target using an external control knob, thus allowing the target-substrate separation to be varied. A third system used was a Perkin-Elmer Randex model 3140 unit evacuated by a Welch turbomolecular pump.

RESULTS AND DISCUSSION

A. Bulk Polymer Sputtering

1. Results

Since the only polymer films made by sputtering to date involved fluoropolymers, PTFE was first investigated. Because sputtering is a non-equilibrium preparation method, and thus film characteristics and properties are highly dependent on sputtering conditions, such tests are not redundant with previous literature⁽⁹⁻¹⁵⁾. In addition, polyethylene (PE), polypropylene (PP), polyvinylchloride (PVC), polyvinylidene fluoride (PVDF), and an aromatic polyester (EKONOL*) were also sputtered. The rationale behind

the selection of this group involved selection of polymers having relatively simple structures but displaying widely varying elemental composition and physical properties. In this manner, the experimental thin film formation might be related to the polymer type of the bulk precursor.

a. PTFE: PTFE targets 50mm diameter and 10mm thick mounted on Al backing plates were made from a bulk extracted rod. Initial work using the MRC system involved experimental variation of Ar gas pressure, rf-power, and substrate-target separation from test to test. Though PTFE can be sputtered in its own self-generated vapor, Holland et al.⁽¹⁴⁾ have shown that film deposition rates are higher when PTFE is sputtered in pure Ar. Films deposited on glass slides appeared faintly yellow in color and have non-crystalline x-ray diffraction patterns. The film thickness was measured using Tolansky-type interferometer (Varian λ -scope). The film deposition rate was calculated from each test and found to increase with power in the regime measured and to increase with decreasing target-substrate separation. The Randex sputtering unit was then used to prepare additional films to check instrumental variation of film deposition behavior. This time additional glass substrates were placed upon the target ground shield where it was observed that a film had been accumulating. Deposition rates as a function of power, pressure and separation are shown in Figures 1-4.

In several tests film was collected on KBr discs and analyzed in a Fourier Transform infrared system. The spectra (a typical one shown in Figure 5) were nearly identical in all cases and displayed a small broad peak between 1600 and 1750cm^{-1} in addition to the large absorption due to CF stretching mode at 1220cm^{-1} . The smaller absorption was apparently due to oxidation of the polymer film. An elemental profile analysis of a sputtered

PTFE film on Cu substrates was performed using Ion-Scattering Spectrometry (ISS). Film profiles obtained in the top 40-60nm showed no oxygen present. The apparent discrepancy between IR and ISS data might be due to slight variations in the sputtering environment during the different tests. Alternatively, the IR films might have incurred post-deposition oxidation from several hours exposure to ambient conditions before IR analysis. The ISS films were only exposed to ambient conditions for several minutes. Nevertheless, the tests showed good reproducibility of films in all other respects.

b. PVDF: A 51mm dia. x 3mm thick PVDF target was made from sheet stock of the high purity polymer. During most PVDF tests the target-substrate separation was 2.5cm. Both MRC and CVC/MRC units were used to sputter PVDF. During initial tests films of 30-50nm were obtained after one to two hours, indicating deposition rates around $5\text{\AA}/\text{minute}$. When tests were performed for longer periods very little film was found to accumulate on substrates below the target. To determine whether film re-sputtering from the substrate was occurring, glass slides were also placed upon the target ground shield. The pressure was varied from 25 to 125 to 300mTorr Ar between tests at a constant power of 25 watts. Film thickness was measured using a Talysurf 10 stylus profilometer. At 25mTorr the deposition rate was about $1\text{\AA}/\text{minute}$ on the ground shield and $1/2\text{\AA}/\text{minute}$ on the substrates under the target. At 125 and 300mTorr the rate was about $1/2\text{\AA}/\text{minute}$ for both ground shield substrates and normal substrates. Though tests were repeated twice with similar results, the extremely low film accumulation rate in PVDF tests makes it hard to make conclusive remarks. One explanation is that film re-sputtering may

occur in all cases studied with the effect decreasing at higher pressures. This pressure dependence is consistent with previous re-sputtering studies⁽²⁰⁾. Moreover, the structure and composition of sputtered films could not be determined for lack of sample.

The most serious hindrance to normal rf-sputtering of PVDF may be due to the dielectric properties of the polymer. By an unfortunate coincidence, a large peak in the dielectric loss occurs with its center at 10^7 Hz and a value of $\tan \delta$ is about 0.25 which is directly proportional to the energy absorbed by the polymer at that frequency. Because the frequency of the rf-signal during sputtering was 13.56 MHz, the PVDF target absorbed the field energy causing a large dielectric heating effect. Indeed, dielectric heating of PVDF has been used to determine its pyroelectric coefficient⁽²¹⁾. Even in tests performed at 40W power the PVDF targets (mp $\sim 180^\circ\text{C}$) softened and dislodged from the Al backing plates after about 1 hour. This suggests that practical rf-sputtering of PVDF is at least limited to frequencies well below 1 MHz.

c. PE, PP, PVC: Polyethylene, polypropylene, and polyvinylchloride sputtering targets 51mm diameter and 3mm thick were sputtered in the CVC/MRC unit at power levels between 25 and 50W. Although a stable plasma was maintained during all initial depositions, target degradation was noticeable after several hours after plasma initiation for each polymer. Using PVC, the target apparently melted after one hour sputtering. This was not surprising because the softening point of PVC is about 75°C and this temperature could easily be reached at the target surface. Initial tests involving PE and PP targets produced clear films about 200 to 500nm thick. The films obtained were not

sufficient to do extensive characterization, and after several short depositions, the targets detached from the Al backing plates. No evidence of material accumulation on the ground shield or elsewhere in the sputtering chamber was present. The deposition of thin films underneath the PE and PP targets shows that some transfer of target material to the substrate occurred, but the manner in which the films formed cannot be understood without longer depositions during which mechanical integrity of the targets is maintained.

d. EKONOL: The final polymer selected was Ekonol, an aromatic polyester based on p-hydroxybenzoic acid. It is highly crystalline and stable to 600-700°C. The above results clearly demonstrated the need for thermal stability during polymer sputtering and it was reasoned that Ekonol, like PTFE (decomposition ~350°C) had a clear advantage in this respect. The target was made from a 8cm diameter 6mm thick disc of the polymer. Initial sputtering tests produced mechanically stable films depositing at about 10Å/minute, except when the Ar pressure was maintained at 5mTorr in which case the films peeled from the substrate. Peeling at low gas pressures is commonly found for both metal⁽²²⁾ and semiconducting⁽²³⁾ films and has been related directly to a high compressive stress and indirectly to the minimization of void network structures in the films.

A series of further tests was done to correlate Ar pressure, rf power, and target-substrate separation to film deposition rate in order to maximize the rate. In addition, KBr pressed pellets and metallic substrates were used for IR spectroscopy and dielectric property measurements, respectively. Figures 6, 7 and 8 plot deposition rate as a function of sputtering parameters, and show maxima in rate vs. pressure and power. Figure 9 compares

the bulk Ekonol IR spectrum with the spectrum obtained from the sputtered film (Fig. 10). Immediately apparent is the loss of the many sharp absorption peaks, characteristic of the bulk polymer, when the material is sputtered. The sputtered films showed a characteristic broad absorption centered about 1600cm^{-1} . The thin film spectra suggest an entirely amorphous and possibly degraded polymer is formed. Moreover, x-ray diffraction of sputtered Ekonol invariably showed no crystallinity. However, the resistivity of the sputtered films remained high ($\sim 10^{10}\Omega\text{-cm}$) suggesting that the films were not largely degraded chemically. It is likely that if the polymer became carbonized the resistivity of the films would approach values for a-C ($\sim 10^2\Omega\text{-cm}$). Moreover, semi-quantitative hydrogen profiling in the films was done by Secondary Ion Mass Spectrometry (SIMS) and the level was found to be comparable, if somewhat lower than the bulk polymer. Mass spectra (a typical one shown in Figure 11) show the presence of hydrogen, carbon, and many low molecular weight hydrocarbon species but no oxygen. Thus, the sputtered films appear to be amorphous, hydrocarbon derivatives of the bulk polyester, having comparable resistivity to the bulk ($\sim 10^{12}\Omega\text{-cm}$).

2. Discussion - Polymer Sputtering Problems

a. Thermal Stability: The difficulty in obtaining sputtered films using PE, PP, PVC, and PVDF clearly shows that low thermal stability can be a factor limiting the applicability of rf-sputtering to a wide range of polymers. Two physical properties, melting temperature (T_m) and dielectric loss ($\tan \delta$) are critical variables and a combination of low T_m and high $\tan \delta$ in the rf frequency range leads to target softening and plasma instability during sputtering. In the case of PVDF, the maximum dielectric heating occurs at the frequency commonly used (13.56 MHz). In contrast to PVDF ($T_m = 160^\circ\text{C}$ and $\tan \delta = 0.25$), PTFE has a high "melting point" ($\approx 350^\circ\text{C}$) and

low loss ($\sim 10^{-4}$ at 10MHz). Thus PTFE, a fluoropolymer not greatly dissimilar in elemental composition to PVDF, can be sputtered under a wide range of sputtering conditions giving films with excellent dielectric properties similar to the bulk polymer. Similarly, Ekonol ($T_m \approx 600^\circ\text{C}$, $\tan \delta \approx 10^{-3}$ at 1MHz) can be sputtered easily to give reproducible films, although some chemical decomposition occurs.

b. Chemical degradation: The apparent loss of oxygen in Ekonol sputtering is an example of some chemical degradation which can be expected to apply to many polymers subjected to an rf-plasma. Yasuda⁽²⁴⁾ has studied the behavior of different chemical structure types in an rf-plasma. He found that monomers containing aromatic groups, C=C, -N-, -Si-, remain stable and easily polymerize in the plasma, while monomers containing -C=O, -O-, -OH, and Cl tend to decompose in the plasma. For the case of polymer sputtering, it is reasonable to assume that sputtered polymer fragments will behave similar to monomers having the same chemical groups. Thus, the C-O-O group in bulk Ekonol apparently should be unstable in the plasma leading to decomposition of fragments containing it. Upon decomposition, oxygen may be released resulting in oxygen-free fragments which deposit in the growing film. Thus, the SIMS data shows no significant oxygen level in the sputtered films. In general, the functional groups present in the bulk polymer may determine which can be sputtered without large degradation problems in a similar fashion as the monomer structure does in the plasma polymerization studies by Yasuda.

c. Deposition Behavior:

The mechanism of film formation in PE and PP (hydrocarbon polymers) by sputtering is not clear because of lack of sample material and data. It is possible that film formation results from plasma polymerization of

low molecular weight fragments or monomers evolved from the targets during sputtering. Tibbet et al.⁽¹²⁾ have proposed this two-step process of film formation for PTFE sputtering. In addition, surface heating of the targets may cause evaporation of polymer and subsequent film formation.

In PVDF and PTFE (fluorocarbon polymers) sputtered films accumulation on the target ground shield was, in general, comparable to that beneath the target. Several processes may be involved in film formation. First, the deposition of polymer fragments on surfaces beneath the target should in the simplest case follow a cosine law distribution with the largest accumulation under the target center (Fig. 12a). In general, the rate should go up with increasing power and decrease at high pressures due to increased gas phase scattering of polymer material.

Second, formation of some polymer from re-polymerization of fluorocarbon gas evolved from the polymer target is generally thought to occur in PTFE sputtering (Fig. 12b). The distribution of plasma polymerized film formed in this manner is not well characterized since this effect has not been isolated from pure sputter deposition.

Third, the effect of film re-sputtering may have several origins (Fig. 12c). If a negative bias develops at the substrate, this may be sufficient to cause Ar^+ bombardment of the substrate and consequent re-sputtering of the film. Alternatively, if negatively charged particles develop at the target, they will be accelerated away from the target and often arrive at the substrate with sufficient energy to cause re-sputtering⁽²⁰⁾.

The fact that Figure 3 shows a maximum in PTFE film deposition rate vs. Ar pressure for both 25W and 50W suggests that more than one process is

present. The initial increase in deposition rate at the substrate with pressure may be attributed to increased efficiency of target sputtering by Ar^+ . The decrease at higher pressures may be caused by the increased number of gas phase collisions of polymer fragments with Ar. At 10mTorr the mean free path is about 7mm while the distance the sputtered species must travel to the substrate is 40mm. Thus, at pressures above 50mTorr, where the mean free path is less than 2mm, the fragments are essentially diffusing through the plasma at thermal velocities. This increases the likelihood of polymer decomposition to low molecular wt. species. This, in turn, may facilitate increased plasma polymerization by increasing the concentration of active species. If the film formed on the target ground shield is attributed to plasma polymerized fluorocarbons, it can be seen that the deposition increases and levels off with a slight decrease at higher pressures. While the amount of polymer arriving at the substrate is sharply reduced, the deposition rate at the ground shield remains high. Presumably at higher pressures more polymer fragments are decomposed by sustaining more collisions and are re-polymerized in proximity to the ground shield. Finally, it should be noted that the data indicate that film re-sputtering does not seem to play a major role. In general, the re-sputtering effect should be larger at close target-substrate separations. However, Figure 4 shows that ratio of film formed at the ground shield to the substrate decreases as the separation decreases, just the opposite of behavior expected for film re-sputtering. However, a re-sputtering process cannot be excluded and in composite polymer-metal sputtering there is strong evidence for this phenomenon, which will be discussed later.

In summary, for both PTFE and EKONOL, conditions favoring sputter-deposition of film are relatively low gas pressure (10-30mTorr Ar) and moderate power (50W) with a small separation (2-3cm). In the case of PTFE, the fluorine deficiency commonly found in sputtered films^(13,14) decreases when the substrate is positively biased, presumably from attraction of F^- and F^* radicals in the plasma⁽¹³⁾. Lehman et al.⁽²⁵⁾ showed that the film deposition rate and fluorine content in sputtered PTFE films increased with addition of 20-40% CF_4 to the Ar atmosphere. This they attributed to film bombardment by F^0 radicals and plasma polymerization of CF_4 gas. Thus, while the sputtering of PTFE presents several complications, knowledge of the plasma processes allows one to manipulate the operator controlled parameters to obtain the best films.

B. Polymer-Metal Sputtering

The polymer-metal co-sputtering experiments were designed to make films containing an intimate mixture of the two phases over a range of metal concentrations. Of particular interest was the ability to vary the metal concentration, and thereby the microstructure and film properties, by choice of sputtering conditions. PTFE and EKONOL were used as polymer components in these tests.

1. Results

a. PTFE-metal co-sputtering

1.) PTFE-Pt - All PTFE-metal sputtering was done using the MRC system. The first experiments used a regular 5cm diameter PTFE target upon which foil containing 90% Pt/10% Rh alloy was placed. In the initial series of tests a sector of Pt-alloy foil was placed on one side of the PTFE target with the area of the sector varied between tests. In tests

with a large metal area (1/4 total area) the films appeared metallic and x-ray analysis showed crystalline platinum. In addition, the PTFE target area was coated with a brownish grey appearance. In tests with a metal area ~10% total target area, the deposited films appeared to be PTFE while the Pt-alloy target area was coated with a non-conducting film. Subsequent tests were performed with a metal target area of intermediate size with the geometry indicated in Figure 13. A series of 8 x 8mm glass slides were placed in a row perpendicular to the polymer/metal boarder in the target. In this manner it was expected that the films would vary in metal content from substrate to substrate. Because of the apparent re-sputtering effect which caused the target discoloration in the previous tests, subsequent tests were performed for only 10 minutes to establish whether the target damage occurred within that period of time. Series of films examined in a SEM showed smooth and structureless surfaces on the 100nm level although the films appeared visually like neither PTFE or metal.

Compositional profiles of two of these films deposited in the same test were performed using a 3M Ion Scattering Spectrometer. The films (positions #4 & #5 in Figure 13) were about 40nm thick and were profiled at a sputtering rate of 1nm/hr for the first thirty minutes. Data were collected in scans run at intervals of 5 to 6 minutes during this time. After thirty minutes the ion beam was focused to a smaller diameter giving a sputtering rate of 10nm/hr while scans were done at intervals ranging from 5 to 10 minutes for 2 1/2 hours. Thus, the data were obtained for the top few monolayers of film as well as providing compositional analysis through 20-30nm of the film. Figures 14 and 15 show the atomic % of several elements vs. sputtering time which is directly proportional to film depth. The oxygen signal initially present could indicate either a discontinuous film with

some beam penetration to the substrate or some interdiffusion of substrate atoms through the film. At any rate, the onset of rapid increase in the signal corresponds to the central beam penetration to the substrate. A chlorine signal was present in both films probably a result of contamination from the epoxy used to bond the PTFE target to the backing plate. When the scan of Cl + F concentrations is plotted along with C concentration, Figures 16 and 17 show the Cl + F signal as a function of time is roughly parallel to the C concentration, suggesting that the Cl may be substituting for F in the polymer phase. Of more fundamental interest, however, is the variation of metal concentration in the film which shows that at the film surface the metal concentration is rapidly approaching zero for both films, while at depths equivalent to greater than 20 min ion sputtering ($\sim 4\text{nm}$) the Pt/C ratio is roughly constant. Thus, during film formation almost no metal is being incorporated in the film after the first 10 min of deposition.

When tests were repeated under the same sputtering conditions a stable plasma was not achieved and the PTFE target experienced extensive surface damage. At lower power levels (20-25W) a stable plasma was obtained and films were deposited on Cu microgrids with carbon supports for TEM analysis. However, bright-field and SAD modes gave no indication of any metal in the films. The apparent re-sputtering effect and associated plasma instabilities and lack of reproducibility for the PTFE/Pt-alloy tests led to the substitution of Au for Pt-alloy in subsequent tests.

2.) PTFE-Au - A PTFE/Au target was made by placing a small $\sim 1\text{cm}^2$ area of Au foil on the edge of a 5cm diameter PTFE target (Figure 18). Initial tests using power levels of 25-50W produced films whose appearance varied as a function of substrate proximity to the gold portion of the

target, ranging from gold and reflective to reddish-brown and non-reflective. For one test, films deposited on 4 KBr substrates arranged for decreasing gold content were analyzed using a Perkin-Elmer IR spectrometer. Figure 19 shows that all four samples exhibited a broad absorption around 1200cm^{-1} characteristic of the PTFE C-F vibration. However, as in the previous case, repeated tests caused plasma instabilities and PTFE target damage, while the target ground shield was coated with gold.

3.) PTFE-Cu - A final series of PTFE-metal co-sputtering tests was done using Cu metal and various target configurations. Different sized PTFE circular discs were placed on a 2" diameter Cu target initially. In some cases the PTFE was bonded to the Cu surface using a conductive medium. The power was 50W for most tests, while the Ar pressure varied from 25 to 400mTorr. In the tests performed at higher pressures (100-400mTorr) the deposition rate on the substrates was about 0.1-0.2nm/min while a small amount of film deposited on the ground shield. A series of tests performed at 25mTorr Ar and 50W power with variation of PTFE target size produced the following results. During three tests performed using a 30mm PTFE disc and no connective medium to the Cu target, it was observed that the PTFE surface turned brown-gray after several minutes of sputtering. However, after about 15 minutes the target began to turn white again. The tests were conducted for 20, 30 and 120 minutes. The film deposited for 20 minutes appeared light blue; the 30 minute film appeared yellow-blue; the 120 minute film was faintly yellow. Films deposited on NaCl substrates positioned under the target and on the target ground shield were measured in a Perkin-Elmer IR spectrometer and were found to contain fluorocarbon polymer in all 3 cases. During tests performed with a conductive medium between copper and polymer target components, but otherwise identical

conditions to those above, a dark metallic coating was formed over the PTFE target surface after tests of 15-30 min. In addition, the deposited films beneath the target were Cu colored and conductive, while IR spectra of the film on NaCl substrates indicated no distinct fluorocarbon absorption peak. Finally, tests were performed at 25mTorr Ar and 50W with no conductive medium but with PTFE circular discs of smaller size ranging from 13mm diameter to 27 mm diameter. The films collected on the target and ground shield in all these cases were conductive and apparently devoid of significant amounts of polymer. A summary of all the PTFE-metal co-sputtering tests is presented in Table 1.

b. EKONOL-metal co-sputtering

A Pt-alloy and Au were used to co-sputter with EKONOL. However, after initial qualitative examination of Au and Pt-alloy co-sputtered films, it was decided to focus experiments on the Au-polymer system exclusively.

Using a target geometry similar to PTFE-Au tests, films were deposited in the MRC and Randex sputtering units. At 75W power in the MRC system mechanically stable films were obtained when the Ar pressure was 15mTorr or greater. Though a thin film was found to form on the target ground shield, the deposition rate beneath the target was 10 to 20 times greater. Cross plane film resistivity measurements were made for films deposited on metal substrates. Figure 20 shows the target and substrate arrangement and Figure 21 shows the dc-resistivity vs. substrate position for tests run at different power levels. The ac-resistivity of the same films was measured using a Hewlett-Packard 4274A LCR meter. In general Figure 22 and 23 shows that the $\log \rho$ varies linearly with \log frequency suggesting a hopping type conduction in the films. The resistivity vs. temperature data shown in Figures 24 and 25 for the same samples shows that the conductivity follows fairly well a $1/T$ vs. $\log \sigma$ behavior common to hopping semiconductor type films. For the 70W test the volume % Au was

estimated from film density measurements at each substrate position. Figure 25 show that even a ~45% Au ($R = 0$) the dc-resistivity was some 10^{10} times greater than for pure gold.

Because the film thickness was highly non-uniform under the target at power levels above 60W a subsequent test was done at 40W and films deposited on a series of eight carbon support Cu microgrids were analyzed in a Phillips EM 300 electron microscope. The bright field images shown in Figure 27 of the polyester-gold films clearly show that the gold particles are discrete even in gold-rich films. Figure 28 compares the microstructure and diffraction patterns for two different substrates. The dark field image shows that most particles are 2-8 nm in size at $R = 0$, while at $R = 18$ mm region the majority of particles are 2-3 nm or less. At substrates # 4 thru #8 diffraction patterns became diffuse and dark field images failed to show any distinct gold particles. Substrate #4 and #5 were examined using a HB5 scanning transmission electron-microscope⁽²⁶⁾. Figure 29 shows the B.F. and D.F. images indicating particle sizes of 1 to 3nm for both #4 and #5.

When sputtering was done in the Perkin-Elmer system, the power was increased to 200W and pressure was 25mTorr Ar. Resistivity, compositional, and microstructure data are shown in the next series of figures. Resistivity was measured on films deposited on metal and glass substrates shown in Figure 20. The dc- resistivity vs. substrate position shown in Figure 30 gives the same relative variation for metal and glass substrates, although the resistivity is about 100 times lower for glass substrate films. (The different values may be due to the fact that the resistivity for metal substrate films was measured cross plane whereas, the glass substrate films were measured along the film plane.

The volume % Au in the films was estimated using energy dispersive X-ray analysis. Shown in Figure 31 is the cross plane d.c. resistivity

vs. % Au in the films. The a.c.-resistivity (Figure 32) and dc-resistivity vs. temperature (Figure 33) again show behavior characteristic of hopping conductivity. TEM micrographs of films sputtered onto NaCl substrates, shown in Figure 34, reveal that the particles in the gold rich films (~25-30% Au) range from 2-8nm in size while the majority of particles in the gold-deficient films are 2nm or smaller. Again, there appears to be no clustering of gold islands even in the gold-rich films.

2. Discussion

a. PTFE-metal co-sputtering: The ISS data from PTFE/Pt-alloy sputtering and IR spectra of PTFE/Au films shows that thin polymer-metal films can be made. However, steady state conditions in the plasma were not maintained and a re-sputtering phenomenon seems to play a dominant role in these tests. This was first indicated by visual observation of the PTFE/Pt-alloy target after sputtering and by the ISS profiles which show that after 10 minutes of sputtering virtually no metal is arriving at the film surface. Thus, the Pt-alloy target appears to be completely coated with polymer by this time.

One possible explanation for this behavior is that negative ion induced re-sputtering is occurring. Several authors have reported negative ion re-sputtering effects in systems where the target contains elements whose electronegativity difference is large. Gilbert et al.⁽¹⁶⁾ have shown that negative oxygen ion re-sputtering occurs in the Ba(Pb,Bi)O₃ system. This is attributed to extraction of electrons from Ba by oxygen near the target surface. The O⁻ ions are accelerated from the target with sufficient energy to cause substrate film to be re-sputtered. Similarly, Cuomo et al.⁽²⁷⁾ have shown that in noble metal rare earth alloys, re-sputtering from negative

ion formation occurs when the difference between the ionization potential of the rare earth element and the electron affinity of the noble metal is below a critical value. In the PTFE/metal experiments, the fluorine has a high electron affinity and can attract electrons from metals with relatively low first ionization potentials. Thus, while film re-sputtering is not significant in pure PTFE sputtering, it occurs in PTFE-metal co-sputtering in the presence of electron donor metal atoms.

The PTFE-Cu experiments demonstrate that the re-sputtering effect causes extreme variation in the composition of the film produced which is directly dependent on the relative areas of polymer and metal target and on the thermal contact between the two targets. The experimental results can be explained in the following manner. During the first several minutes both polymer and metal deposit on the substrate. The evolution of some fluorine from the target precipitates F^- formation in the presence of Cu. The F^- ions are accelerated across the dark space toward the substrate at cathode potential and will re-sputter the growing film if not thermalized by gas phase collisions. The components in the film will be resputtered and some material will deposit on the target and target ground shield. If the relative amount of polymer is large, the re-sputtered material will coat the Cu portion of the target, preventing further metal deposition after several minutes. The PTFE target that was observed to be darkened after a few minutes by re-sputtered Cu invariably turned white again as the source of Cu was covered by the re-sputtered polymer. In addition, the films deposited for 120 minutes appeared to be almost pure polymer, while the films deposited for 20 minutes still had significant copper in them.

When the polymer area is decreased the tests show that a metallic coating is re-sputtered onto the PTFE target area after several minutes. PTFE ceases to deposit on the substrate and F^- ions in the plasma are eliminated.

The copper then deposits alone in the film. In addition, the re-sputtered ground shield film is non-conductive, which is expected if re-sputtering occurs only in the first few minutes. While both PTFE and Cu are re-sputtered by F^- induced film bombardment, a non-conductive mixture of the two would form on the target ground shield. Subsequently F^- ions are depleted and the Cu depositing in the substrate film is not re-sputtered leaving the ground shield film non-conductive.

The behavior of the target when the PTFE is thermally bonded to the Cu may be explained by considering that the deposition of polymer film occurs not only from sputtering but by evaporation on the hot surface. Lehman et al.⁽²⁵⁾ have reported that in reactive sputtering of PTFE the deposition of polymer is indeed significantly greater when the target is uncooled. In the case where the target is not bonded to the cooled Cu target, the PTFE surface becomes hot enough to promote polymer evaporation as well as sputtering. The combination provides enough polymer to coat the entire Cu portion of the target when the substrate film is re-sputtered. But the sputter deposition rate of the cooled target alone does not provide enough polymer to re-sputter onto the Cu target. In this case the Cu arrives at the substrate faster and coats the polymer target after being re-sputtered.

In summary, the observations made during PTFE-metal co-sputtering can be explained by considering that negative ion induced re-sputtering is caused by the presence of fluorine and metal in the plasma. The subsequent film re-sputtering prevents continuous co-deposition of polymer and metal because of target geometry. Though Gilbert et al.⁽²⁰⁾ found that negative ions could be thermalized at pressures above 400mTorr preventing re-sputtering from occurring, during PTFE-Cu sputtering the deposition rate at 300mTorr was less than 0.1nm/min. One possible way of controlling the re-sputtering effect is by use of a two target system which would decrease any re-sputtered material arriving at the

target surfaces and decrease the concentration of negative ions formed by removing the metal target from the plasma in which the PTFE is sputtered.

b. EKONOL-Metal Co-Sputtering

The polyester-gold sputtered films produced had compositions ranging from about 40 to 1 vol % Au. In this range all films show relatively high resistivity which is expected if the gold phase is discontinuous. Thus, for all the films conduction appears to take place by an activated process. This is reflected in the data for resistivity vs. frequency and temperature. In each test the films show a decrease in resistivity with increasing temperature. When $\log \rho$ is plotted against $1/T$ the slope of the line increases as the gold content decreases, indicating an increased activation energy. This corresponds to a decrease in the Au island size and an increase in the average separation of the islands. The ac-resistivity data generally suggests hopping-type conduction. The resistivity varies as ω^n where ω is the frequency and n ranges from 0 to 1 for the samples studied. In some samples there appear two regions of frequency dependence with the transition region between 10^3 and 10^4 Hz. Such behavior has been reported for pure polymers⁽²⁸⁾ and polymer-metal composites⁽²⁹⁾.

CONCLUSIONS

The limitations of rf-sputtering for making polymer and polymer-metal films may be divided into 3 categories. The first is the physical properties such as low melting point and high dielectric loss found in such common polymers as PVDF, PP, and PE. The second is the chemical nature of the polymer. Certain chemical groups appear to be especially unstable in the rf-plasma as reported by Yasuda⁽²⁰⁾ and this problem will be reflected in degradation of the sputtered polymer. Thirdly, though fluoropolymers such as PTFE may be sputtered and still return their useful properties as thin films, a very pronounced re-sputtering effect occurs in PTFE-metal co-sputtering. Preliminary analysis suggests that this is caused by negative ion formation, and this limitation is not as funda-

mental as the first two. Because of the success in preparing polyester-gold sputtered films, it seems likely that fluoropolymer-metal films can be made using a modified rf-sputtering system.

REFERENCES

1. K. L. Chopra, T. V. Rao, and A. C. Rastogi, Appl. Phys. Letters. 29
340 (1976).
2. N. Morosoff, H. Yasuda, E. S. Brandt, and C. N. Reilley, J. Vac. Sci.
Tech. 15, 1815 (1978).
3. K. Nakajima, A. T. Bell, and M. Shen, J. Appl. Polymer Sci. 23, 2627
(1979).
4. G. Turban and Y. Catherine, Thin Solid Films 48, 57 (1978).
5. S. Padhkee, Thin Solid Films 48, 319 (1978).
6. Y. Murakami and T. Shintani, Thin Solid Films 9, 301 (1972).
7. P. Luff and M. White, Thin Solid Films, 6, 175 (1970).
8. M. Syzuki, Y. Tanaka, and S. Ito, Jpn. J. Appl. Phys. 10, 817 (1971).
9. R. Harrop and P. J. Harrop, Thin Solid Films 3, 109 (1969).
10. I. M. Pratt and T. C. Lausman, Thin Solid Films 10, 151 (1972).
11. D. T. Morrison and T. Robertson, Thin Solid Films 15, 87 (1973).
12. J. M. Tibbet, M. Shen, and A. T. Bell, Thin Solid Films, 29, 143
(1975).
13. H. Biederman, S. M. Ojha, and L. Holland, Thin Solid Films, 41,
329 (1977).
14. L. Holland, H. Biederman, and S. M. Ojha, Thin Solid Films 35,
L19, (1976).
15. L. Holland, J. Vac. Sci. Tech. 14, 5 (1977).
16. A. Rastogi and K. L. Chopra, Thin Solid Films 18, 187 (1973).
17. E. Kay, A. Dilks, and U. Hetzler, J. Macromolecular Sci. Chem. A12,
1393 (1978).
18. N. Boonthanom and M. White, Thin Solid Films 24, 295 (1974).

19. T. V. Rao and K. L. Chopra, Physica Stratus Solidi (a) 53, 43 (1979).
20. L. R. Gilbert, R. Messier, and S. V. Krishnaswamy, J. Vac. Sci. Tech. 17, 389 (1980).
21. H. Sussner, P. E. Horne, and D. Y. Yoon, Appl. Phys. Lett. 32, 137 (1978).
22. J. A. Thornton, J. Tabock, and D. W. Hoffman, Thin Solid Films 64, 41 (1979).
23. R. C. Ross and R. Messier, J. Appl. Phys. (in press).
24. H. Yasuda, J. Macromolecular Sci. Chem. A10, 383 (1976).
25. H. W. Lehmann, S. Frick, and R. Widmer, Thin Solid Films 48, 231 (1978).
26. R. A. Roy, R. Messier, and J. M. Cowley, Thin Solid Films, 79, 207 (1981).
27. J. J. Cuomo, R. J. Gambino, J.M.E. Harper, J. D. Kuptsis, IBM J. Research and Development 20, 580 (1977).
28. A. C. Rastogi and K. L. Chopra, Thin Solid Films 26, 61 (1975).
29. S. K. Bhattacharge, S. Busy, and S.K. De, J. Appl. Poly. Sci. 25, 111 (1980).

Table I

SPUTTING CONDITIONS				CHARACTERIZATION	RESULTS
Target	Area	RF Power	Ar Pressure		
PTFE/Pt alloy	10ZPt	50W	15mTorr	Visual examination, x-ray diffraction Visual examination, x-ray diffraction Scanning electron microscopy, x-ray diffraction ion scattering spectrometry	-Film appears to be pure polymer -Film appears to be pure metal PTFE target damaged -Films contain Pt and polymer -Pt concentration gradient with film depth
	20ZPt	45W	15mTorr		
	30ZPt	45W	15mTorr		
PTFE/Au	5ZAu	25W	25mTorr	Visual examination infrared absorbtion resistance measurement	-Films contain gold and polymer -Gold concentration decreases as a function of substrate distance from gold target
PTFE/Cu	30ZPTFE banded to Cu target	50W	25mTorr	resistance measurement infrared absorbtion visual examination	-Non-conducting films are deposited whose color changes from blue to yellow as the length of the sputtering test increases -Cu colored conductive film on substrates -PTFE target is black -Non-conductive ground shield film
		20 min			
		30 min			
		120 min			
	30ZPTFE banded to Cu target		30 min		
	26ZPTFE (unbonded)		15 min		

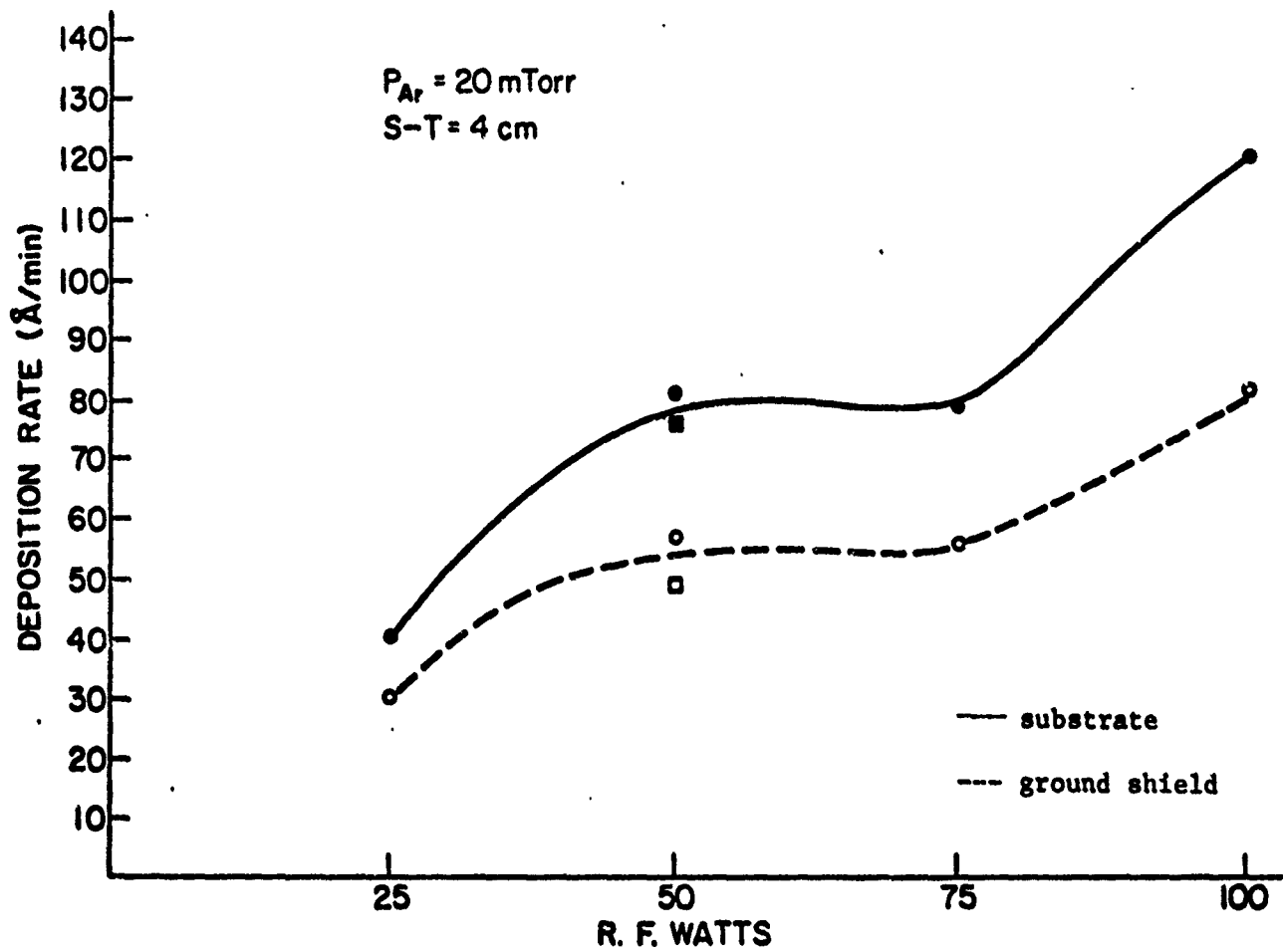


Fig. 1 Fluoropolymer film deposition rate vs power using an MRC sputtering unit.

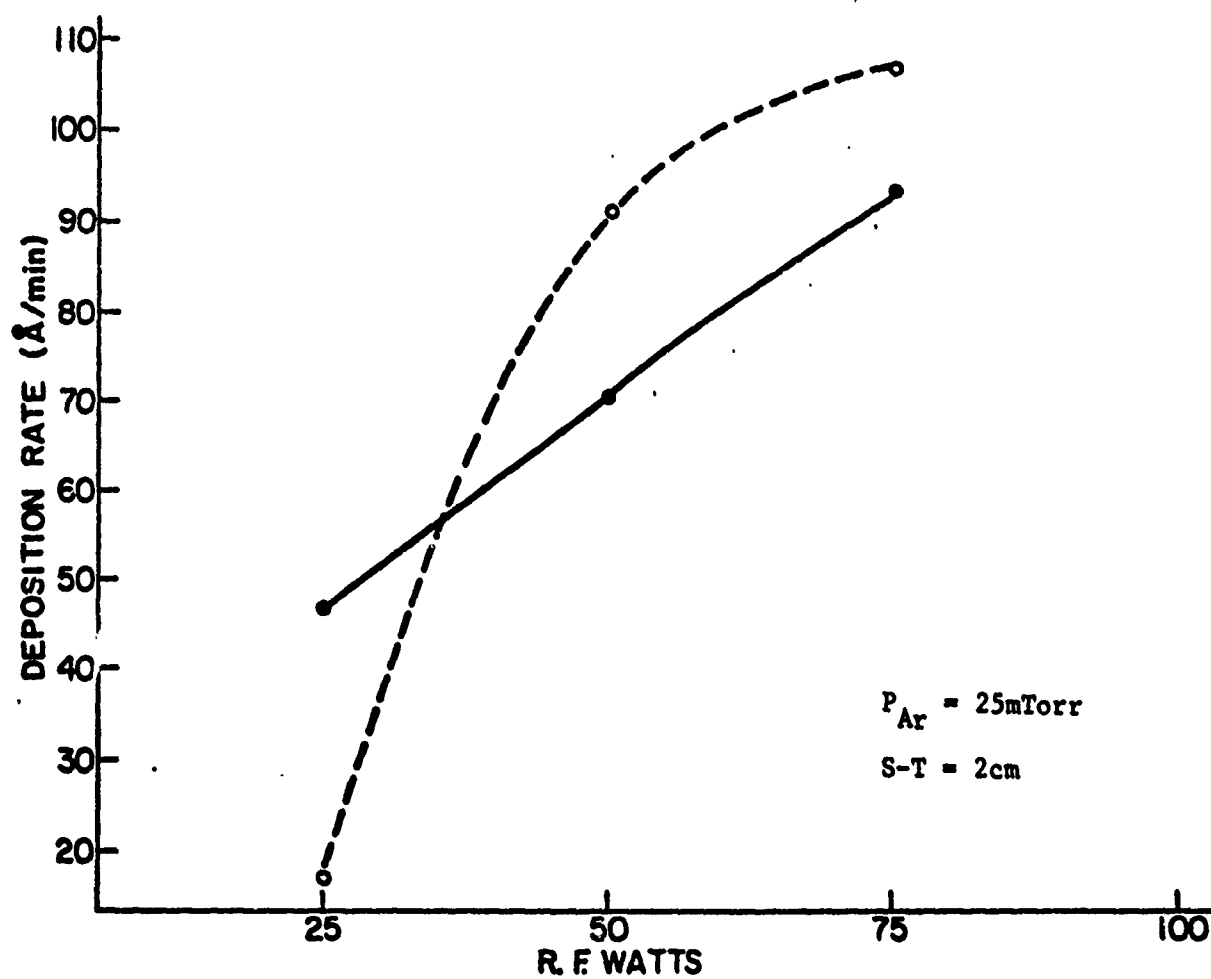


Fig. 2 Fluoropolymer film deposition rate vs power using Perkin-Elmer Randex sputtering unit.

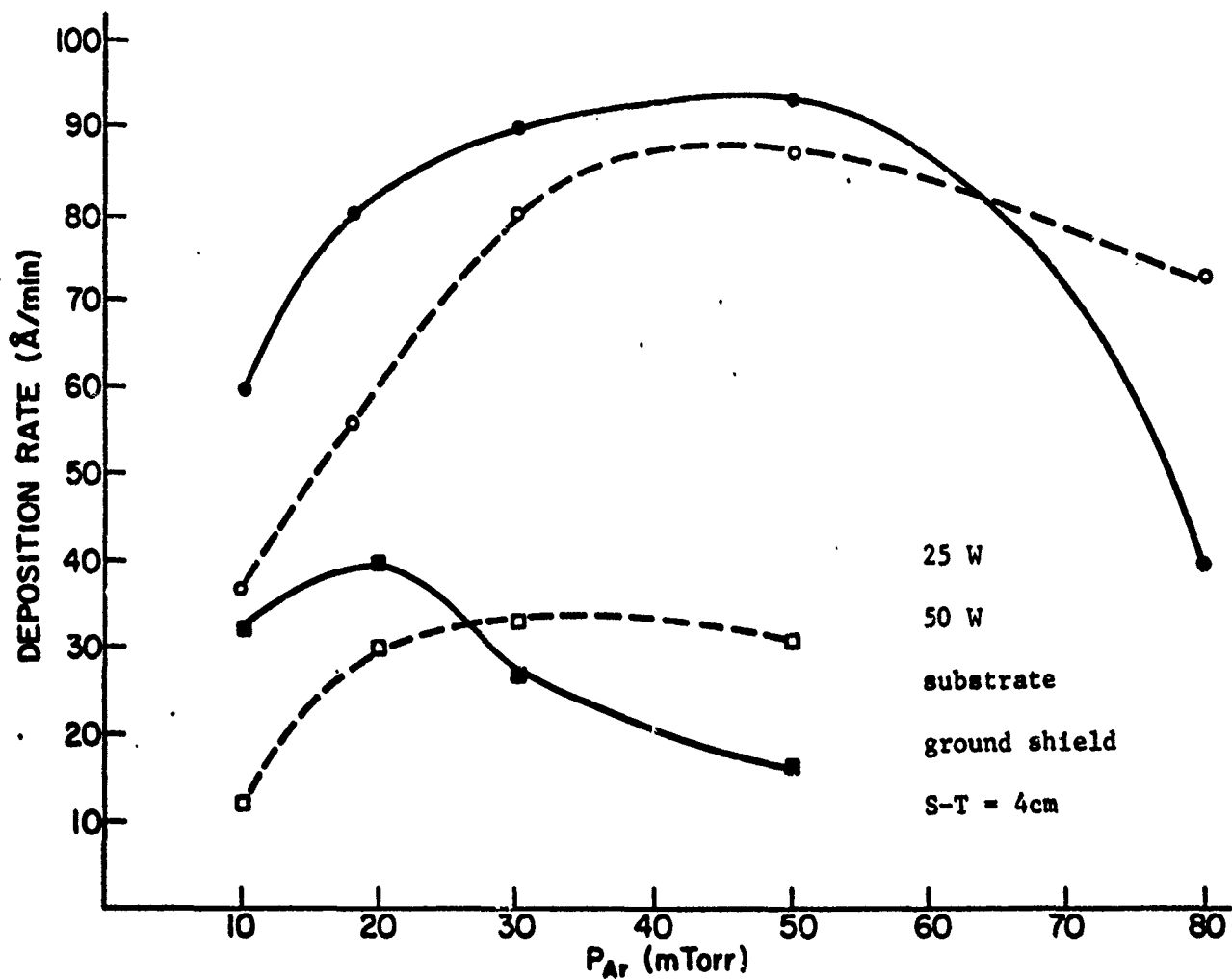


Fig. 3 Fluoropolymer film deposition rate as a function of sputtering gas pressure.

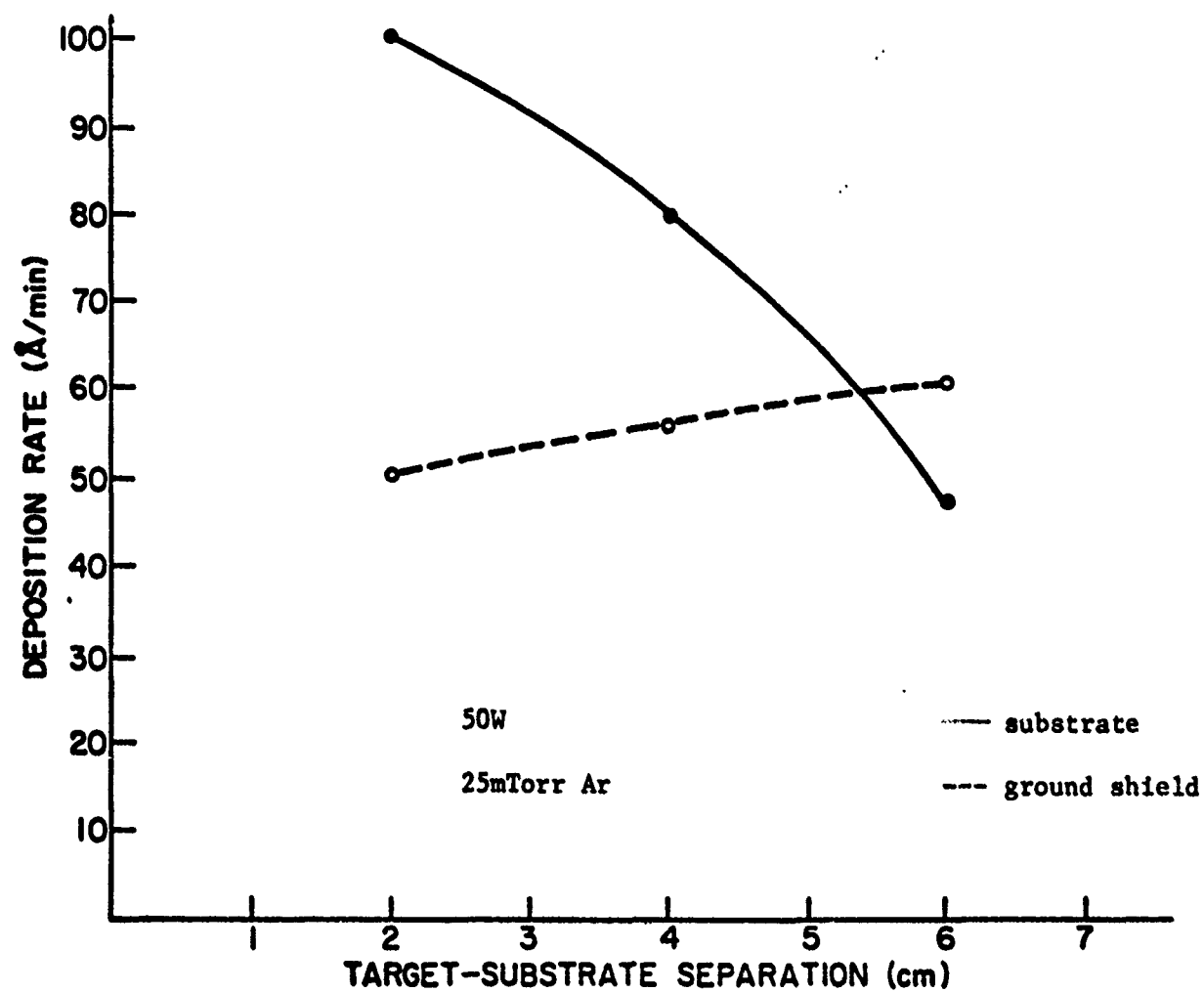


Fig. 4 Fluoropolymer film deposition rate at different target-substrate separations.

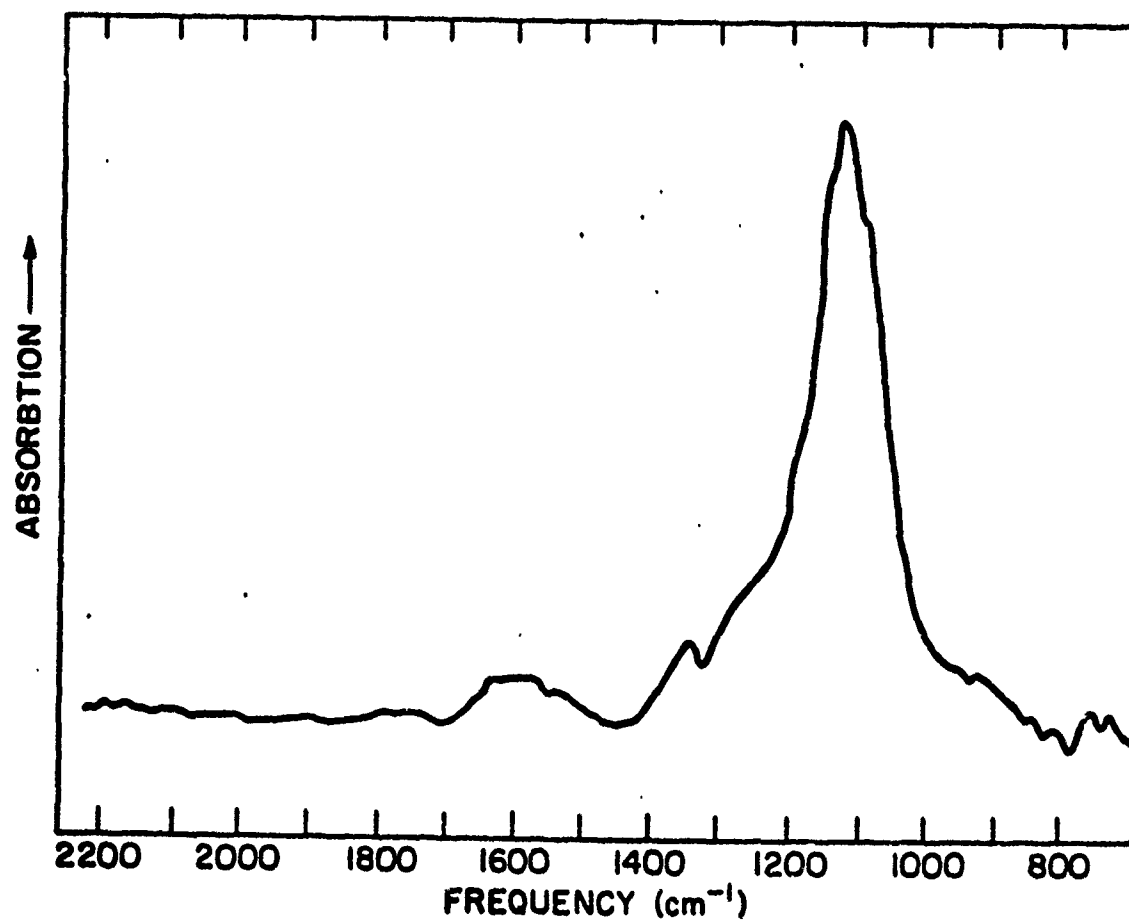


Fig. 5 Fourier transform infrared spectrum of sputtered fluoropolymer film.

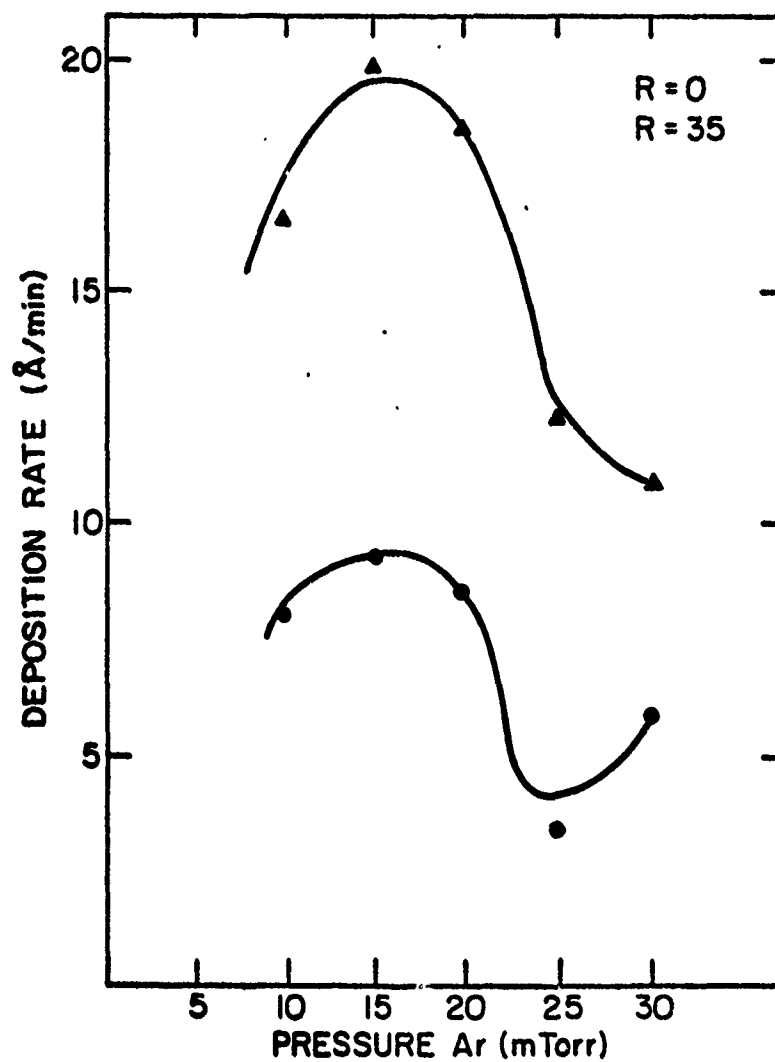


Fig. 6 Polyester film deposition rate as a function of sputtering gas pressure at two different substrate positions under the polymer target.

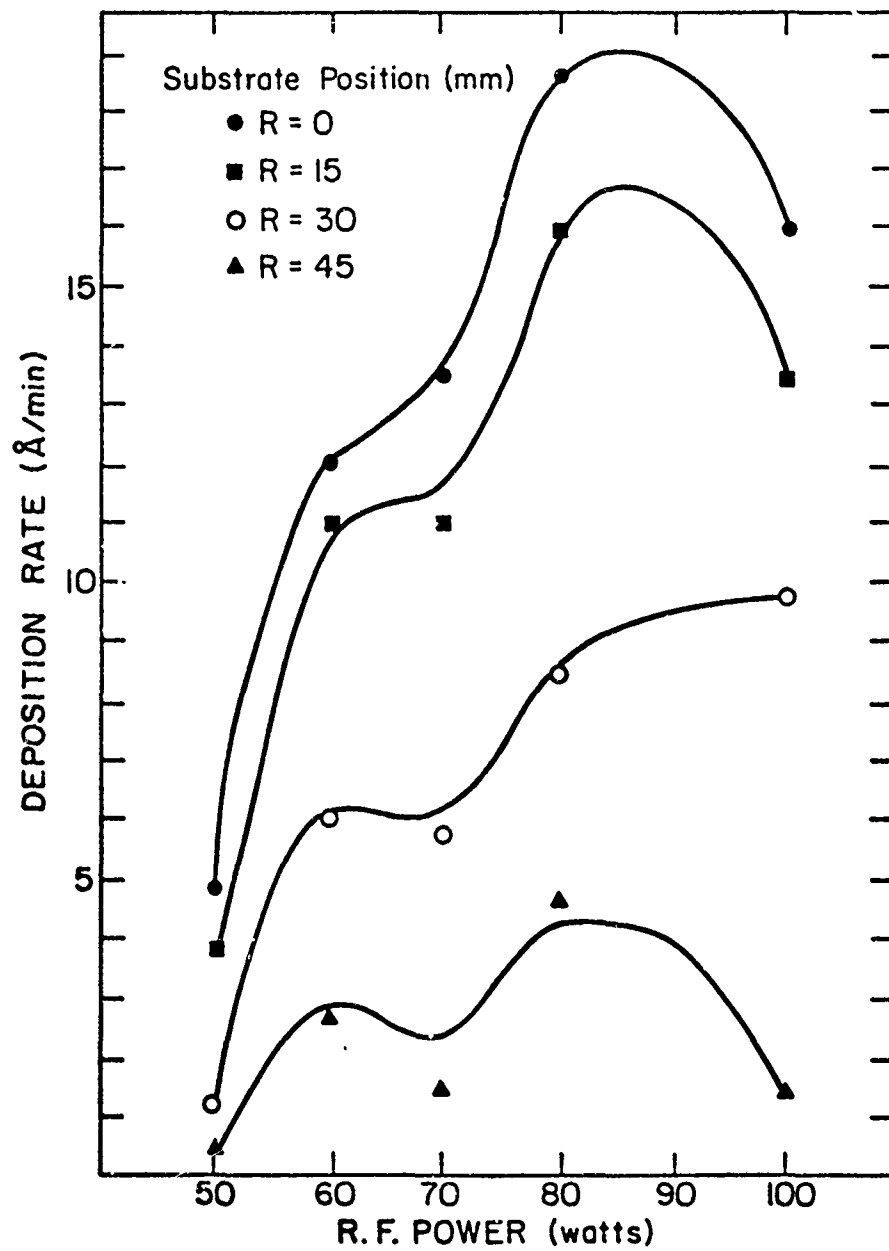


Fig. 7 Polyester film deposition rate vs power at different substrate positions under the polymer target.

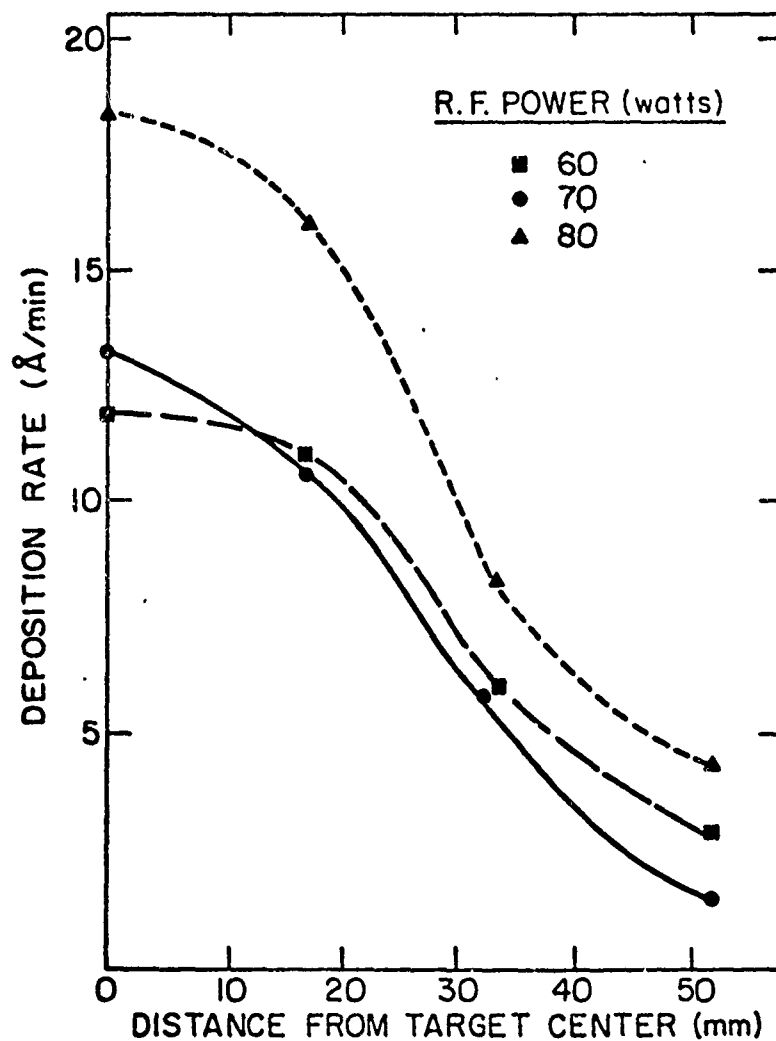


Fig. 8 Polyester film deposition rate vs substrate position shown at different power levels.

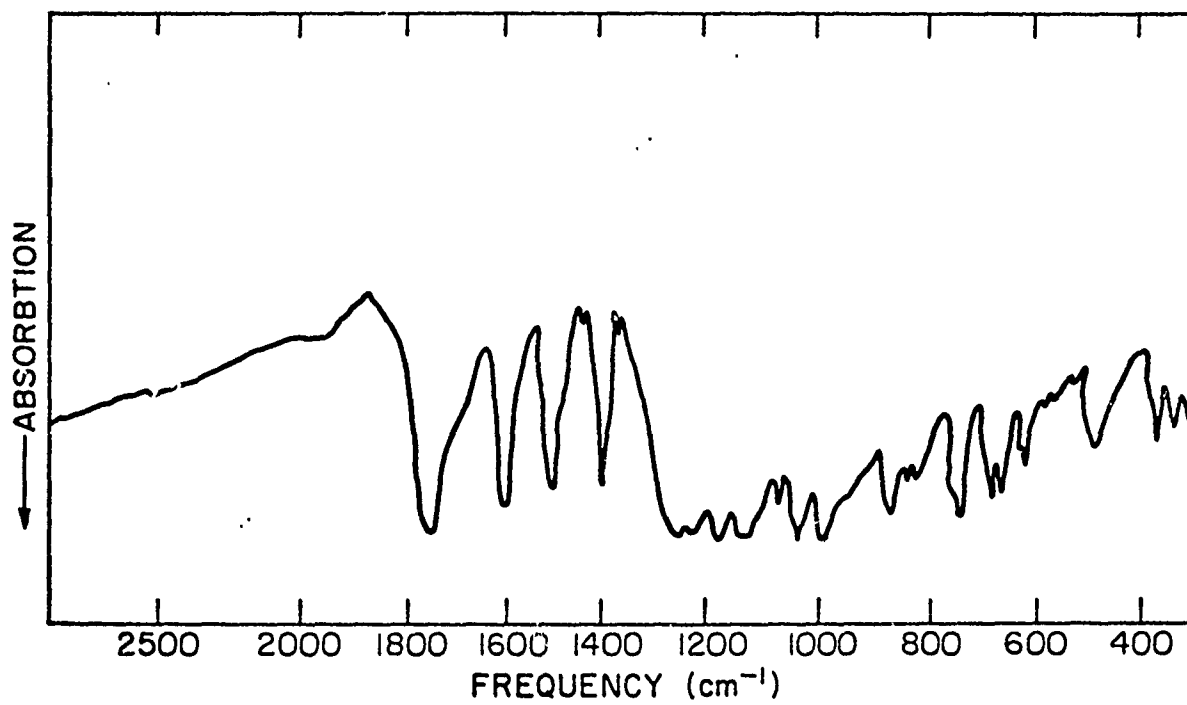


Fig. 9 Bulk polyester infrared absorbtion spectrum.

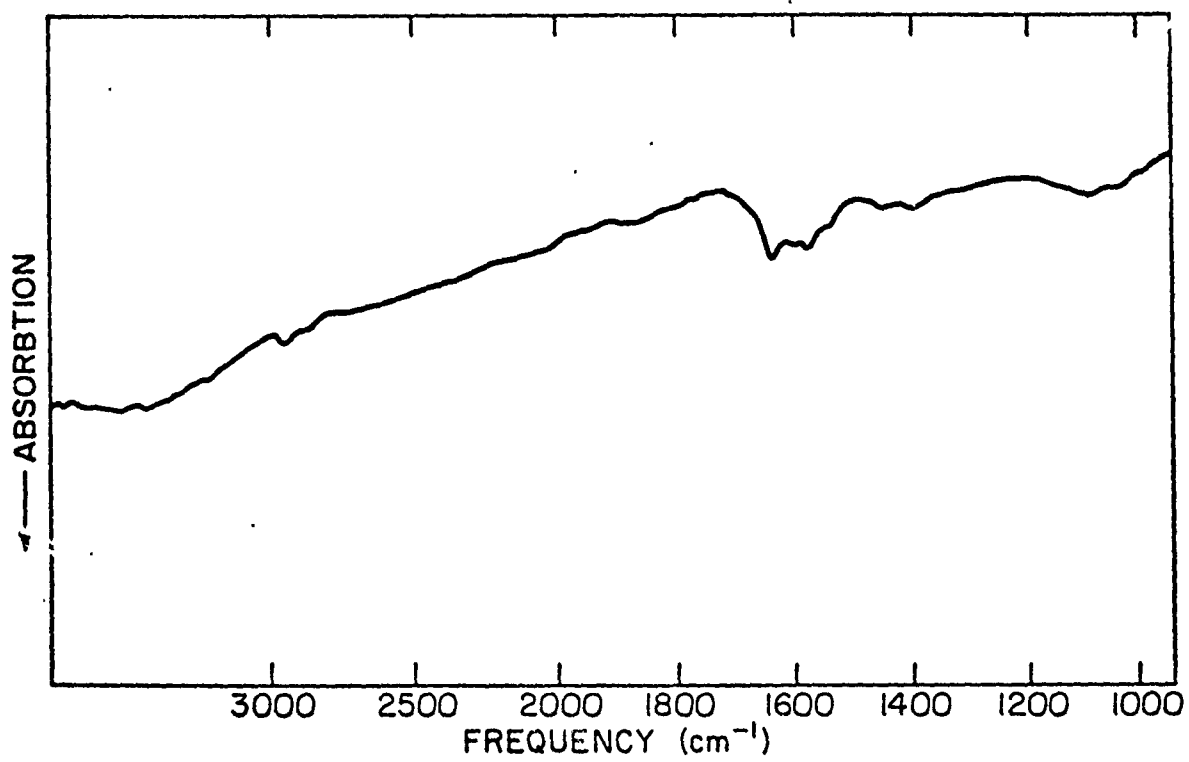


Fig. 10 Typical sputtered polyester film infrared absorbtion spectrum.

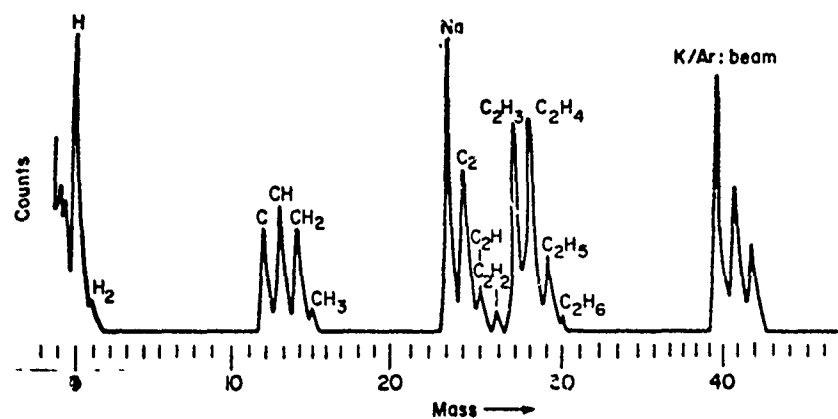


Fig. 11 Sputtered polyester film mass spectrum taken by SIMS.

- ⊙ SPUTTERING GAS
- TARGET MATERIAL

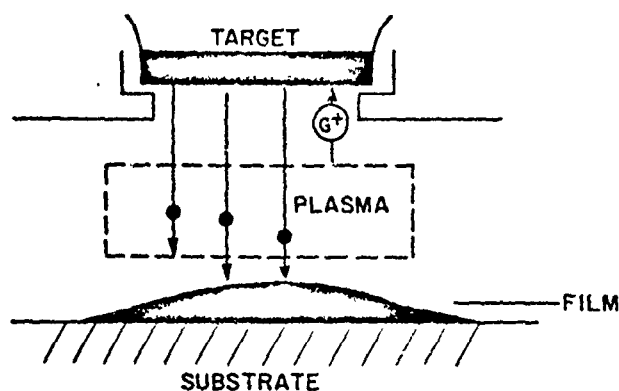


Figure 12(a)

- ⊙ SPUTTERING GAS
- ⊙ GAS EVOLVED FROM TARGET
- ⊙* ACTIVATED SPECIES

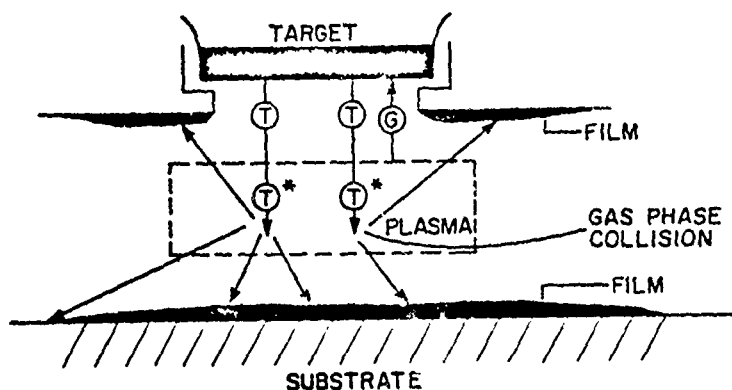


Figure 12(b)

- ⊙ SPUTTERING GAS
- ⊙ TARGET SPECIES
- RE-SPUTTERED FILM

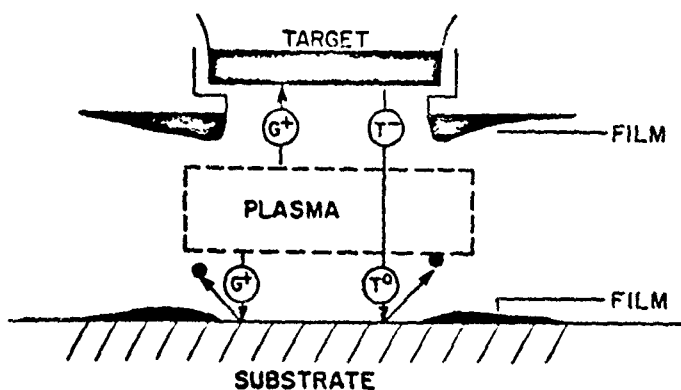


Figure 12(c)

Schematic of processes contributing to polymer film formation when the target is exposed to an rf-plasma. 12(a) shows film accumulating from direct transfer of target material to the substrate below. 12(b) shows possible areas where re-polymerized gaseous low molecular wt. species will deposit to form film. 12(c) suggests film deposition behavior if substrate film re-sputtering occurs either from negative or positive ion induced bombardment at the substrate.

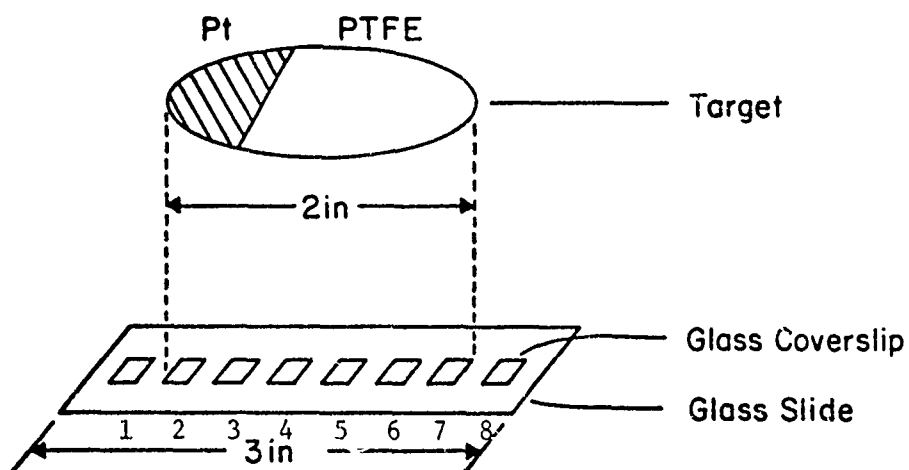


Fig. 13 Substrate and target geometry used to vary film composition in PTFE/Pt sputtering.

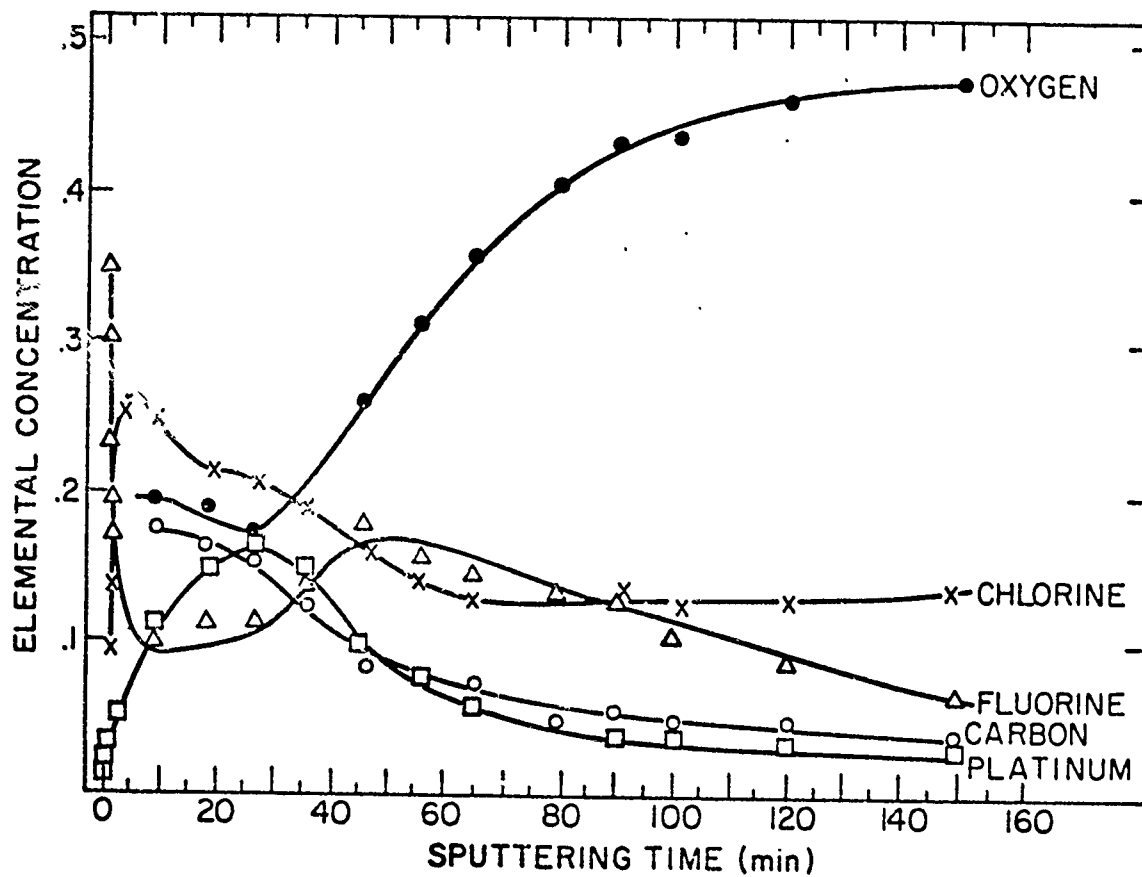


Fig. 14 Elemental film profile of sputtered PTFE/Pt film from ISS spectra of substrate #4 of Fig. 13. Of significance is the relative variation of Pt vs film depth.

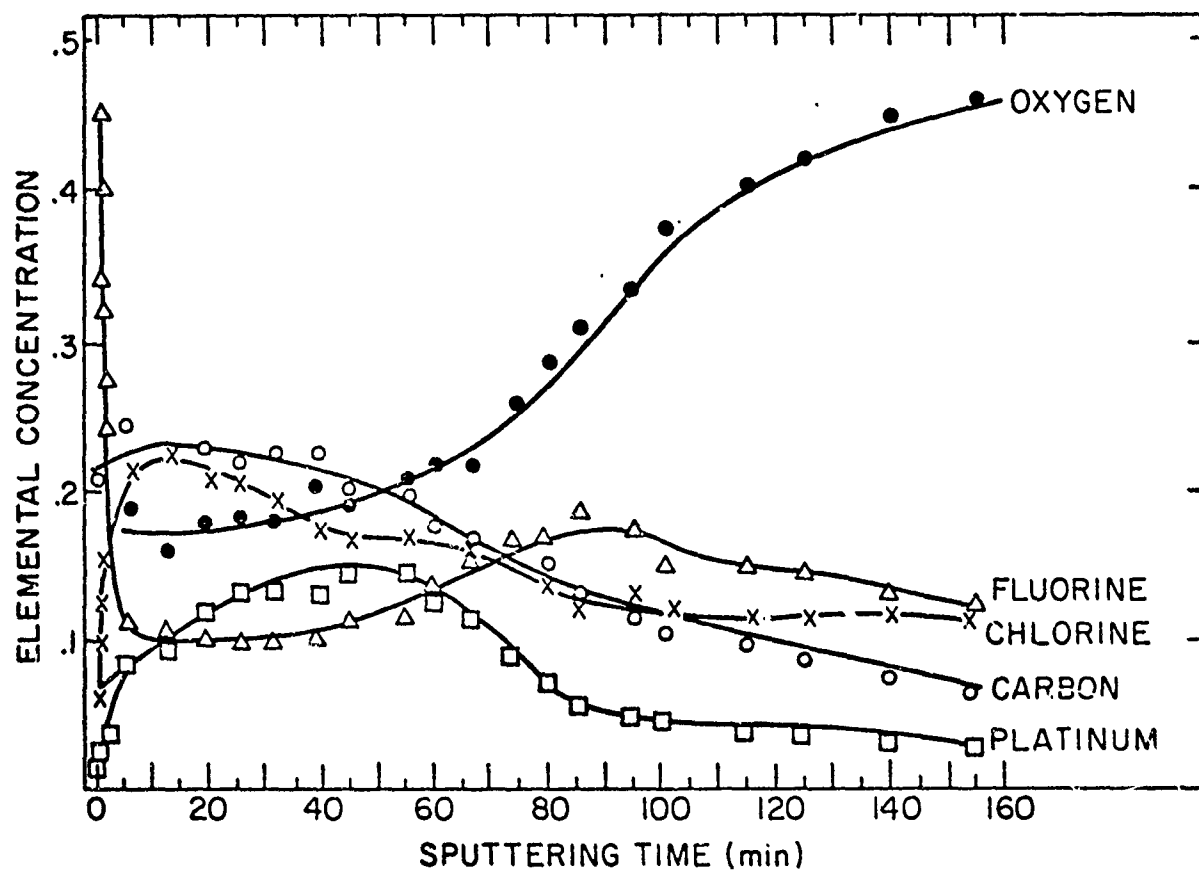


Fig. 15 Elemental ISS profile of film from position #5 of Fig. 13 showing the same Pt concentration behavior as the adjacent substrate #4.

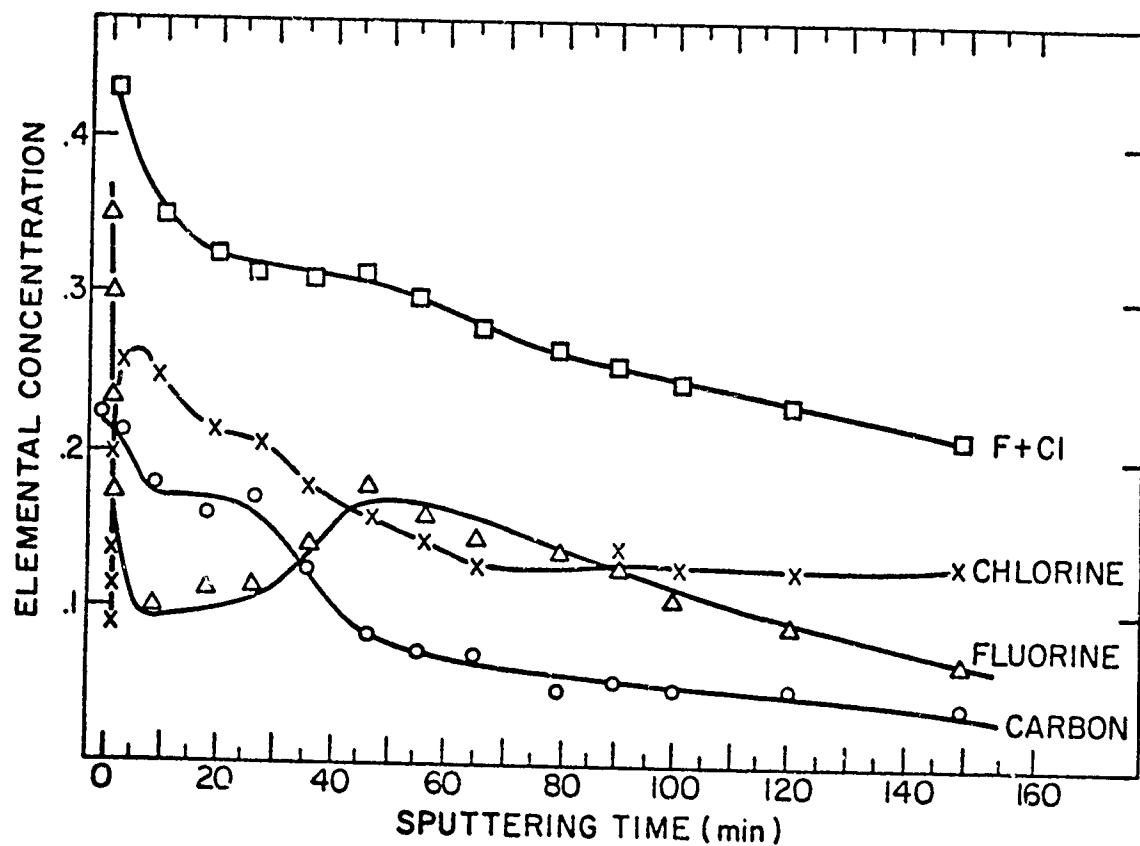


Fig. 16 Carbon and halogen signals with the sum of F+Cl signals also plotted for film substrate #4 of Fig. 13. The F+Cl and carbon signals appear parallel suggesting Cl substitution in the sputtered polymer film.

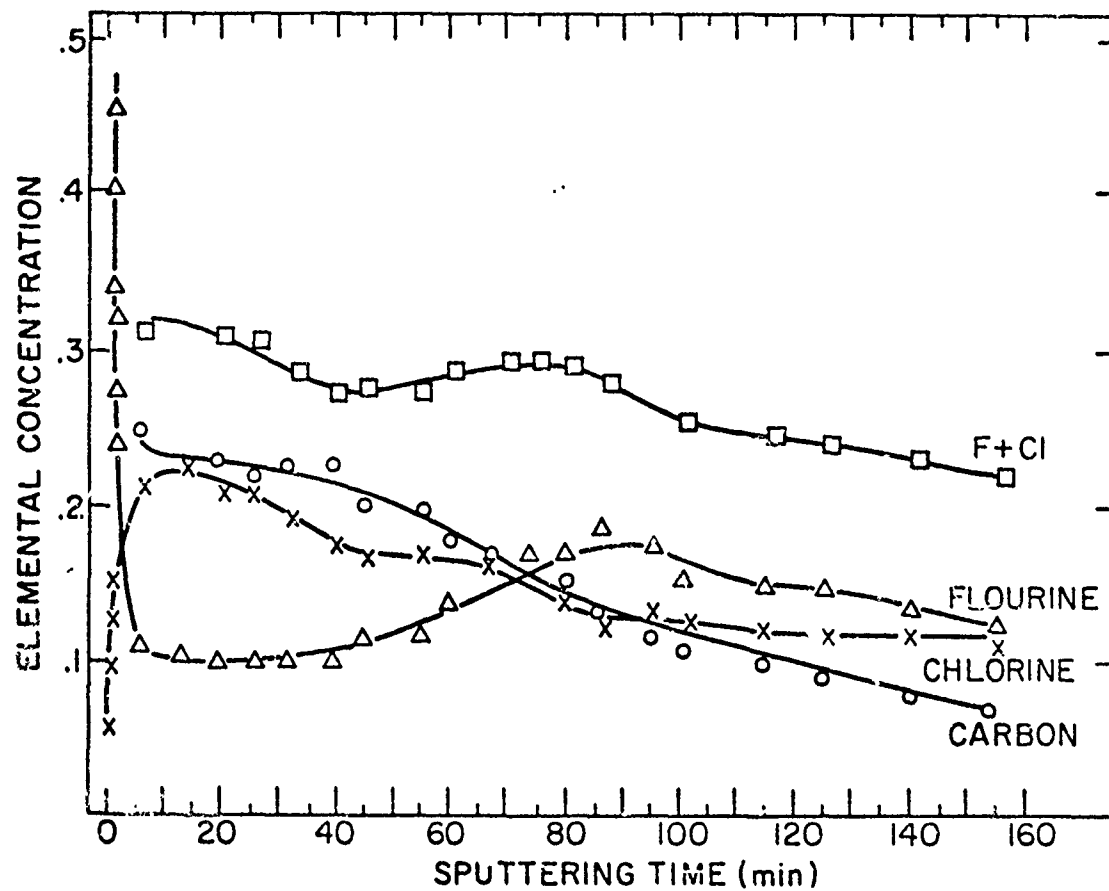


Fig. 17 Carbon, halogen, and the sum of F+Cl signals plotted for film substrate #5 of Fig. 13 showing similar behavior as substrate #4.

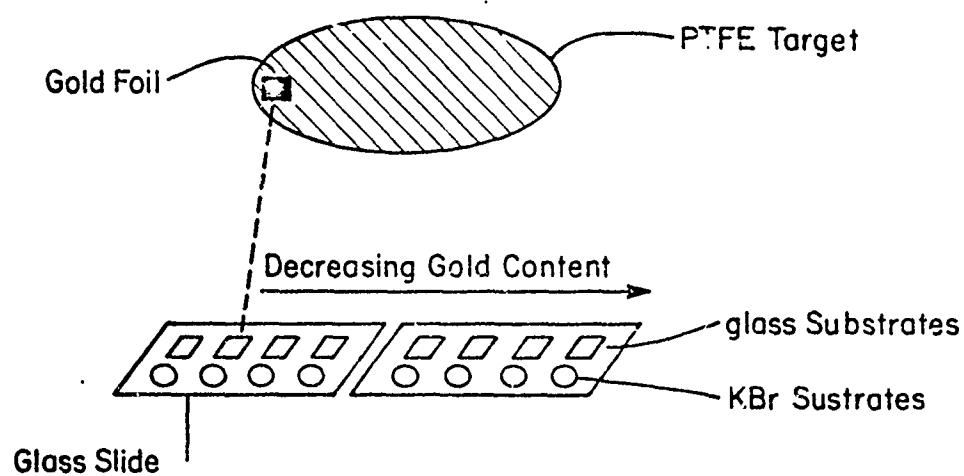


Fig. 18 PTFE/Au target and substrate geometry.

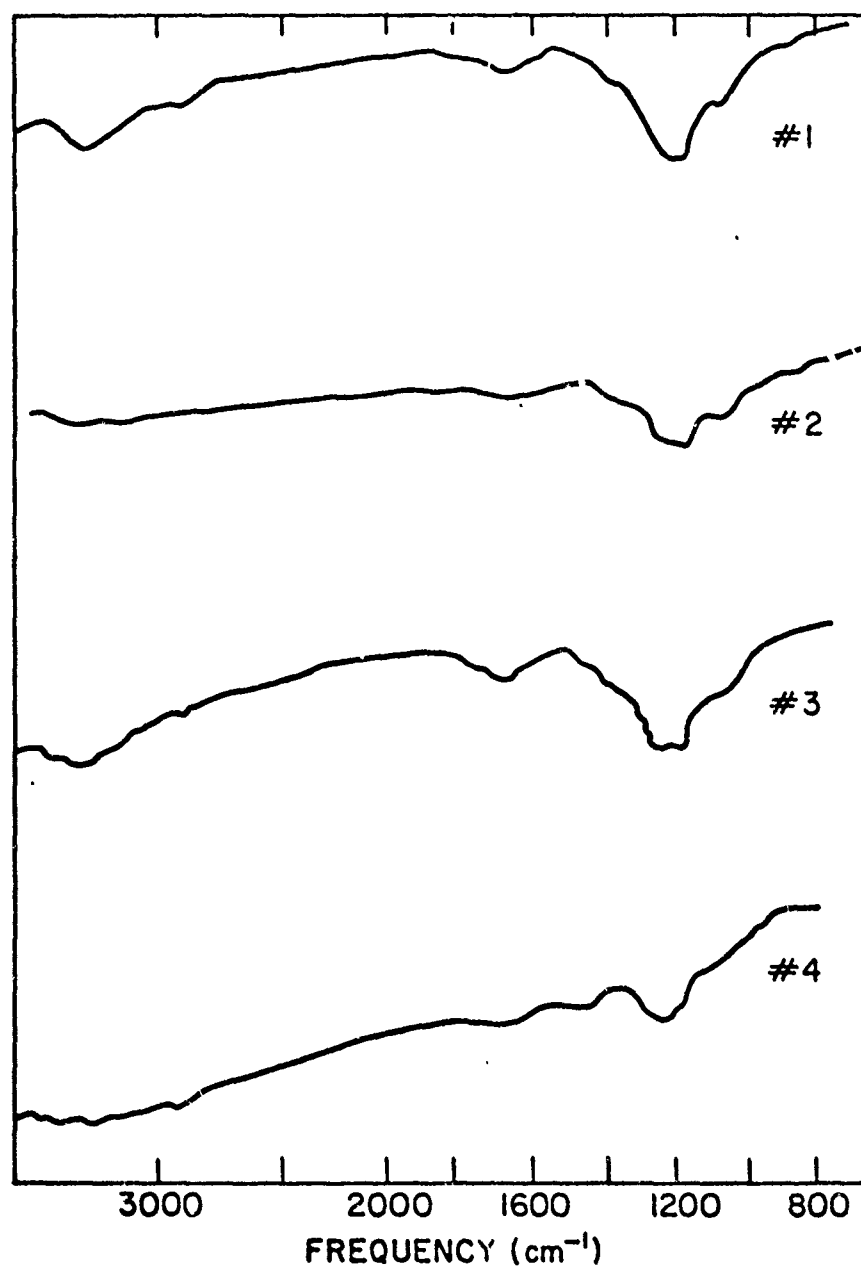


Fig. 19 Infrared absorption spectra of PTFE/Au sputtered films at different substrate positions showing a broad absorption at 1200cm^{-1} .

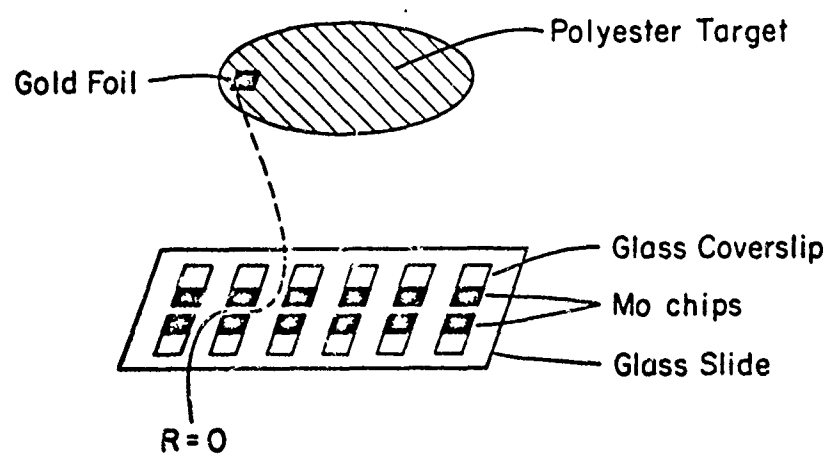


Fig. 20 Polyester/gold target and substrate geometry used for resistivity measurements on sputtered films.

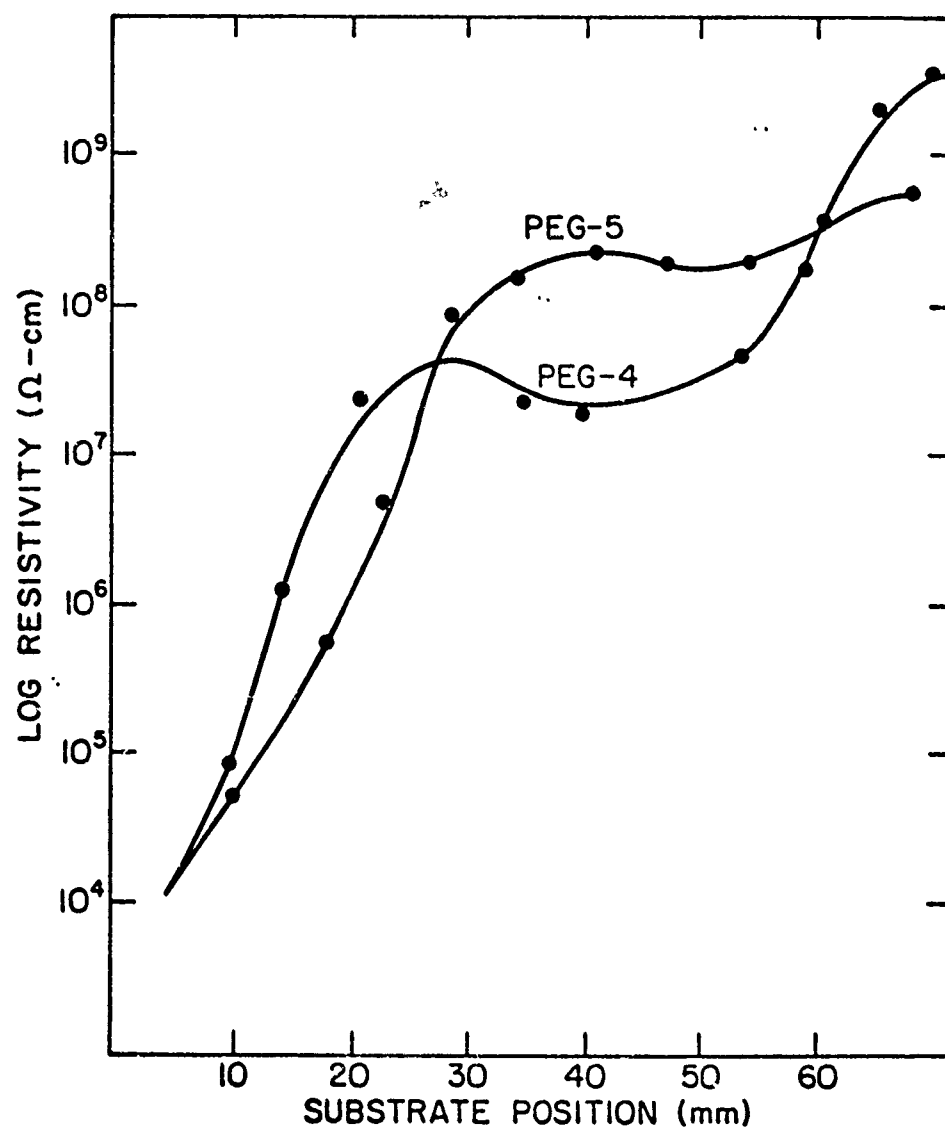


Fig. 21 DC resistivity vs distance from under the gold target for films deposited at 70W(PEG-4) and 80W(PEG-5).

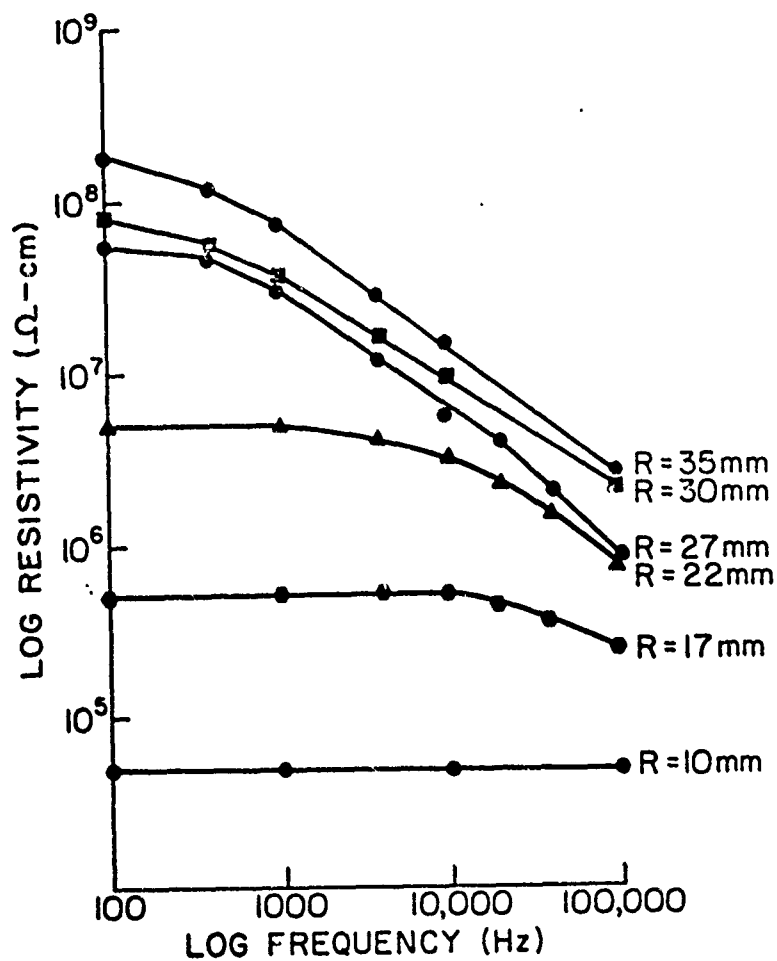


Fig. 22 AC resistivity for polyester-gold films deposited at 80 watts. Shown are a series of curves for different substrate positions with respect to the gold portion of the target.

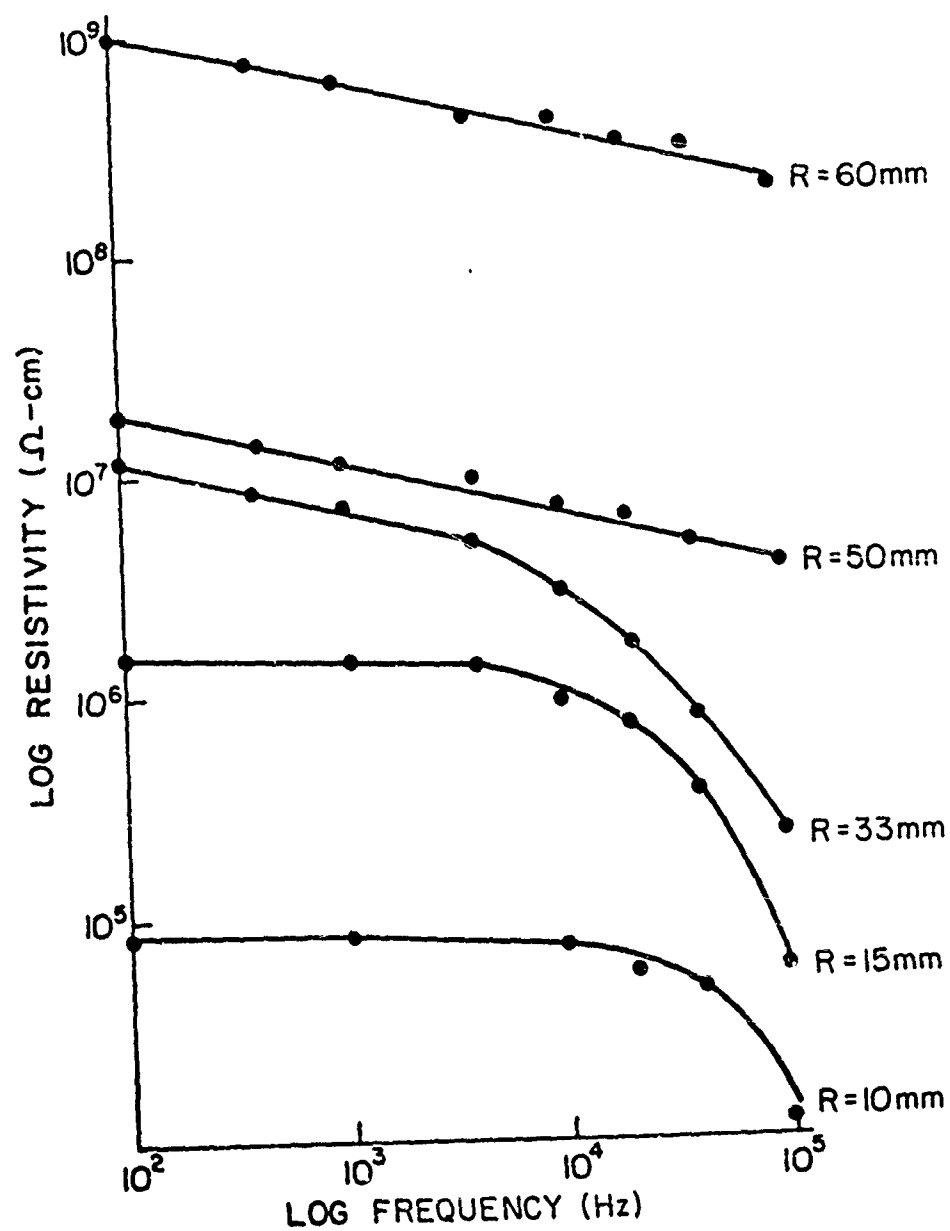


Fig. 23 AC resistivity of sputtered polyester/gold films deposited at 70W power.

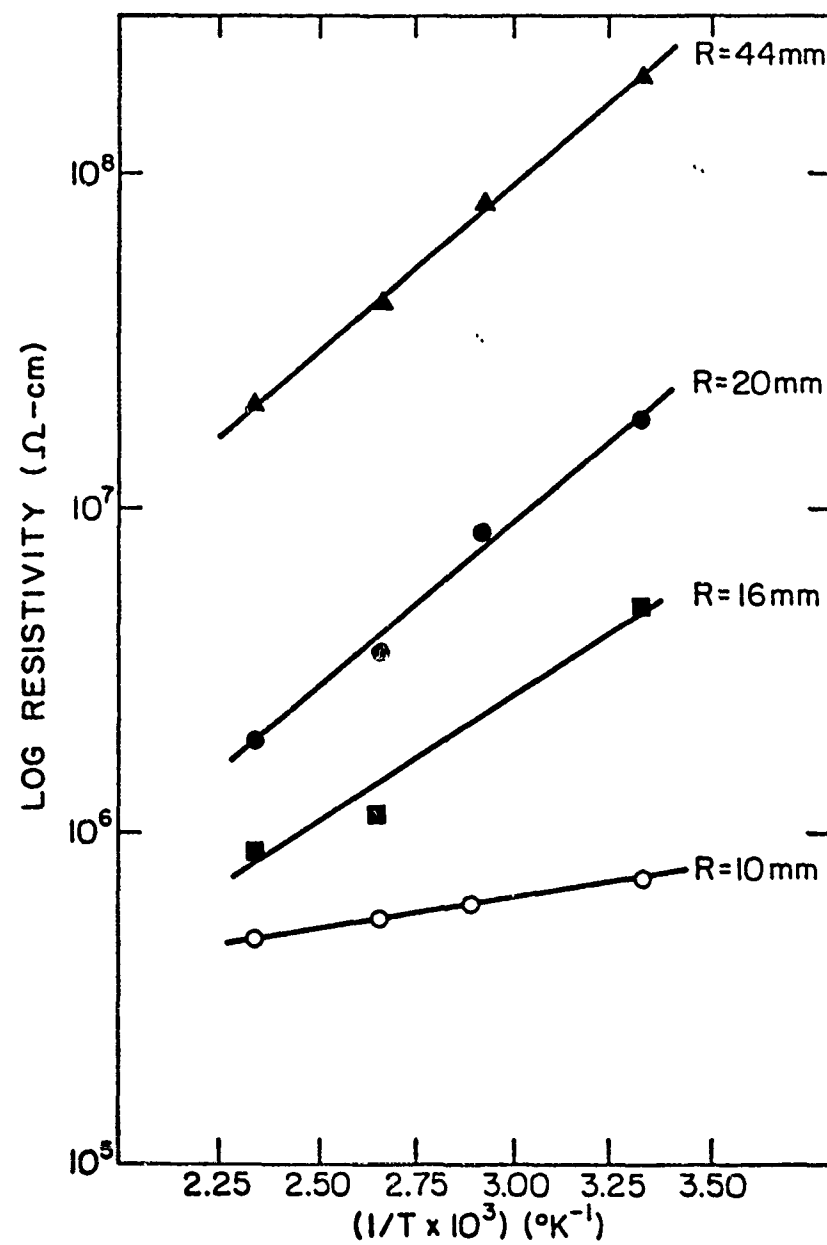


Fig. 24 DC resistivity vs reciprocal temperature for polyester/
gold films deposited at 80W.

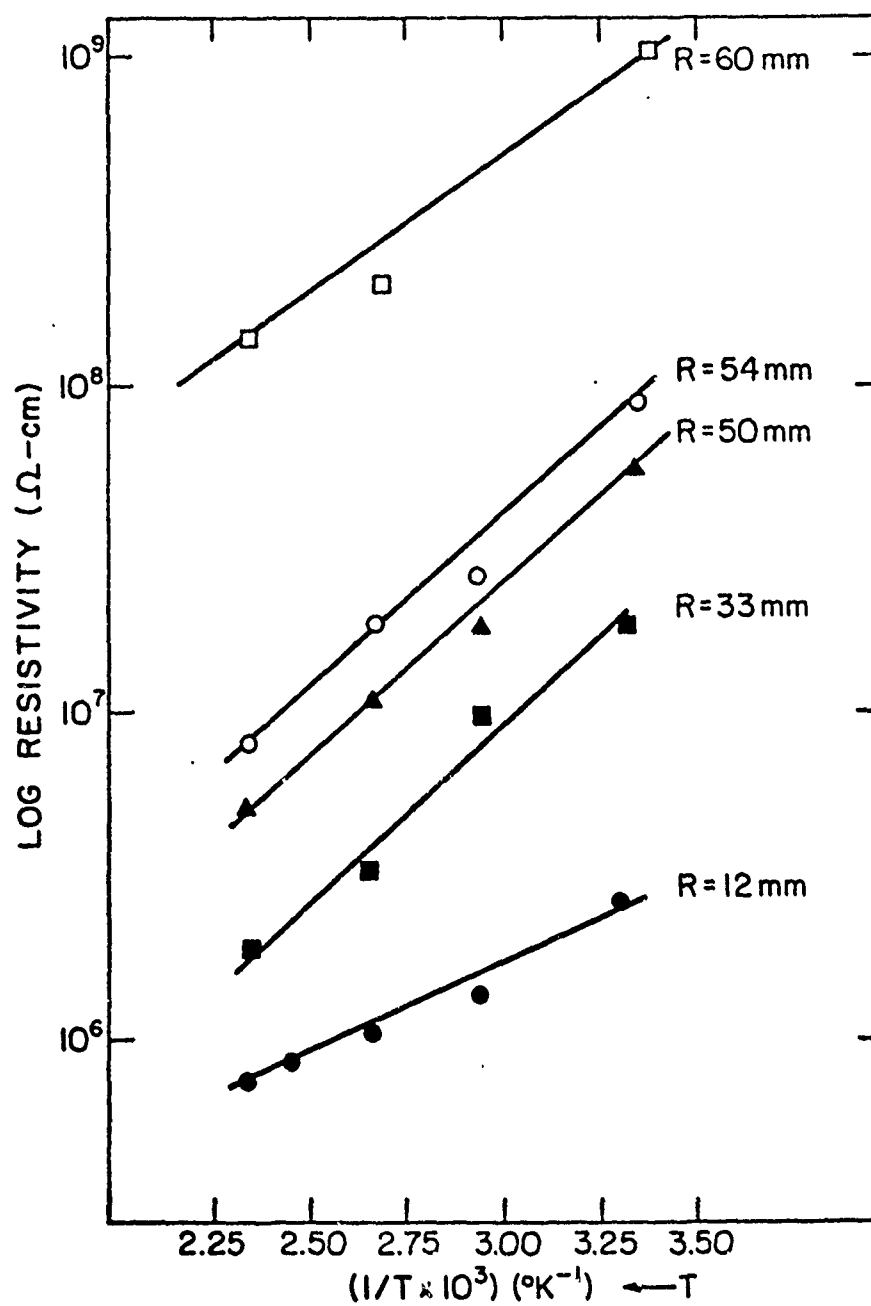


Fig. 25 DC resistivity vs reciprocal temperature for polyester/
gold films deposited at 70W.

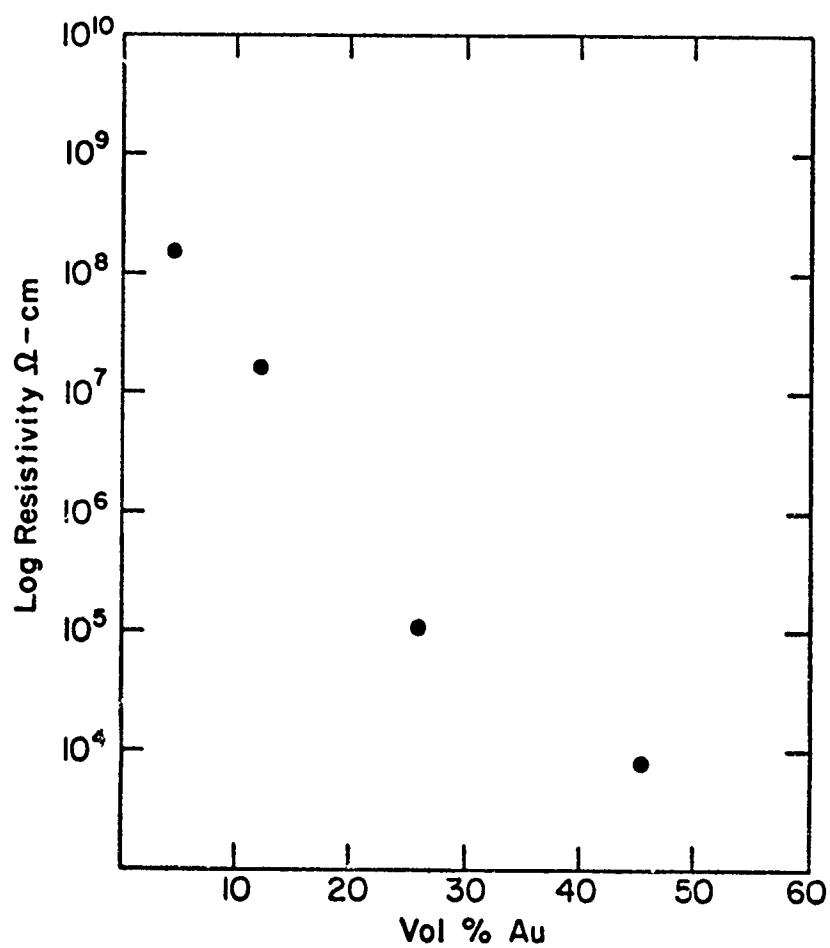
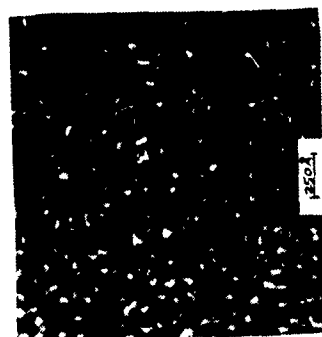


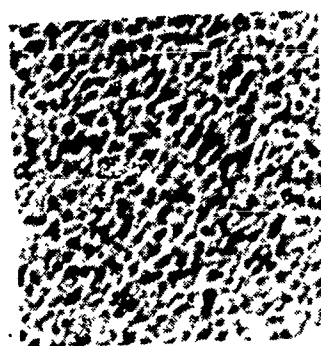
Fig. 26 DC resistivity vs volume % gold in sputtered polyester/gold films deposited at 80W power.



$R = 18\text{mm}$



$R = 9\text{mm}$

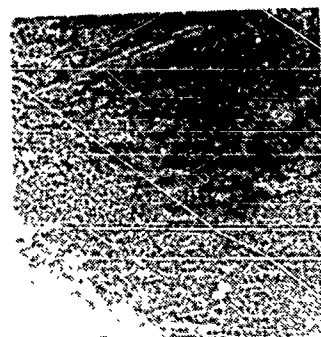


$R = 0$



$R = 30\text{mm}$

TEM OF SPUTTERED POLYESTER-GOLD FILMS
AS A FUNCTION OF RADIAL DISTANCE



$R = 27\text{mm}$

Fig. 27 Bright field TEM micrographs of sputtered polyester/gold films as a function of distance from the gold target at 40W power.

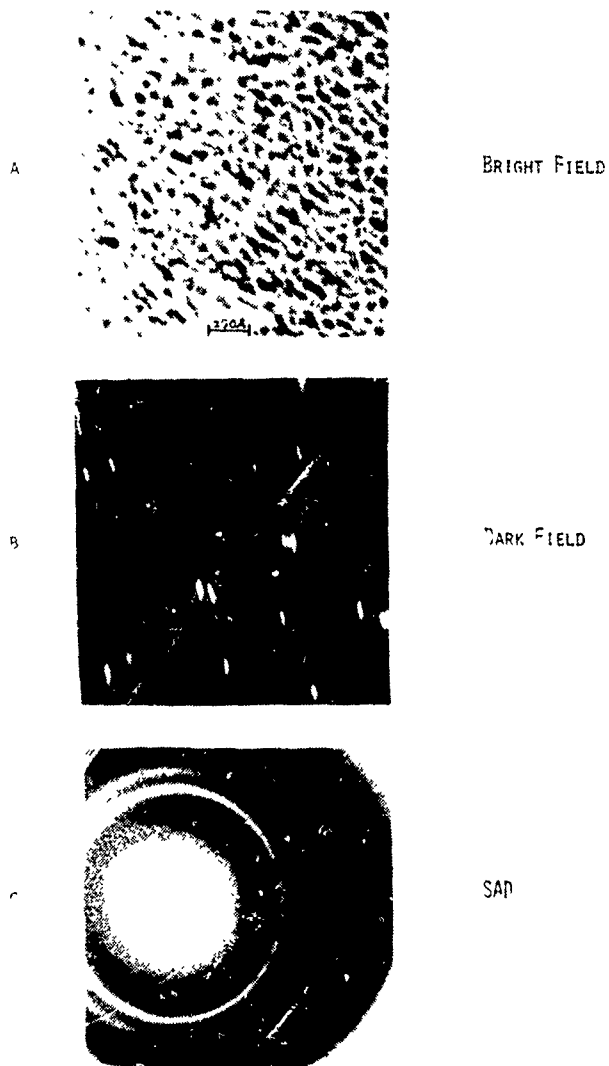


Figure 28(a) Sputtered Polyester-Gold
 Film deposited at 40W
 for position $R=0$.

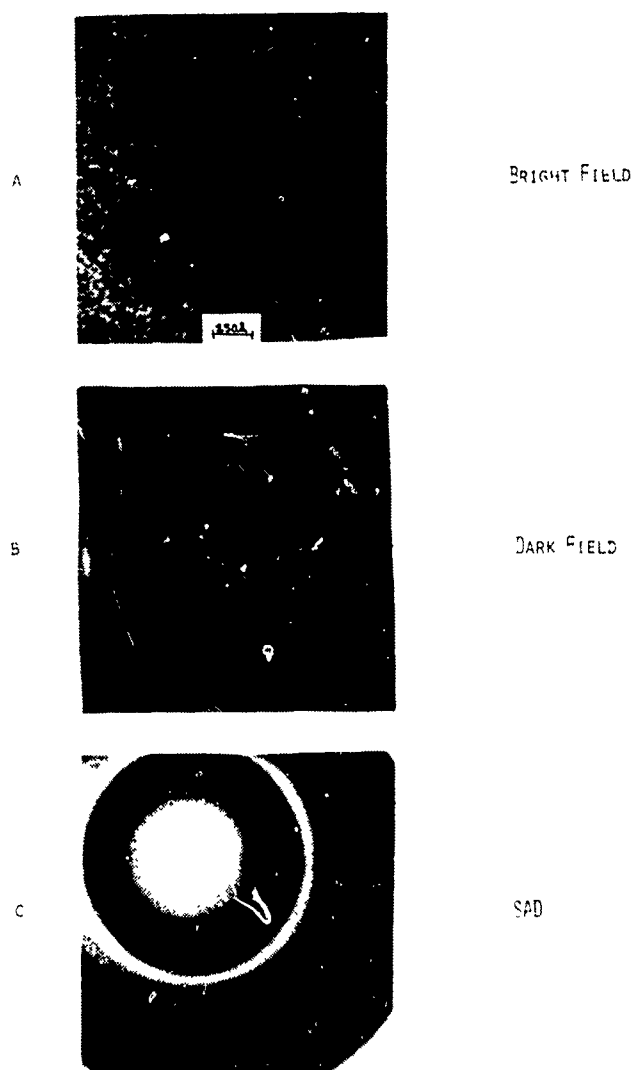


Fig. 28(b) TEM of Sputtered Polyester-Gold
 Film deposited at 40W for
 position $R = 18\text{mm}$

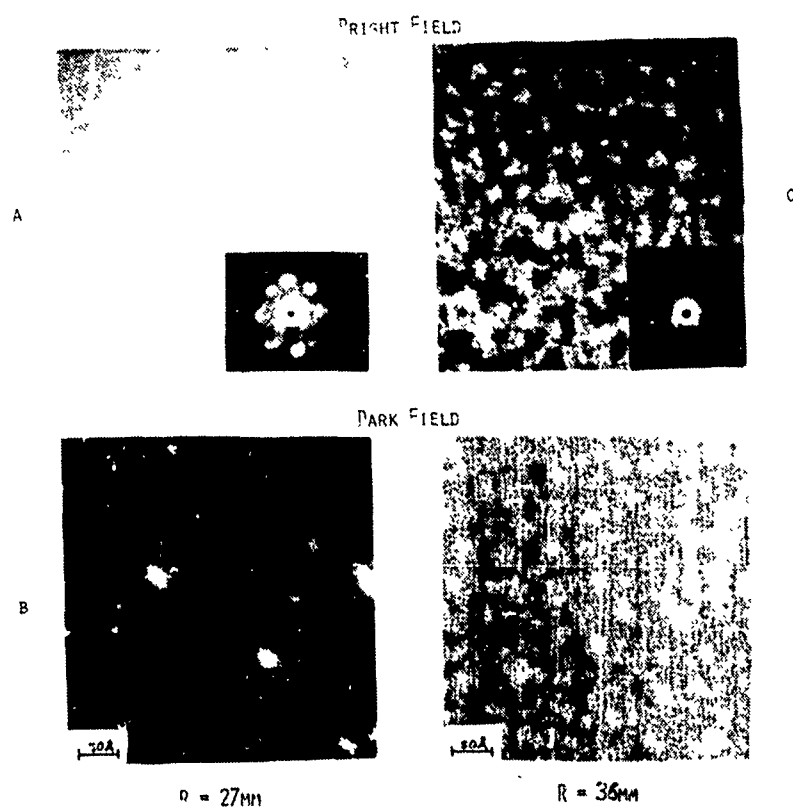


Fig. 29 High resolution STEM micrographs of polyester-gold films. Insert shows single particle diffraction pattern.

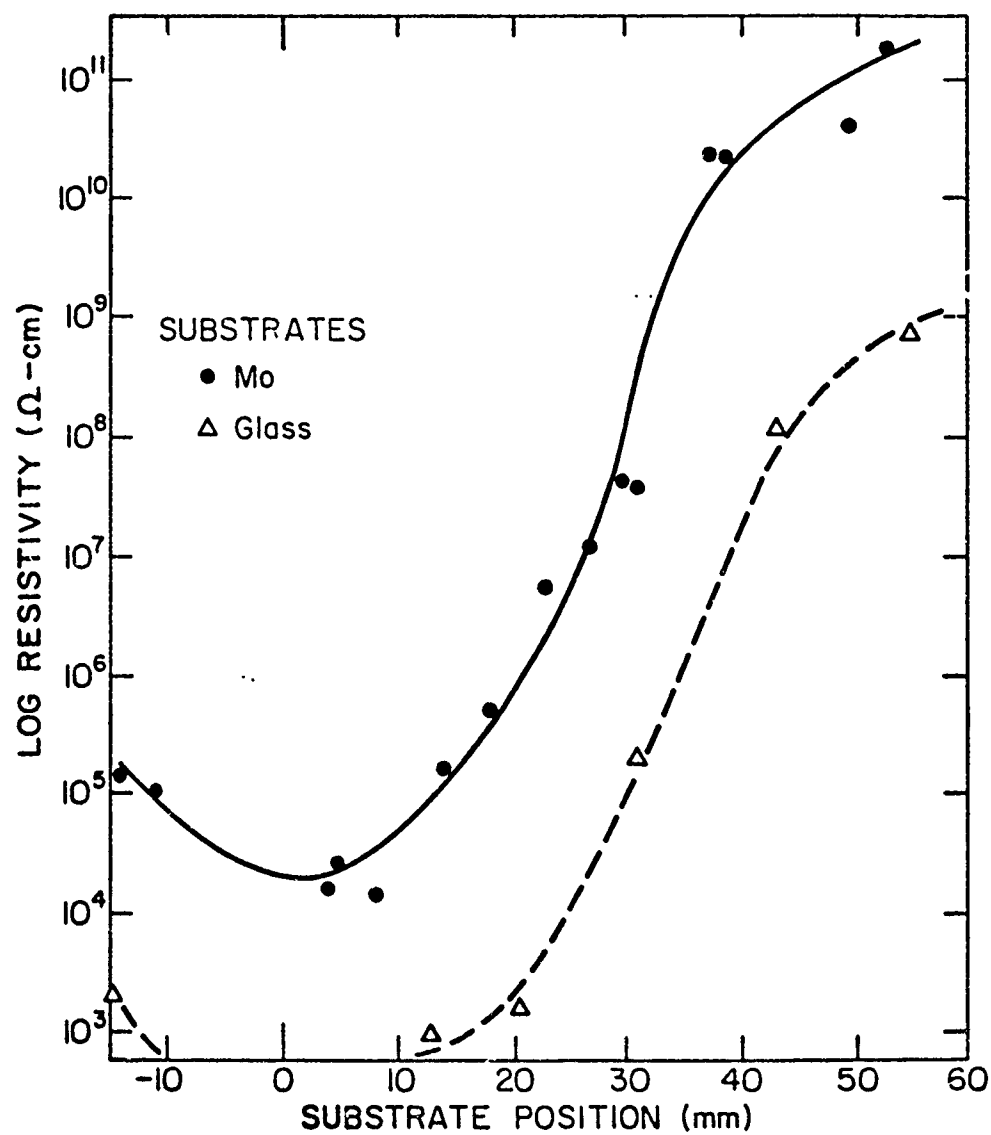


Fig. 30 DC resistivity of sputtered polyester/gold films deposited on metal and glass substrates simultaneously (see Fig. 20) at 200W power.

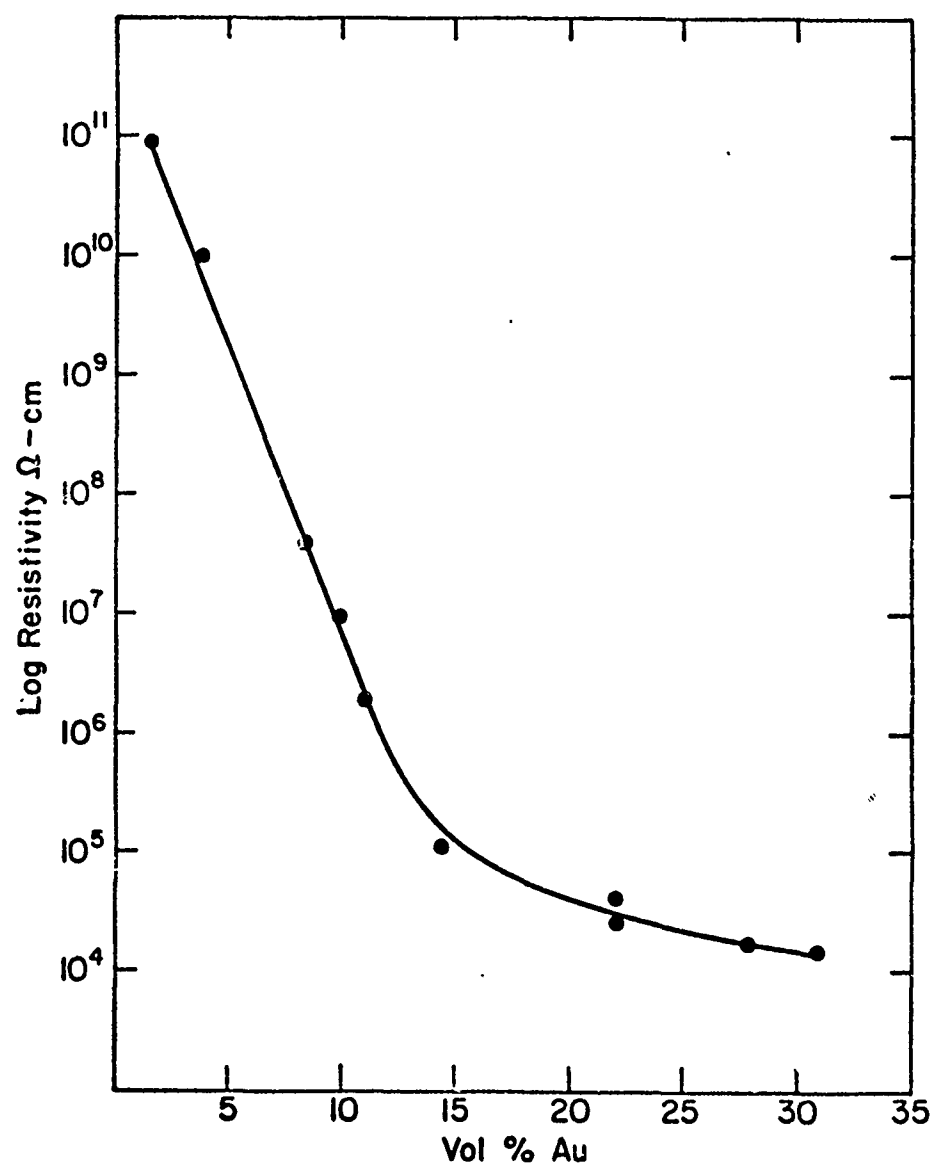


Fig. 31 Resistivity of polyester/gold films deposited at 200W shown as a function of volume % gold.

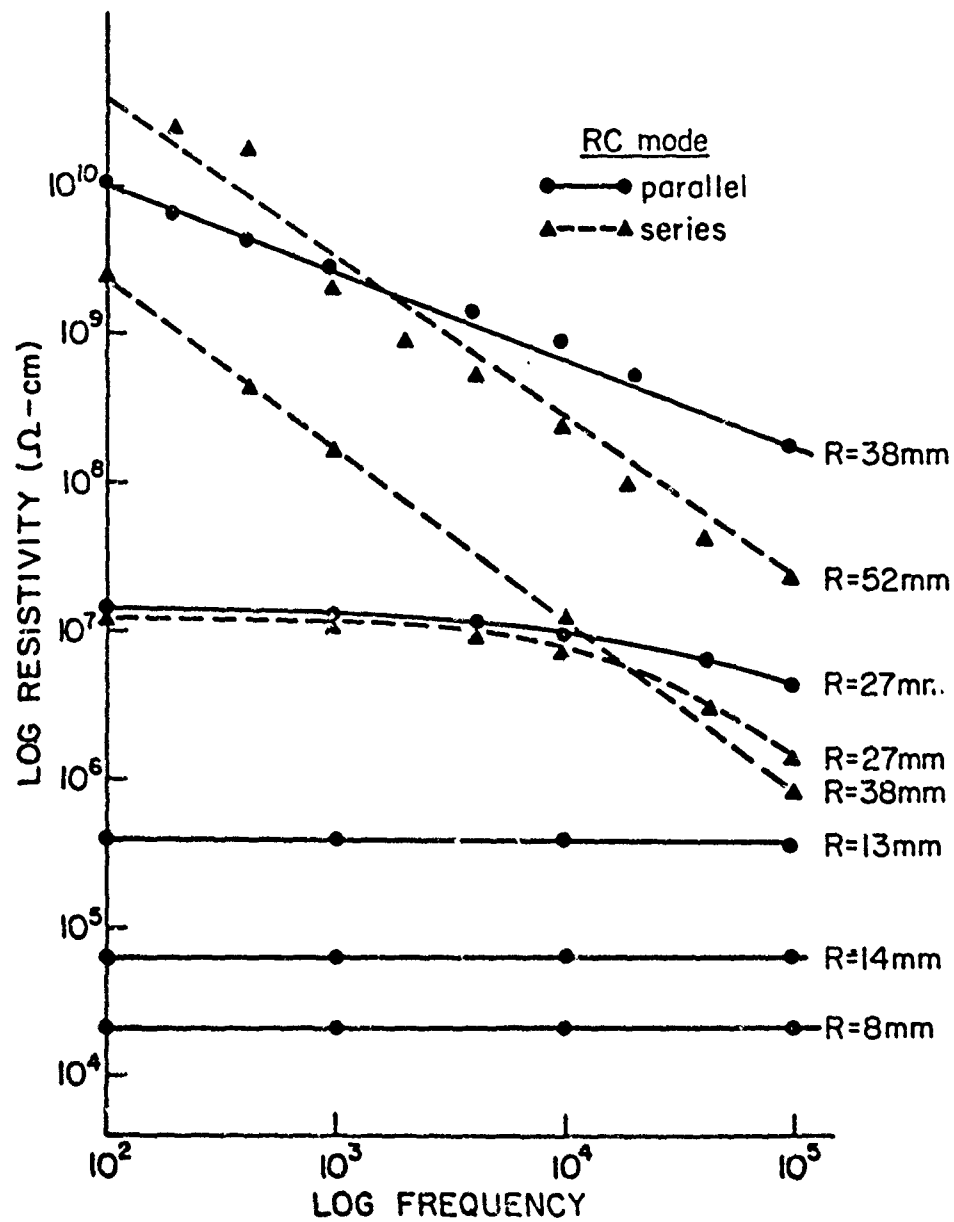


Fig. 32 AC resistivity of sputtered polyester-gold films deposited at 200W showing behavior similar to previous samples.

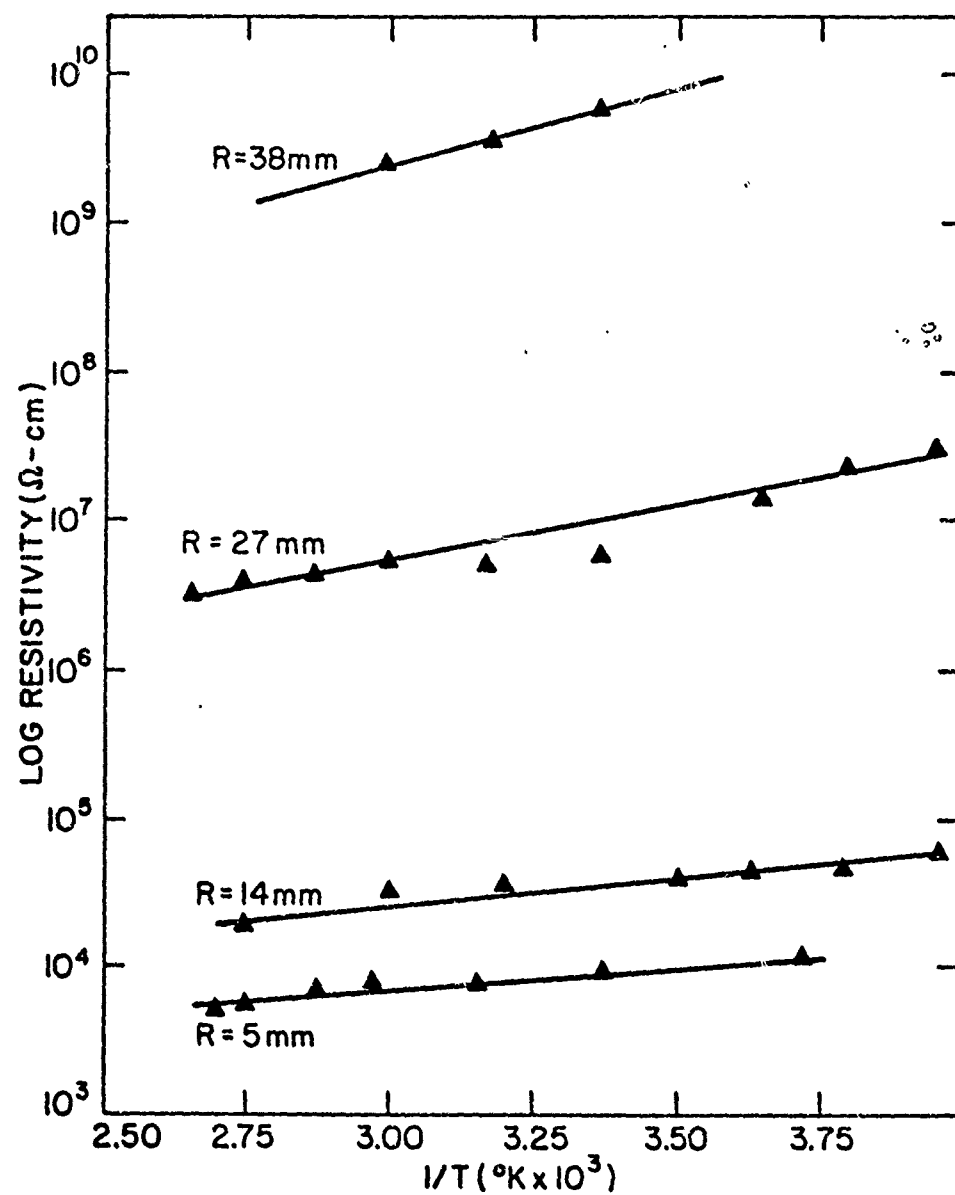


Fig. 33 DC resistivity vs reciprocal temperature for polyester/gold films sputtered at 200W.

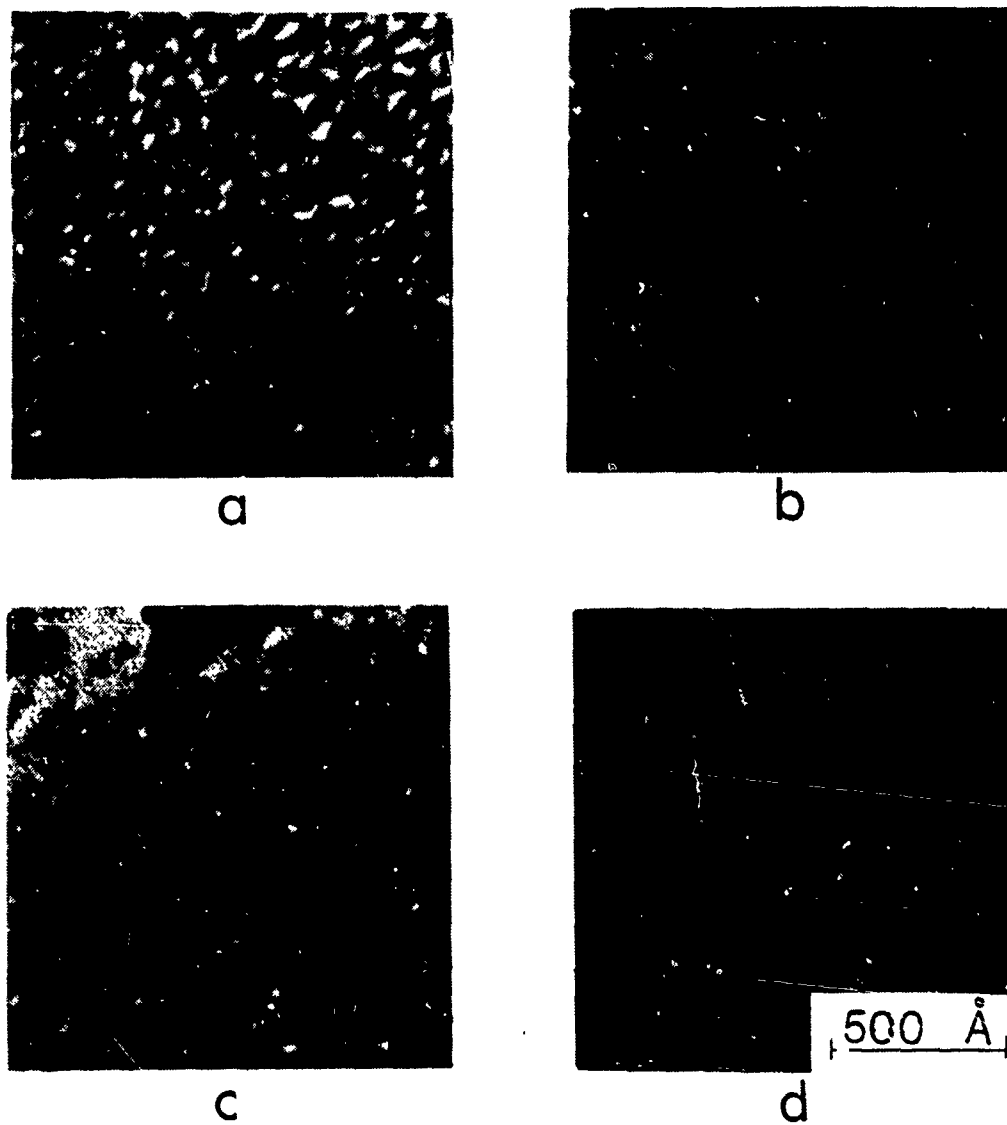


Fig. 34 Bright field TEM micrographs of polyester/gold films
deposited at 200W.

Appendix H

Preparation and Properties of Amorphous WO_3 Sputtered Films

Introduction

Among the inorganic systems exhibiting electrochromism, WO_3^* is one of the best known examples. It was first reported by Deb⁽¹⁾ that transparent films of WO_3 show electrochromic (EC) behaviour. An electrochromic material has the property of changing color when a voltage is applied across the material. The color change may be from a transparent to a colored state, or, in the case of organic electrochromics, one color to another color⁽²⁾.

Tungsten oxide WO_3 films can be colored at a low voltage (1.5-2 volts) and show a memory effect, i.e., color remains when the voltage is removed. The films become transparent only when the polarity of the applied voltage is reversed. The dark blue color in EC WO_3 films is aesthetically pleasing, with good contrast and a wide viewing angle. Due to these characteristics of WO_3 films, it was thought that a display device superior to liquid crystal displays (LCD) could be made. Hence, this possibility has provided strong motivation for work in this area.

In the past few years, properties and EC phenomena of WO_3 films has been extensively investigated by a number of groups (eg., RCA, CNRS-France, Imperial College, IBM, Bell Labs, etc.). Despite the large amount of development work on WO_3 towards realizing a technically useful display device, there are still some gaps in our understanding of electrochromism in WO_3 films, especially in the material characterization of these films (for instance, see review by Faughnan and Cranall, Reference 3). In the following section we shall see this in more detail.

*The exact composition, generally $\text{H}_x\text{W}_y\text{O}_{3-y}$, is variable with preparation conditions and post-deposition treatment and usually not measured. Unless designated as stoichiometric- WO_3 , the term WO_3 should be assumed to mean the variable composition as noted above.

Summary of Literature Survey

Various methods have been used to prepare WO_3 films (e.g., thermal evaporation, rf-sputtering of WO_3 , reactive sputtering of W, electron beam evaporation, flash evaporation, chemical spraying techniques, etc.). It should be noted that detailed preparation conditions are seldom reported.

In case of thermal evaporation of WO_3 powder, various boats (e.g., Ta, W, Pt, Al_2O_3 coated Mo, etc.) have been used. Boat temperatures are kept in the range 1000-1400°C. Films are deposited in the pressure range 10^{-4} Torr⁽⁴⁾ to 10^{-6} Torr⁽⁵⁾, with deposition rates ranging from 10 Å/min⁽¹⁾ to 600 Å/min.⁽⁷⁾ The partial pressure is important since it apparently relates to oxidation of the growing film.

A number of workers have prepared WO_3 films by rf-sputtering^(8, 9, 10) and reactive sputtering^(5, 12, 13). The sputtering condition of total pressure is generally varied from 5×10^{-2} to 10^{-3} Torr of Argon in order to control stoichiometry of WO_{3-y} and H_xWO_{3-y} films over a wide composition range^(5, 12). Sputtering conditions like rf-voltage, power, film self-bias voltage and substrate-target distance have not been studied by previous authors. It is well known that these parameters are extremely important in dictating the structural, chemical, and optical properties of films⁽⁶⁾.

It has been reported that sputtered films do not have any water incorporated in them^(5, 13, 14), while evaporated films contain variable amounts of water, which affects the EC performance^(14, 15). This apparent variability in water content has led to nonreproducible evaporated WO_3 films even within one laboratory. The performance of all solid state EC cells is also shown to depend on humidity in the atmosphere⁽¹⁶⁾.

Attempts have been made to distinguish between amorphous and crystalline WO_3 films. Preliminary x-ray diffraction (XRD) studies showed that, depending on deposition conditions, films can be amorphous or crystalline. From SAD and TEM patterns Dauteront-Smith et al.⁽⁹⁾ and Green et al.⁽⁸⁾ showed that crystallite size in sputtered films (0.4-1.0 μm thick) varies between 200-800 \AA , and that these crystallites have tetragonal or orthorhombic structures. The monoclinic structure is completely ruled out by them. On the other hand, from high resolution electron microscope studies Shiojiri et al.⁽¹⁷⁾ found that, in case of evaporated films (100-150 \AA thick), crystallite size varies between 10-20 \AA and crystallites have monoclinic structure. From the results of Green et al.⁽⁸⁾ and Shiojiri et al.⁽¹⁷⁾, it seems that deposition method and film thickness have an effect on crystallite size and its structure⁽⁹⁾.

Most authors found that annealing of amorphous films in air at temperatures between 300-400 $^{\circ}\text{C}$ leads to crystallization^(1, 5, 18) and crystallite size increases in films with fine crystallites^(9, 17).

Usually 0.2 μm to 1 μm thick films are deposited on various substrates (like carbon, glass, platinum, quartz, ITO or Au coated glass) for EC studies. Green et al.⁽¹⁹⁾ observed no effect of the substrate on crystallite size and film growth, but Dauteront-Smith et al.⁽⁹⁾ and Zeller⁽¹⁸⁾ have noticed the effect of the substrate on crystallite size (in sputtered films). Substrate temperature is generally varied between R.T.-300 $^{\circ}\text{C}$ with higher substrate temperatures giving crystalline films rather than amorphous films⁽¹⁹⁾. Also, a higher sputtering rate causes substrate heating and leads to microcrystalline films⁽²⁰⁾. Similarly higher substrate temperatures $\geq 270^{\circ}\text{C}$ produce blue films, i.e., more nonstoichiometry⁽⁵⁾.

Green et al.⁽¹⁹⁾ observed that films with crystallite size $\geq 250\text{\AA}$ have tetragonal II structure and Hurditch⁽¹⁴⁾ has observed a monoclinic structure in annealed films with comparable crystallite size. This suggests that depending on the substrate and substrate temperature, the deposition method and post-deposition treatment of films stabilizes a different type of structure and different crystallite size.

The chemical composition of WO_3 films has been determined by a nuclear resonance reaction technique and proton backscattering technique⁽⁵⁾. Also, Auger electron spectra (AES)^(21, 4) has been used. EPR^(22, 23) and ESCA^(4, 24) have been used to detect W^{+4} , W^{+5} ions in WO_3 films. Stoichiometry of WO_3 films is shown to range from WO_2 up to WO_3 ^(4,5). Many authors have annealed their films in air, O_2 and N_2 or in vacuum. Only Schrimmer et al.⁽¹⁸⁾ have shown that the chemical composition (stoichiometry) changes in films annealed in air and O_2 . Their qualitative results are based on x-ray fluorescence analysis. Therefore, the effect of annealing on composition has to be determined quantitatively.

Along with the compositional analysis, optical properties of WO_3 films have been studied to understand the mechanism of electrochromism. The optical absorption band in colored films peaks between 0.90eV and 1.46eV depending on film properties^(1, 18). Additives like MoO_3 (10%) shifts the bandpeak in colored films to higher energies⁽²¹⁾, whereas additives like BaO ⁽²⁵⁾, show no shift in bandpeak but suppress the EC efficiency.

Originally Deb⁽¹⁾ proposed that coloration in WO_3 films is due to F type color centers, which is no longer valid. Faughnan et al.⁽²⁶⁾ suggested the formation of a hydrogen tungsten bronze ($\text{H}_x\text{WO}_{3-y}$) by a double injection of protons and electrons. This was interpreted in terms of intervalence transfer

between W^{+5} and W^{+6} . Schriener et al.⁽¹⁸⁾ and Deneuille et al.⁽⁵⁾ have proposed the small polaron model for coloration. From electron spin resonance studies at low temperatures, Pifer et al.⁽¹¹⁾ have given evidence which argues against the small polaron model. Therefore, it seems that the exact electrochromic mechanism in WO_3 films yet to be confirmed.

In recent years various solid state sandwich cell structures for EC devices have been proposed^(8, 9, 4, 16, 27-30). Barna⁽⁴⁾ has shown that interfacial resistance between layers varies when WO_3 films are deposited by different methods onto an ITO layer. At present little is known about the exact nature of the electrochromism, life-time, and ultimate limits on switching speeds in such devices⁽³⁾. Due to these reasons most of the authors have used liquid electrolytes (aq. H_2SO_4 and Li^+ , Na^+ , K^+ , Ag^+ in organic solvents) to study the electrochromism in WO_3 films. The main drawback of aqueous electrolytes is the strong dissolution of WO_3 film in water, affecting EC performance and life of the device. Therefore, studies have been made on dissolution kinetics of WO_3 films in various solvents^(15, 31).

Power requirements and switching speeds of EC devices have been considered in detail by Faughnan⁽³⁾. The power required to induce a given contrast ratio varies from $3mC/cm^2$ to $16mC/cm^2$. With the contrast ratio depending on the preparation method and conditions of WO_3 films. Sputtered films have been reported to have poorer EC efficiency than evaporated films^(3, 13) although Kobale⁽³²⁾ and Green et al.^(8, 9, 19) have shown that sputtered films can have good EC sensitivity. Diversity of such results should not be taken as contradiction but rather as an indication of extreme sensitivity of WO_3 films on preparation conditions.

From the above discussion we realize that basic electrochromic phenomena in WO_3 films have turned out to be exceedingly complex. Their proper understanding requires a knowledge of solid state physics, amorphous materials, chemistry and electrochemistry. Thus, at present an important problem is to elucidate the critical material parameters controlling the electrochromic behaviour in WO_3 films.

Aim of the Present Work

As seen in the previous section, a number of parameters control the EC sensitivity in WO_3 films. Information from the literature is not adequate enough to correlate material preparation parameters uniquely to EC sensitivity and thus enabling one to make optimum EC devices.

Our approach to understanding problems and phenomena in this area can be divided into four stages as follows.

- 1) Establish a method to prepare WO_3 films in a reproducible manner, with good control over physical, chemical and electrical properties.
- 2) Using such a method, vary the preparation parameters in order to optimize EC sensitivity in WO_3 films.
- 3) Characterize the structure (micro and nano) and chemical composition of these films in their virgin, colored and bleached states. See the effect of annealing on composition.
- 4) Measure optical and electrical properties of films (virgin, colored and bleached) prepared at various conditions.

From this study we should be able to develop a model, which correlates preparation parameters to structure, composition and electrical properties of WO_3 films. From such a model we shall then be able to specify conditions for

optimum electrochromic WO_3 films and the limits to which electrochromic performance (eg., good contrast ratio, long life, long memory, no chemical degradation) can be improved.

Results and Discussion

A. Anodization

As explored in previous studies⁽³³⁾ the method of electroanodization was investigated to prepare amorphous WO_3 films. In the anodization of W metal, we systematically changed the parameters of (a) pH of electrolytes (aq. solutions of H_2SO_4 , HNO_3 , H_3PO_4), (b) temperature of electrolytic bath (0°C to 80°C), (c) current density, and (d) potential applied to W electrode. Also various surface treatments (mechanical and electrochemical polishing) were given to the W metal sheets and foils. In general, these parameters showed an effect on the kinetics of oxide film formation, but no appreciable change in EC properties was detected, as reported previously⁽³⁵⁾. The oxide film thickness (maximum) obtained was less than 1000\AA .

X-ray diffraction patterns showed very broad peaks suggesting an amorphous structure. This peak broadening may be due to thickness of film also. Comparing these results with XRD patterns of various phases of WO_3 , WO_{3-y} and $\text{H}_x\text{WO}_{3-y}$, no conclusions could be drawn about the structure of anodic WO_3 films. SEM and TEM studies could not be made due to experimental difficulties. In the future, we are planning to do compositional analysis and depth profiling using AES and SIMS. Details of anodization experiments and problems in structural characterization will be discussed elsewhere.

B. rf-Sputtering

Reactively sputtered films give good control over reproducibility and a wide range of stoichiometry^(5, 12). Therefore, we prepared the WO_3 films

by reactive sputtering of a tungsten target (2 inch diameter), in an atmosphere of argon, oxygen and hydrogen. In all sputtering experiments no external heating or cooling was applied to the substrates (glass, ITO coated glass, W foil, Au and ITO glass) although heating due to bombardment processes in sputtering occurs and has been measured to be $\sim 100-200^{\circ}\text{C}$ for conditions similar to those presently reported.

In the literature we find that ITO substrates with resistivities ranging from $5\Omega/\square$ ⁽²⁹⁾ to $500\Omega/\square$ ⁽³⁴⁾ have been used. In order to see the effect of conductivity of ITO layer on EC behaviour, we used ITO substrates with various resistivities ($100, 50, 25\Omega/\square$). One micron ($1\mu\text{m}$) thick films of WO_3 were deposited at 20mTorr total pressure ($P_{\text{Ar}} = 19\text{mTorr}$ and $P_{\text{O}_2} = 1\text{mTorr}$) and power density 5 watts/cm^2 at 800 volts. Films on ITO substrates ($25\Omega/\square$) showed maximum coloration in EC test and, therefore, were used in all subsequent tests.

Gold films of various thicknesses ($50, 100, 200\text{\AA}$) were deposited onto the ITO layer by dc-sputtering with $1\mu\text{m}$ thick WO_3 films deposited, in turn, onto the Au/ITO layer. In the EC test, the Au layer showed blistering at voltage ≤ 1 volt, causing WO_3 films to peel off from the substrate. Deposition of WO_3 films on W foil at various sputtering conditions, gave blue rather than transparent films.

Sputtering parameters like rf-power density, rf-voltage, substrate-to-target distance and partial pressure of Ar, O_2 , H_2 were systematically changed in the following set of experiments.

Set 1 (a) Argon and oxygen pressures were varied from 0-30mTorr in such a way that different ratios of Ar/O_2 were obtained at various total pressures ($P_{\text{tot}} = 5, 10, 15, 20, 25, 30\text{mTorr}$). Power density 4.9 watts/cm^2 at 800 volts and 35mm distance between substrate and target was kept constant. All films were tested for EC efficiency. The best EC effect (maximum coloration) was shown by

the films, which are deposited at 20mTorr pressure ($P_{Ar} = 19\text{mTorr}$ and $P_{O_2} = 1\text{mTorr}$). Films deposited at pressures $>20\text{mTorr}$ were crystalline by XRD.

(b) By keeping 20mTorr total pressure ($P_{Ar} = 19\text{mTorr}$ and $P_{O_2} = 1\text{mTorr}$), rf voltage was varied from 50-1000 volts. As a result power density varied from 1.2-14.8 watts/cm². Films deposited at higher power densities (>4.9 watts/cm²) and voltages >800 volts were crystalline and opaque white or yellowish.

Set 2 (a) In order to more precisely control the oxidation state of WO₃ films, the partial pressures of O₂ and H₂ were varied from $1 \times 10^{-6}\text{Torr}$ to 10mTorr. Total pressure was kept at 20mTorr by adjusting Ar pressure from 0-19mTorr. In one experiment total pressure was 20mTorr obtained with 10mTorr O₂ and 10mTorr H₂. Power density 4.9 watts/cm² at 800 volts and 35mm substrate-to-target distance are kept constant. Depending on the ratio of O₂:H₂:Ar, we obtained films which were metallic, dark blue, light blue and transparent. Due to complexity of parameters and results in these experiments, they will be discussed in detail elsewhere. In essence, our observations are similar to the results reported by Deneuville et al.⁽⁵⁾.

All films were tested for EC efficiency. Films deposited at 20mTorr total pressure ($P_{Ar} = 19\text{mTorr}$, $P_{O_2} = 1\text{mTorr}$, $P_{H_2} = 5 \times 10^{-6}\text{Torr}$) showed best EC sensitivity among all other samples. Also blue coloration remained for months, showing good memory.

(b) In order to investigate total pressure in the range 5-30mTorr, argon pressure was changed in steps (e.g., 4, 9, 14, 24, 29mTorr) while $P_{O_2} = 1\text{mTorr}$ and $P_{H_2} = 5 \times 10^{-6}\text{Torr}$ were kept constant. Power density 4.9 watts/cm² at 800 volts and 35mm substrate-target distance are kept constant. Again, good EC sensitivity was shown by films deposited at 20mTorr pressure ($P_{Ar} = 19\text{mTorr}$,

$P_{O_2} = 1\text{mTorr}$ and $P_{H_2} = 5 \times 10^{-6}\text{Torr}$).

(c) Films were deposited at various power densities (1.2-14.8 watts/cm²) and different voltages with total pressure kept at 20mTorr ($P_{Ar} = 19\text{mTorr}$, $P_{O_2} = 1\text{mTorr}$, $P_{H_2} = 5 \times 10^{-6}\text{Torr}$). Films deposited at power density 4.9 watts/cm² (at 800 volts) showed the best EC sensitivity and memory.

From the above sets of experiments, we found the appropriate sputtering conditions to prepare optimum (for our range of tests) EC WO₃ films in a reproducible manner, i.e., $P_{Ar} = 19\text{mTorr}$, $P_{O_2} = 1\text{mTorr}$, $P_{H_2} = 5 \times 10^{-6}\text{Torr}$ and power density = 4.9 watts/cm² at 800 volts, substrate-target distance = 35mm).

Using thermosensitive indicates the temperature of ITO substrates, during various sputtering conditions, were measured. Maximum temperature of 130°C was reached in 15 minutes at the optimum conditions described above.

Under our optimum sputtering conditions substrate to target distance was changed from 30mm to 70mm: however, no appreciable change in EC sensitivity was detected.

Films deposited under the optimum sputtering conditions were analyzed with SIMS for W/O ratio and H content. For a transparent virgin film of WO₃, the depth profile revealed that W/O ratio and H concentration is constant down up to the substrate, indicating that the films are homogeneous. In the case of colored films, H concentration was, higher as compared to virgin films with depth profile showing that this H concentration remains constant down to substrate. Faughnan et al.⁽³⁾ mentioned that sputtered films only color in thin layer (<1000Å). Our SIMS results on virgin and colored films do not agree with their findings. It is difficult to enumerate the reasons for this disagreement, because we do not know the details of their chemical characterization.

Films prepared at various sputtering conditions were annealed in the temperature range 100-400°C, in air, and N₂ atmosphere. Annealed films can be colored electrolytically, but coloration decayed at room temperature. The higher the annealing temperature, the faster was the decay of coloration. Long annealing times up to 24 hours, reduced the coloration memory up to 5 minutes or less. Films annealed in oxygen atmosphere, became yellowish with the EC test inducing inhomogeneous coloration with poor memory.

Throughout the above described series of films, preparations were carried out at each set of conditions for two different times such that films of ~1µm and ~12-15µm were obtained for each preparation conditions. Above we have described the qualitative EC behavior of the 1µm thick set of film using a liquid-electrolyte cell configuration [ITO⁻/WO₃/H⁺(HNO₃, 1N)/Pt⁺]. The set of thicker films (12-15µm) were prepared for the purpose of characterizing the physical microstructure of these films and its relation to EC behavior. Such a correlation is important since there has been no serious attempt to date to show, if any, a microstructure - property relation for EC WO₃ films. Thicker films were chosen since the microstructure, though generally columnar⁽³⁶⁾, is evolutionary⁽³⁷⁾ and thereby excentuated as film thickness is increased.

SEM micrographs of the top surface and fractured edges of a series of films in which P_{Ar} was varied (see Figure 1) showed that a distinctly columnar microstructure is evident at high P_{Ar} (Figure 1a), decreases with decreasing P_{Ar} (Figure 1b), and is barely visible at P_{Ar} = 5mTorr. It is suspected that this minimization of microstructure is due to positive ion bombardment (eg, Ar⁺) of the growing film which results from high negative floating potentials on the film. However, electrostatic probe measurements of the plasma are needed. We have previously shown that such a mechanism is the primary cause of

microstructure reduction in a-Si:H sputtered films⁽³⁸⁾. It is interesting to note that EC behavior does not occur in films which have negligible columnar structure. Although more tests are again required, we can at least suggest at this point that a direct link between anisotropic physical structure and hydrogen ion transport (EC behavior) exists in which fast ionic diffusion occurs down the intercolumnar void regions with slower ionic conduction into the columns. Other evidence which support this suggestion are: annealing leading to loss of EC coloration and memory; SIMS profiles showing higher concentration of hydrogen in the colored films as compared to virgin, transparent films; and the essentially constant level of hydrogen throughout the thickness of a 1 μ m thick electrolytically colored films. Again, the a-Si:H literature provides further support in that post-deposition re- and de-hydrogenation of a-Si films has been related to the columnar void structures in those amorphous films. This microstructure-property relation for EC WO_3 thin films has been suggested by Green⁽¹⁹⁾; however, he relates the microstructure to crystalline grain boundaries which are distinctly different than the void network structures⁽³⁶⁻³⁸⁾.

Conclusions and Plans for Future Work

Our results prove that WO_3 films with good EC sensitivity (switching speed <1 second) can be made by reactive sputtering. Depending on preparation conditions various contrast ratios are obtained in colored films. Annealing shows an effect on memory of coloration which has not been reported previously. Finally, a mechanism for fast ion transport in amorphous WO_3 thin films based on their anisotropic microstructure was suggested.

Further experiments which are suggested from these preliminary though important studies are:

1) Structural characterization of films prepared under optimum sputtering conditions in order to see the detailed effects of thickness on the physical structure of WO_3 . (TEM and SEM study).

2) Quantitative results should be obtained for compositions of films (virgin, colored, bleached and annealed) by using standards in SIMS and AES analysis.

3) Along with the structural and chemical characterization, optical properties should be analyzed quantitatively. This will help us to understand the EC mechanism and its relation to microstructure.

4) Dissolution kinetics should be studied for various films. Also related electrical properties should be measured.

References

1. S. K. Deb, *Philos. Mag.* 27, 801 (1973).
2. C. J. Schoot, J. J. Ponjee, H. T. VanDam, R. A. Van Doorn, and P. T. Bolwijn, *Appl. Phys. Lett.* 23(2), 64 (1973).
3. B. W. Faughnan and R. S. Crandall, *Topics in Appl. Phys.* 40, 181 (1980).
4. G. C. Barna, *J. Electron Mat.* 8, 153 (1979).
5. A. Deneuveille and P. Gerad, *J. Electron. Mat.* 7, 559 (1978).
6. R. Messier, T. Takamori, and R. Roy, *J. Vac. Sci. Technol.* 13(5), 1060 (1976).
7. M. Manfredi and G. C. Salviati, *Thin Solid Films* 75, 133 (1981).
8. M. Green, W. C. Smith, and J. A. Weiner, *Thin Solid Films* 38, 89 (1976).
9. W. C. Dautremont-Smith, M. Green, and K. S. Kang, *Electrochim. Acta.* 22, 751 (1977).
10. R. S. Crandall and B. W. Faughnan, *Appl. Phys. Lett.* 26(3), 123 (1975).
11. J. H. Pifer and E. K. Sichel, *J. Electron. Mat.* 9(1), 129 (1980).
12. P. Cerad, A. Deneuveille, G. Hollinger, and T. M. Duc, *J. Appl. Phys.* 48, 4252 (1977).
13. H. R. Zeller and H. U. Beyeler, *Appl. Phys.* 13, 231 (1977).
14. R. Hurditch, *Electron. Lett.* 11(7), 142 (1975).
15. J. P. Randin, *J. Electron. Mat.* 7, 47 (1978).
16. H. J. Stocker, S. Singh, L. G. VanUitert, and G. J. Zydzik, *J. Appl. Phys.* 50(4), 2993 (1979).
17. M. Shiojiri, T. Miyano, and C. Kaito, *Jpn. J. Appl. Phys.* 17, 567 (1978).
18. O. F. Schriener, V. Wittwer, G. Baur, and G. Brandt, *J. Electrochem. Soc.* 124, 749 (1977).
19. M. Green, *Thin Solid Films* 50, 145 (1978).

20. E. K. Sichel, J. I. Gittleman, and J. Zelez, Appl. Phys. Lett. 31, 109 (1977).
21. B. W. Faughman and R. S. Crandall, Appl. Phys. Lett. 31, 834 (1977).
22. S. K. Deb, Phys. Rev. (b), 16(3), 1020 (1977).
23. P. Gerad, A. Deneuville, and R. Courths, Thin Solid Films. 71, 221 (1980).
24. R. J. Colton and A. M. Guzman, J. Appl. Phys. 49(1), 409 (1978).
25. B. J. Malonar, A. R. Haranhalhi, and D. B. Dove, J. Vac. Sci. Technol. 15(2) 261 (1978).
26. B. W. Faughnan, R. S. Crandall, and P. M. Heyman, RCA Rev. 36, 177 (1975).
27. A. Deneuville, P. Gerad, and R. Billet, Thin Solid Films 70, 203 (1980).
28. Y. Hajimota and T. Hara, Appl. Phys. Lett. 28(4), 228 (1976).
29. A. T. Howe, S. H. Sheffield, P. E. Childs, and M. G. Shilton, Thin Solid Films 67, 365 (1980).
30. S. K. Mohapatra, G. D. Boyd, F. G. Storg, S. Wagner and F. Wudl, J. Electrochem. Soc. 126(5), 805 (1979).
31. T. C. Arnoldussen, J. Electrochem. Soc. 138(1), 117 (1981).
32. M. Kobale and H. P. Lorenz, (mentioned in reference 13).
33. A. DiPaola, F. DiQuarto and C. Sunseri, J. Electrochem. Soc. 125(8), 1344 (1978).
34. M. Green and D. Richman, Thin Solid Films 24, 545 (1974).
35. A. Bholagir and R. Messier, (unpublished).
36. J. A. Thornton, Ann. Rev. Mat. Sci. 7, 239 (1977).
37. R. Messier, S. V. Krishnaswamy, and R. Ross (unpublished)
38. R. Ross and R. Messier, AIP Conf. Proc. (in press).

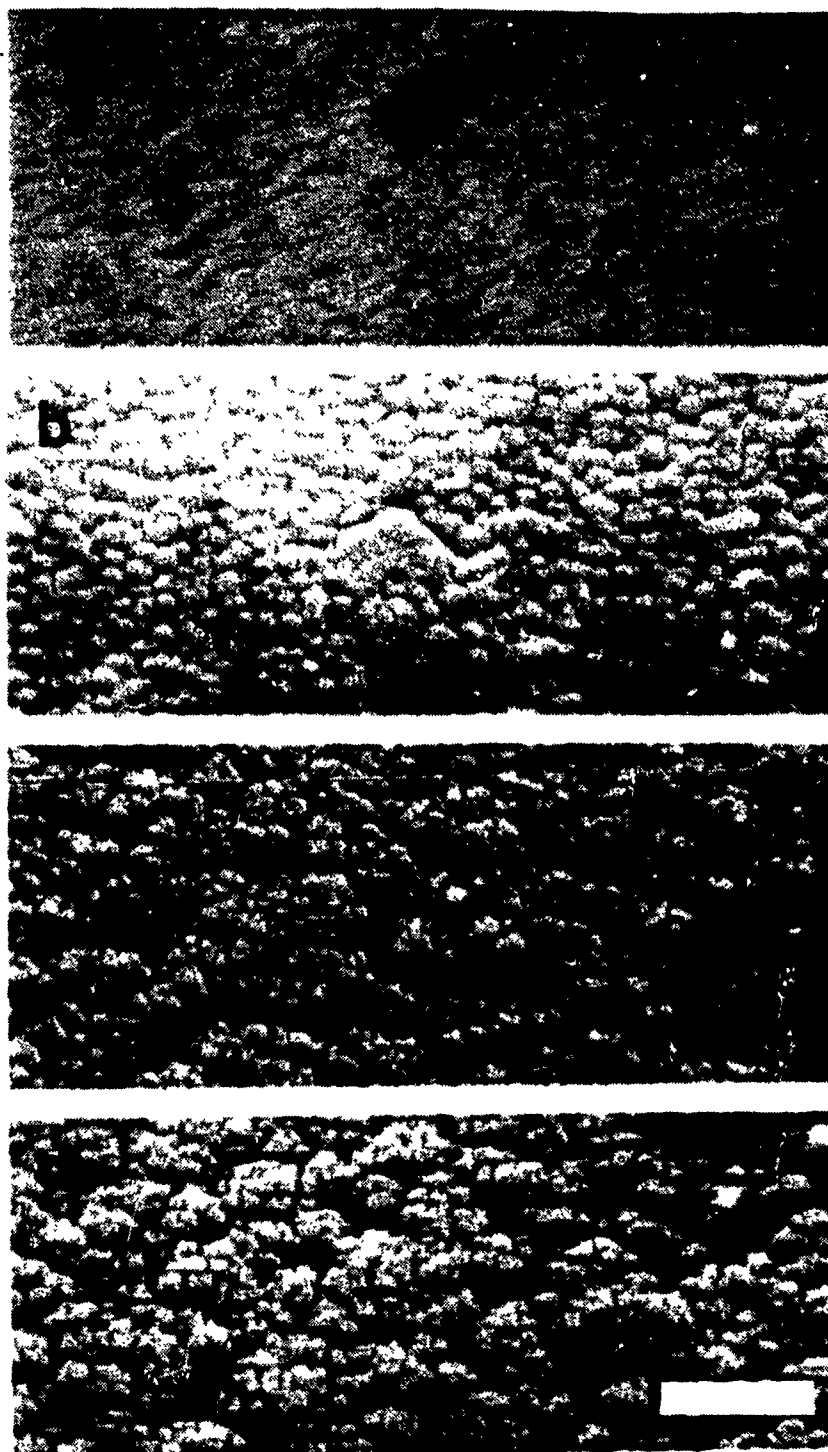


Fig. 1 SEM microstructures of a series of films in which the O_2 (1mTorr) and H_2 (.005 mTorr) partial pressures during sputtering were constant and the Ar partial pressure varied: a) 4mTorr, b) 9mTorr, c) 19mTorr, and d) 29mTorr. The film thickness was $15\mu m$ in all cases. The marker equals $1\mu m$.

APPENDIX I

Voids in Thin Films: A TEM and FIM Comparison

INTRODUCTION

The correlation of thin film properties with those of corresponding bulk materials has always been tenuous. Of the studies that have attempted to relate these differences in properties to materials characterization, most have concentrated on impurity incorporation and the role of crystalline grain boundaries. The role of voids, which are generally regions of lower density in thin films^(), however, has only recently been considered. Most thin film void studies have been on amorphous semiconductors with some work on crystalline metallic films and essentially no work on insulating films reported. Unfortunately, most thin film studies have not considered the effect of void, or low density, network structures on resulting film properties. In most instances, thin films are erroneously considered to be homogeneous and isotropic, especially for noncrystalline films.

Voids have been invoked in the past to rationalize the apparent discrepancies that exist in density data of amorphous semiconductors^(2,4,8-10), to understand the perpendicular anisotropy in magnetic alloys,^(5,7,11) to relate to anisotropic diffusion⁽⁶⁾, etching⁽¹²⁻¹⁴⁾, post-deposition oxidation behavior^(10,15-17) etc. Although much remains to be understood about voids, a number of general observations can be made. Under deposition conditions of low adatom surface mobility voids are usually correlated low density regions with a correlation direction close to that of the average angle of the impinging vapor species⁽¹⁸⁻²¹⁾. For instance, isolated, essentially isotropic, voids occur primarily in metal films with high surface mobilities during deposition⁽²²⁻²⁴⁾. Such anisotropic voids

are neither very much dependent on the crystal structure or degree of crystallinity nor on the method of preparation. Therefore, voids are highly dependent on the preparation history such as heating and film bombardment effects.

Finally, anisotropic voids generally form honeycomb-like networks which surround columns $\sim 100\text{\AA}$ in diameter for most materials. Such a column seems to be the basic void network unit, yet little is known about their origin or even why their characteristic size is always around 100\AA for a wide diversity of materials. As the film increases in thickness the void networks become more complex due to the incomplete coalescence of the $\sim 100\text{\AA}$ size columns which leads to yet larger voids, in addition to these smaller honeycomb-like voids and associated larger columns, typically $1000\text{--}3000\text{\AA}$.

Recently, we have used the atomic resolution and single atom detection capability of the atom probe field ion microscope (APFIM) to image sputtered thin films in both the nucleation and growth stages plus to chemically analyze the vapor species field evaporated during the depth profiling process^(16,17,25). Our experiments indicate clustering in a-Ge films and polycrystalline Au, Ni and Pt films. In a detailed study of voids in a-Ge and a-Ge:H films we have shown that the void networks are really low density regions which surround $\sim 100\text{\AA}$ – 300\AA diameter nano columns, are aligned in the direction of impinging vapors and originate at the interface. The interface is not distinct but graded over $\sim 10\text{--}30\text{\AA}$, indicating some type of mixing (probably bombardment-induced). In this paper, we have compared both TEM and FIM techniques for the observation of voids in a wide range of sputtered thin films. Both the techniques provide similar results in a complementary rather than redundant manner.

EXPERIMENTAL

Films were deposited onto Mo field ion tips as well as carbon coated

copper grids (400 mesh) using our MRC (Model 8520) rf-diode sputtering system described elsewhere⁽¹⁴⁾. The diffusion pumped system was routinely pumped to 2×10^{-5} Pa before backfilling with Ar sputtering gas. The sputtering parameters were 20mTorr Ar, 50W rf-power, 500-800V for target voltage depending upon material, and 50 to 55 mm for target-to-substrate distance. The deposition time was controlled to obtain an estimated film thickness in the range 1000-3000Å on FIM tips and 1200-1800Å on TEM grids. The FIM and TEM samples were not prepared simultaneously but sequentially under the same operating conditions.

After deposition the tips were transferred to the APFIM and the grids to the electron microscope. Details of the atom probe used in this investigation are given elsewhere⁽²⁶⁾. The films were imaged in the APFIM using 5×10^{-4} to 6×10^{-3} Pa H_2 or Ne, a pressure range typical for a FIM with a channel plate image intensifier. The tip specimens were maintained at 95K during imaging and pulse evaporation.

The coated grids were examined using Philips EM 300 and JOEL 100C transmission microscopes, operated at 100 kV. For imaging the void networks, the defocus phase contrast technique⁽²⁷⁾ was used. In the case of the tungsten oxide films difficulties were experienced because of electrical charging of the films in the electron beam, resulting in their disruption. The problem was overcome by bonding the carbon substrates to the copper grids with an adhesive and evaporating a thin ($\sim 100\text{\AA}$) carbon coating on top of the sputtered WO_3 films.

RESULTS

Fig. 1 shows field ion micrographs of polycrystalline films of Ni and Au deposited on Mo tips. The Ni film is imaged (Fig. 1a) in $\sim 10^{-3}$ Pa H_2

at 12 kV. As can be seen from the figure there is a network of voids, or low density regions, interconnecting the polycrystalline grains. The grains are $\sim 100\text{--}300\text{\AA}$ while the voids are estimated to be $\sim 20\text{--}150\text{\AA}$ in width. Similar size voids were imaged for Pt films on Mo tips. The grain size as well as the void size in the Au film (Fig. 1b) is larger with the dominant large grains ~ 500 to 800\AA with $\sim 100\text{--}400\text{\AA}$ size voids separating the grains. Further, the dark regions indicate a network structure for Au.

TEM results for these metal films show a general trend of increasing grain size and void size with increasing film thickness. However, there is a large variation in void density between Pt, Ni, Au, and Cu films, as well as a considerable range of grain sizes in films of comparable thickness (see Fig. 2). It is seen that the void sizes range from $\sim 10\text{\AA}$ (for Pt) to 150\AA (for Au). Note that the Cu film, with the largest grain size, is the most dense of the films and the voids are widely separated. The Pt and Ni have the best developed void network structures. In the copper and the gold no such structures exist, but isolated voids occur within grains and at grain boundaries.

Voids in a-Ge range in size from 100 to 300\AA depending upon the preparation conditions as reported earlier in our FIM study⁽¹⁶⁾. An example of such a void in a-Ge film is shown in Fig. 3a in which the low density void regions are exposed by raising the dc voltage so as to operate in an essentially over-focus condition. Fig. 3b is a transmission electron micrograph of a similar film showing voids up to $\sim 20\text{--}50\text{\AA}$ in size forming an interconnected honeycomb network structure.

Fig. 4a is a transmission electron micrograph of an a-Si film, which shows that these films have much less structure than the a-Ge films. At exact focus the a-Si films appear structureless even at magnifications of 200,000

times, in contrast to the void networks in a-Ge. Use of the optimum defocus method, utilized first by Nakahara and his colleagues⁽²⁷⁾, shows that any voids present in the a-Si (Fig. 4a) and a-Si:H (Fig. 4b) films studied must be $\leq 30\text{\AA}$ in diameter. Both micrographs were taken at near optimum underfocus and show that the voids, which are less than 30\AA in diameter, are aligned in short strings. This observation, first thought to be an artifact caused by residual objective lens astigmatism, is thought to be significant but is not understood. The strings of voids impart to the image a localized linear structure and such structures in some regions align at approximately 120° .

In Fig. 5a-c, TEM micrographs of approximately equal thickness a-Ge films prepared at three different rf-power levels (25, 50 and 200W) are compared. Again, we see a direct correlation with our earlier FIM studies in that the voids decrease in size with increasing rf-power and, more correctly, increasing film deposition temperature. Fig. 5d shows the TEM micrograph of a film prepared at 50W but with film thickness $2.5\times$ that of the film in Fig. 5b. The most obvious difference is that voids appear larger for the thicker film. However, close inspection shows that smaller voids and associated columns (as seen in Fig. 5b) are still present in the thicker film (Fig. 5d) in addition to the larger voids which tend to dominate the visual appearance of the structure. This sort of superstructure created by the larger voids appears to result from the incomplete coalescence of the smaller $\sim 100\text{\AA}$ size columns, as seen in Fig. 5b.

TEM micrographs of WO_3 films prepared under identical conditions but with different thicknesses are shown in Fig. 6. Again it is clear that as the film thickness increases the total void area increases, and there is an apparent increase in island size as defined by the dominant void network. The islands are roughly equiaxed in the thinnest film but become more irregular with

increased film thickness with many re-entrants. Again, there is evidence of much internal or surface porosity. Void widths vary from $\sim 10\text{\AA}$ (minimum) in the thinnest film (deposition time 2 min.) to $\sim 100\text{\AA}$ (maximum) in the thickest one (deposition time 6 min.). Fig. 6d is an electron micrograph of a WO_3 film prepared in an $\text{Ar} + \text{O}_2$ mixture. The film was prepared at the same rf-power level (50W) and total gas pressure (20mTorr) as the films in Fig. 6a-c. The film thickness is comparable to that in Fig. 6b.

DISCUSSION

We have compared voids in polycrystalline metallic films and noncrystalline Ge, Si, and WO_3 films using TEM and FIM. Both size and nature of voids in these films as investigated by the two techniques appear similar. Also, there is a large variation ($\sim 10\text{\AA}$ to $\sim 300\text{\AA}$) in both the grain and void size in these various films. In metallic-films the interconnected voids decrease, isolated voids increase and crystallite size increases in the order Ni, Pt, Au and Cu. Since the melting points (T_m) of this series of fcc metals also decrease in this order, and if the temperature during film preparation (T) is assumed the same in all cases, then the ratio T/T_m ($^{\circ}\text{K}$) increases. From the structure zone model^(25,28) it has been shown that adatom mobility increases proportionally with T/T_m and that at low ratios anisotropic, interconnected void structures are more favored. Thus, these results are consistent with this model.

Comparing voids in Ge films prepared at different power levels, and hence substrate temperature T_s , we find a correlation between the present (TEM) and our earlier (FIM and SEM) studies^(14,17) in that the void size decreases with increasing T_s . This fits the structure zone model in which the increase in T_s results in the microstructure going from zone 1 to zone T structure and again this can be understood based on the increased surface mobility of the ad atom as

T_g is increased.

Comparing the a-Si films with and without hydrogen we did not observe any noticeable change in the microstructure. But the a-Si films appeared structureless when compared to a-Ge film prepared under similar conditions. A more detailed study investigating the effect of hydrogenation and the evolution of growth as a function of thickness is in progress and will be reported later.

From a comparison of Figures 3(b) and (c) (Ge) and Figures 6(a)-(c) (WO_3) it is clear that the column and void size in these films indeed is thickness dependant, increasing with increasing thickness. In thin films ($<1000\text{\AA}$ thick) voids are clearly interconnected and surround $\sim 100-300\text{\AA}$ columns. As thickness increases the columns seem to evolve into larger columns (~ 1000 to 5000\AA) surrounded by larger, only partially connected voids. The resulting larger void network is not nearly as uniform or as continuous as the smaller void structure. In fact the larger voids sometimes are even isolated. These larger columns appear to contain within them the smaller columns and voids. Similar variations in void size with film thickness has been observed for the polycrystalline metal films. Further, such increase in void size can be brought about with the introduction of O_2 during sputtering (Figure 6d). The effect of O_2 it appears, is to alter and perhaps inhibit the adatom surface mobility of the growing film leading to larger void and columnar growth.

It is perhaps for this reason of different thickness that the voids in a-Ge (Figure 1) as seen by FIM is \sim two times larger than that by TEM. The difference in void size between the two techniques can also be attributed in part to the statistical averaging involved in data sampling in the case of TEM. Further, the difference may also arise due to the difference in the geometry and field effects in the FIM investigation. Moreover, recently we have observed from etching techniques⁽¹⁴⁾ that to an extent, the substrate controls the columnar growth size and resulting void size and this may be another reason why there is

a difference between the two techniques. Finally the voids in FIM appear larger than in TEM due to the fact that it images not only low density but also topographic relief. Thus, grain boundaries separating large grains may appear as voids but may not truly be. This effect of relief is particularly strong when we compare films with large grains as in Au and Cu and it should be emphasized that under these conditions no quantitative information as to grain or void size should be drawn from the FIM data alone. However, it must be noted that FIM still will yield results that can be correlated with that obtained by TEM.

REFERENCES

1. F. L. Galeener, Phys. Rev. Letts. 27, 1716 (1971).
2. G. S. Cargill, Phys. Rev. Letts. 28, 1372 (1972).
3. J. J. Hauser and A. Staudinger, Phys. Rev. B8, 607 (1973).
4. N. J. Shevchick and W. Paul, J. Noncryst. Solids 16, 55 (1974).
5. S. R. Herd, Phys. Stat. Sol.(a) 44, 363 (1977).
6. J. R. Lloyd and S. Nakahara, J. Electrochem. Soc. 125, 2037 (1978).
7. F. P. Esposito, R. S. Newrock and K. Loeffler, Phys. Rev. Letts. 41, 818 (1978).
8. T. M. Donavan and K. Heinemann, Phys. Rev. Letts. 27, 1794 (1971).
9. N. G. Nakhodkin, A. I. Shaldervan, A. F. Bardamid and S. P. Chenakin, Thin Solid Films, 34, 21 (1976).
10. N. G. Nakhodkin, A. F. Bardamid, A. I. Shaldervan and S. P. Chenakin, Thin Solid Films, 65, 209 (1980).
11. S. Esho, J. Appl. Phys. 50, 1006 (1979).
12. L. R. Gilbert, R. Messier and R. Roy, Thin Solid Films 54, 151 (1978).
13. R. Messier, S. V. Krishnaswamy, L. R. Gilbert and P. Swab, J. Appl. Phys. 51, 1611 (1980).
14. P. Swab, S. V. Krishnaswamy and R. Messier, J. Vac. Sci. Technol. 17, 362 (1980).
15. A. Bienenstock, J. Non-Cryst. Solids 8, 49 (1972).
16. S. V. Krishnaswamy, R. Messier, Yee S. Ng, T. T. Tsong and S. B. McLane, J. Non-Cryst. Solids 35/36, 531 (1980).
17. S. V. Krishnaswamy, R. Messier, Yee S. Ng, T. T. Tsong, Appl. Phys. Letts. 35, 870 (1979).
18. D. Henderson, M. H. Brodsky and P. Chaudari, Appl. Phys. Letts. 25 641, (1974).

19. S. Kim, D. J. Henderson and P. Chaudari, *Thin Solid Films* 46, 155 (1977).
20. A. Barna, P. B. Barna and J. F. Pocza, *J. Non-Cryst. Sol.* 8, 381 (1972).
21. A. Barna, P. B. Barna, Z. Bodo, J. F. Pocza, I. Pozgai and G. Radoczi, in:
J. Stuke and W. Brenig (eds.), *Amorphous and Liquid Semiconductors 2*
(Taylor and Francis, London, 1973).
22. N. G. Nahokin and A. I. Shaldervan, *Sov. Phys.-Solid State* 13, 1621 (1972).
23. A. Staudinger and S. Nakahara, *Thin Solid Films* 45, 125 (1977).
24. S. Nakahara, *Thin Solid Films* 45, 421 (1977).
25. S. V. Krishnaswamy, R. Messier, S. B. McLane, Yee S. Ng and T. T. Tsong,
Thin Solid Films 79, 21 (1981).
26. E. W. Müller and S. V. Krishnaswamy, *Rev. Sci. Instrum.* 45, 1053 (1974);
Yee S. Ng and T. T. Tsong, *Surf. Sci.* 78, 419 (1978).
27. S. Nakahara and Y. Okinaka in R. Sard, H. Leidheiser and F. Ogburn (eds.)
properties of Electrodeposits-Their Measurements and Significance,
Electrochemical Society, Princeton, NJ, 1975, Chapter 3.
28. J. A. Thornton, *Ann. Rev. Mater. Sci.* 7, 239 (1977) and references therein.

Figure Captions

- Fig. 1 Field ion micrograph of Ni and Au films rf sputtered onto Mo tips at 50W and 20mTorr: (a) Ni film imaged in 10^{-3} PaH₂ at 12kV (The marker represents 200Å), (b) Au film imaged in 10^{-3} PaH₂ at 15kV (the mark represents 280Å).
- Fig. 2 Transmission electron micrograph of polycrystalline (a) Pt, (b) Ni, (c) Au and (d) Cu films of nearly equal thickness (~1200-1400Å). The marker represents 1000Å.
- Fig. 3 (a) FIM micrograph of a-Ge film on Mo imaged in 5×10^{-4} Pa Ne at 20kV (best image voltage ~18.5kV). The marker represents 500Å. (b) TEM micrograph of a-Ge film on carbon coated copper grid deposited under similiar condition as that in (a). The marker represents 500Å.
- Fig. 4 TEM micrographs of (a) a-Si and (b) a-Si:H film, ~1200Å thick. The marker represents 1000Å.
- Fig. 5 TEM micrographs of a-Ge films prepared at (a) 25W, (b) 50W and (c) 200W. The gas pressure was 20mTorr Ar. (d) Same conditions as in (b) except film thickness is two and a half times larger. The marker represents 1000Å.
- Fig. 6 TEM micrographs of a-WO₃ films deposited for (a) 2 minutes, (b) 4 minutes and (c) 6 minutes under identical conditions (20mTorr Ar, 50W). (d) Film of comparable thickness and as in (b) and deposited under conditions with O₂ added (12mTorr Ar + 8mTorr O₂, 50W). The marker represents 1000Å.

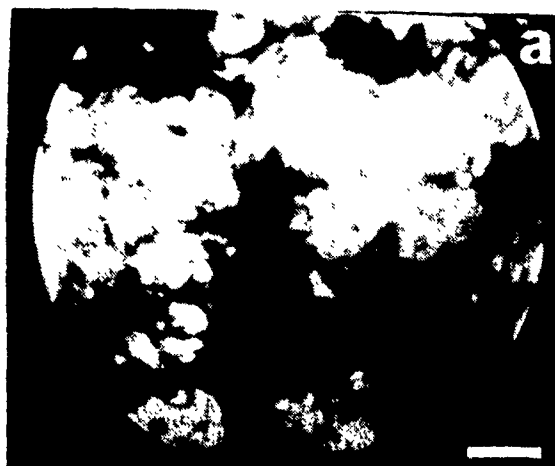


Figure 1

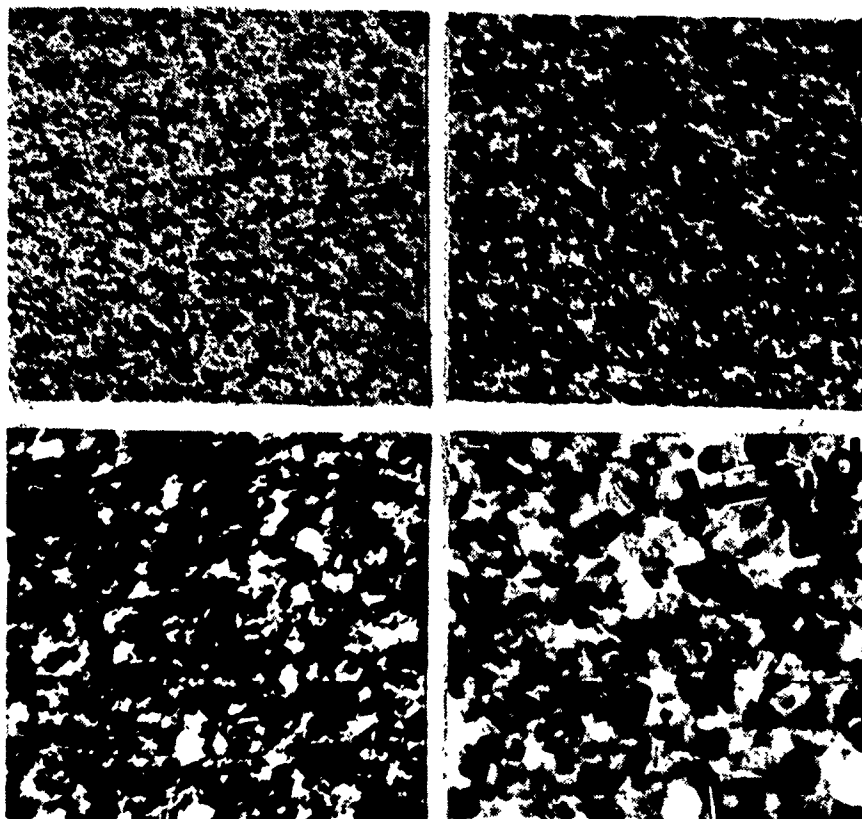


Figure 2

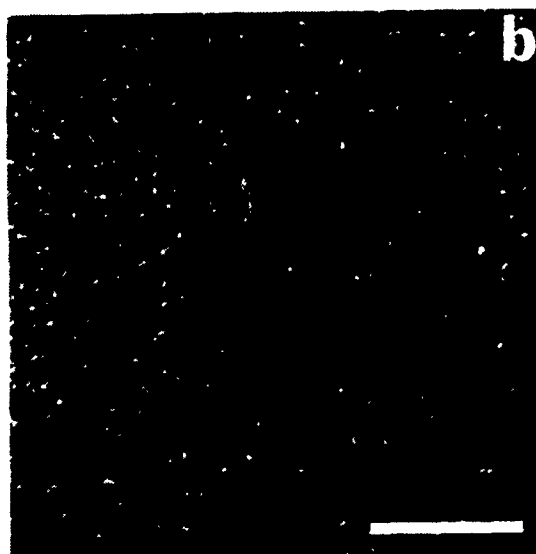
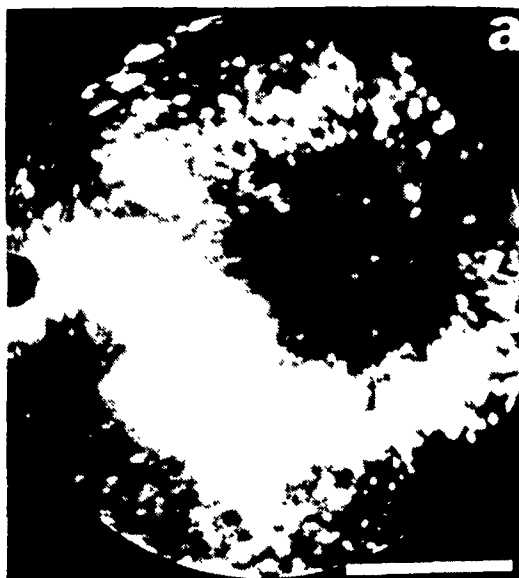


Figure 3

a



b

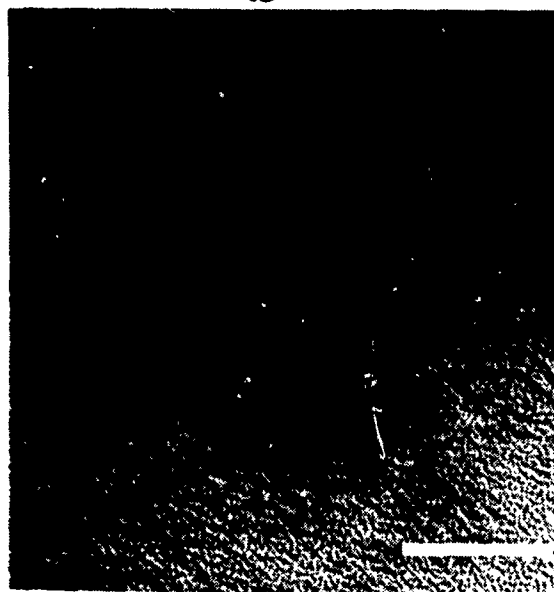


Figure 4

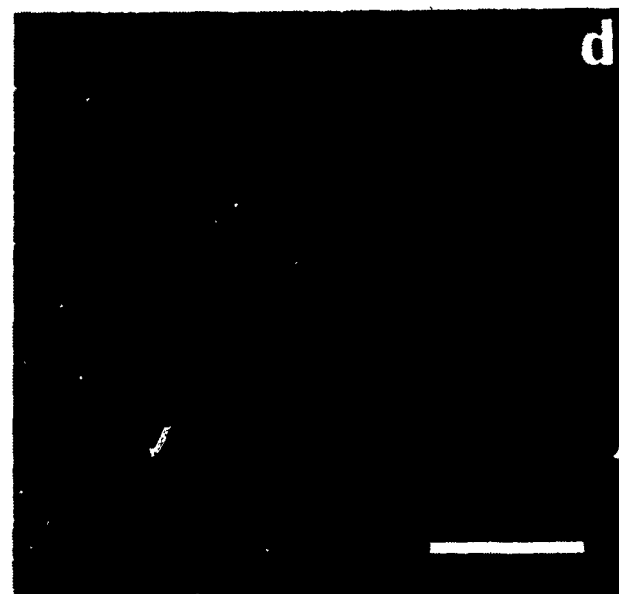
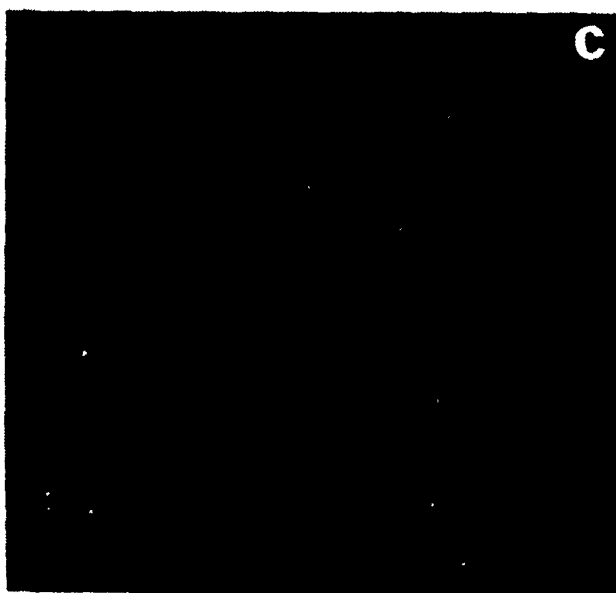
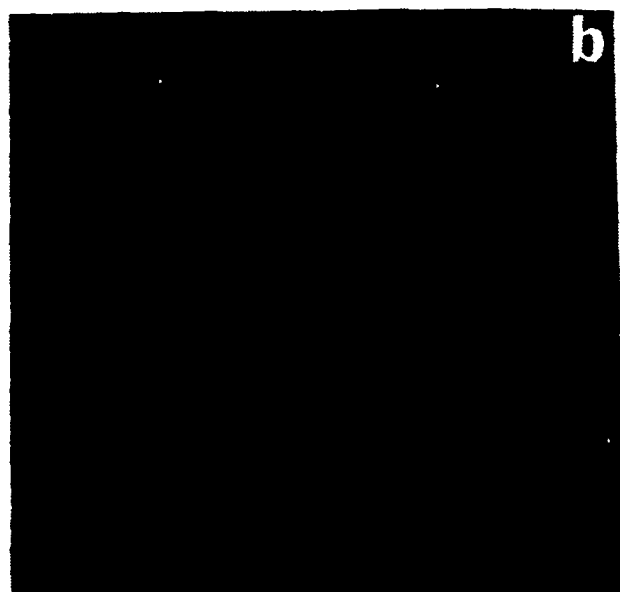
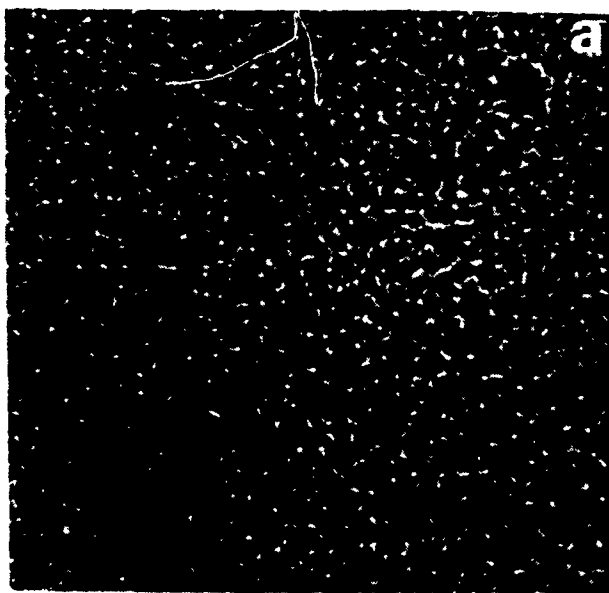


Figure 5

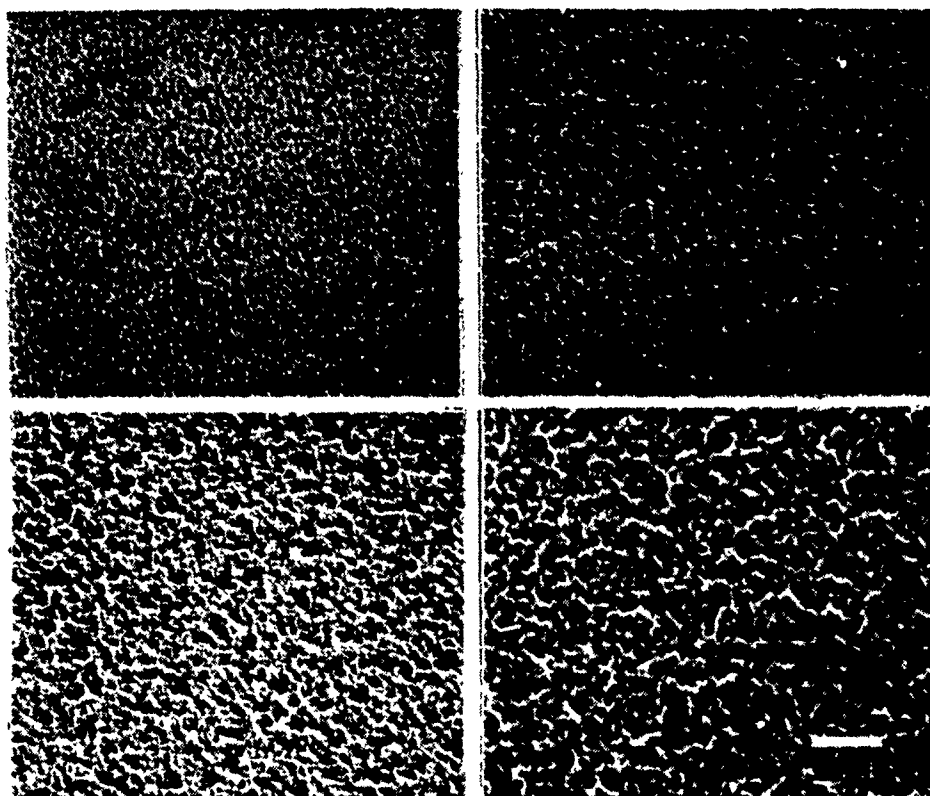


Figure 6